Hierarchical Detection and Assessment of Material Fatigue Damage of the Human Anterior Cruciate Ligament caused by Repetitive Sub-maximal Mechanical Loading

by

Jin Hee Kim

A dissertation submitted in partial fulfillment
of the requirements for the degree of
Doctor of Philosophy
(Chemistry)
in the University of Michigan
2021

Doctoral Committee:

Professor Zhan Chen, Co-Chair
Professor Mark M. Banaszak Holl, Co-Chair, Monash University
Associate Professor Julie Biteen
Professor Jinsang Kim
Professor Edward M. Wojtys

Jin Hee Kim

jinheekm@umich.edu

ORCID iD: 0000-0001-9418-4725

Dedication

For my mom and dad, who ceaselessly loves to learn, and have instilled in me my love of learning and knowledge.

For my sister and brother, who also seek to push the boundaries of knowledge and exercise extreme tenacity in learning.

Acknowledgements

Doing a third rotation was one of the best decisions that I have ever made in grad school. I started to work on the ACL project, hardly familiar with the concern of the sports medicine community regarding non-contact ACL injuries, or the super expensive powerful instrument AFM-IR. Neither did I know that I would be completing my PhD in Australia. Here I am today, with greater appreciation for my work, the techniques and also my mostly stable knees. I couldn't be where I am today, figuratively and literally, without my advisor Dr. Mark Banaszak Holl, who I deeply admire and hope I can be as smart as him one day. I appreciate his guidance as a mentor – as he exercised his patience, and encouragement. I also appreciate his support as a person during this five year journey, where I have had my lows. More than ever, today I resonate with the saying, "The more you know, the more you realize how much you don't know." Mark's contagious fervor in research of all domains, has definitely kindled my love of research – tackling questions with no answers, just yet.

I would also like to thank Dr. Edward Wojtys, Dr. James Ashton-Miller, Dr. Stephen Schlecht, So Young Baek, Dr. Melanie Beaulieu and everyone on the ACL team for their diligence, intellectual contributions, and all other forms of support. Without the team, my thesis would not be the same. I would also like to thank Optiscan for providing me with an opportunity to use their confocal laser endomicroscope for my thesis.

The original Banaszak Holl lab group members at Ann Arbor were amazing colleagues and friends who have also made my PhD journey more personal. JJ who knew everything about anything was a great mentor when I first joined and I appreciate the work he has done for

Chapter 2. Rachel and Isabel helped greatly when I was learning about the AFM-IR and I appreciate our on-going connection. Ted and I have shared a lot of unique experiences as we moved to Australia together. It wouldn't have been as easy without a friend.

Additionally my close friends in CA whom I've known for 10 + years have been a supportive network during my degree. And finally, my boyfriend Simon van Baal, who is also working on his PhD at Monash in philosophy and behavioural economics, have provided enormous support helping me think through my research and also when I didn't have time to cook meals in the midst of preparing my thesis. I couldn't have done it without his insurmountable love and support.

Table of Contents

List of Tables

List of Figures

Abstract

The anterior cruciate ligament (ACL) is a connective tissue adjoining the femur and the tibia, providing stability to the knee joint during articulations. The complex biomaterial's main structural protein is type I collagen, a triple helical molecule, which can self-assemble into macro-hierarchical structures, defining the structure, dynamics, and function of the tissue. It is known that, under repetitive mechanical stress or fatigue, the tissue accumulates microdamage that induces changes in the structure and composition of the tissue in response to the environment. The accumulation of microdamage has been hypothesized to play a role in non-contact ACL injuries, which make up 75% of injuries. Currently, the extent or location of molecular failure, and structural and compositional changes associated with fatigue are unclear. The goal of this research is to elucidate the microdamage signatures in human ACL to better understand the failure mechanism, which can be used to assist programs for injury prevention.

Chapter 1 begins by describing the anatomy and function of the ACL followed by the significant health and economic burdens incurred by the ACL injury. Then the shortcomings of current diagnostic and treatment methods are reported, highlighting the need for higher sensitivity in diagnostic methods and the unresolved problem of re-injury. The material fatigue hypothesis postulates that modulation of magnitude or frequency of loading patterns can alter the fatigue failure life of tissue, thus non-contact ACL injuries can stem from accumulation of fatigue damage due to repetitive sub-maximal loading. The structural and compositional heterogeneity of ACL demands high spatial resolution imaging techniques to capture changes in collagen structure associated with fatigue damage at each hierarchical levels. Therefore,

atomic force microscopy – infrared spectroscopy (AFM-IR) and second harmonic generation imaging (SHIM) are introduced as structural probes.

In chapter 2, the fatigue damage signatures of ACL from a loaded cadaver are characterized at each hierarchical level of collagen organization. At the molecular level, the denaturation of collagen molecules were detected by the spectroscopic peak 1740 cm^{-1} with AFM-IR. This finding was validated by increased binding of collagen hybridizing peptide (CHP) – TAMRA dye in loaded cadavers' ACL. Further structural degradation was seen as a form of fibril voids, and reduction in topographical thickness of collagen fibrils detected by the AFM. Lastly, a reduction in SHG signal intensity and reduction in fiber alignment suggest that the reduction in structural integrity are at least in part responsible for the leading to noncontact ACL failure. Similar damage signatures were found in patients who sustained an ACL injury.

In chapter 3, type I collagen's intrinsic autofluorescence (AF) and second harmonic generation (SHG) signals are used as optical probes to detect accumulation of fatigue damage. A decrease in SHG signal, increase in AF signal intensity with increased anisotropy of collagen fiber orientations in loaded cadavers were found to be consistent with multi-scalar fatigue damage from chapter 2. The feasibility of using a confocal laser endomicroscope (CLE) to detect progression of fatigue damage is explored. Evaluation of damage progression by measuring the changes in AF signal intensity utilizing CLE showed that a larger signal change may indicate larger plastic deformation to the tissue. Additionally, BMI category and posterior lateral tibial slope (PTS) may influence the AF signal due to influence on fiber structure as a result of load distribution on the fibers.

In chapter 4, a detailed spectroscopic analysis of the 1740 cm^{-1} IR peak was carried out to investigate the conformation change in collagen as a result of fatigue. Examination of IR frequencies in the Amide I, Amide III region, and wavenumber associated with tyrosine residue

increased along with the increase in 1740 cm^{-1} peak intensity. The conformation changes describe disruption in the hydrogen bonding network within the helix to increased water mediated hydrogen bonds from the environment, and a disruption in the hydrophobic interactions at the C-telopeptides attributed to tyrosine.

In chapter 5, the results of hierarchical fatigue damage signatures (Ch.2), collagen autofluorescence detection with CLE during progression of fatigue damage (Ch.3) and spectroscopic analysis of 1740 cm^{-1} (Ch.4) are summarized. Future works include three projects expanding on characterization of the fatigue damage signatures: i) AFM-IR detection of local stiffness and composition changes in the ACL as a result of material fatigue ii) O-PTIR (optical photothermal infrared spectroscopy) detection of changes in proteoglycans levels in *in vivo* fatigue tested mouse ACL and iii) Autofluorescence detection by CLE as a sign of fatigue damage progression.

CHAPTER 1

Introduction

Molecular to Macroscale Structure and Chemical Composition of the Human Anterior Cruciate Ligament (ACL)

1.1 Introduction

The human knee is a complex joint and one of the most important load-bearing joints of the body. The anterior cruciate ligament (ACL) is one of the six ligaments adjoining the femur and the tibia providing stability of the knee joint during articulations.[1] Its main function is to protect the knee joint by resisting anterior tibial translation and internal rotation of the tibia from the femur. Unfortunately, ACL is the most commonly injured ligament in the knee and over 350,000 injuries occur in the United States every year which incur financial burdens from treatment cost, rehabilitation therapies, and loss of earnings.[2–4] In addition, the injury appends a debilitating long-term cost of development of osteoarthritis in 50% of injured individuals within 10 – 20 years after injury, inducing pain and functional impairment.[5] 20% of injured patients suffer re-injury within 2 years.[2] Current treatments for ACL injury include neuromuscular training and autograft reconstruction surgery.[6] While these methods strengthen the injured tissue, it is time consuming and cannot guarantee restoration of the ACL back to its equivalent native condition nor exemption from another failure. Therefore, it is necessary to understand the mechanism of the injury to protect the integrity of the tissue prior to these devastating short and long-term costs.

1.2 Material fatigue as a hypothesis for mechanism of non-contact ACL injury

There are two methods of ACL failure: contact mode and noncontact mode. Current dogma regarding ACL injury mechanism has focused on a single overload event caused by excessive abductive movement of the knee[7]; counter intuitively, nearly three-quarters of ACL injuries occur in noncontact mechanism, even in a high collision sport such as National Football League football.[8] Repetition of manoeuvre is critical for athletes for skill acquisition and performance in competition.[9] While collagen-based tissues possess the ability to adapt to required mechanical loads, a faster rate of damage accumulation than biological repair rates can cause overall tissue microdamage, resulting in material fatigue.[10] A structural response to fatigue loading in tendons have known to lead to formation of kinks or repeated distortions, which are a form of discrete plasticity.[11] Additional evidence suggests damage at the molecular level in mechanically overloaded tendons, shown by increased susceptibility to enzymatic cleavage and also increased binding of fluorescent dye tagged collagen hybridizing peptide (CHP) at the sites of denatured collagen.[12] Wojtys and Ashton-Miller et al. showed that the fatigue life (the number of loading cycles tissues can withstand before failure) of a human ACL can depend upon the magnitude of mechanical loading.[9] Therefore, with a high load, the human ACL will fail at lower loading cycles, but even with a low load, the human ACL can still fail with enough loading cycles. The idea of an accumulation of tissue microdamage during normal athletic activity, presents a novel perspective to tackle non-contact ACL injuries as it allows one to consider the loading history of the individual. Further investigation of fatigue damage signatures on the ACL would present an opportunity for strategic intervention for injury prevention.

1.3 Structural and Compositional Heterogeneity of ACL

The ACL is composed of mostly type 1 collagen, proteoglycans, and hydroxyapatite. [13] The difference in their distribution across the matrix serves to minimize stress concentrations at the enthesis. The enthesis is where the ligament attaches to bone, a dynamic part of our body distributing loads applied to them to execute movement.[14] The insertion site possess a complex and heterogeneous structure and composition as a result of the mechanical load it experiences throughout its lifetime. Unfortunately, the ligament to bone insertion site is a site of stress concentration and clinically, most ruptures of the native ACL and graft ACL occur near the femoral enthesis. The enthesis structure can be subdivided into four zones: ligament (L), uncalcified fibrocartilage (UF), calcified fibrocartilage (CF), and bone (B) along with the tidemark which is a border where UF and CF meets[14] (Figure 1.1). The fibrocartilage regions (UF, CF) is a transition region that mediates load transfer between the soft and hard tissue. Qu, D. et al recently demonstrated the compositional heterogeneity of a bovine ACL enthesis at a

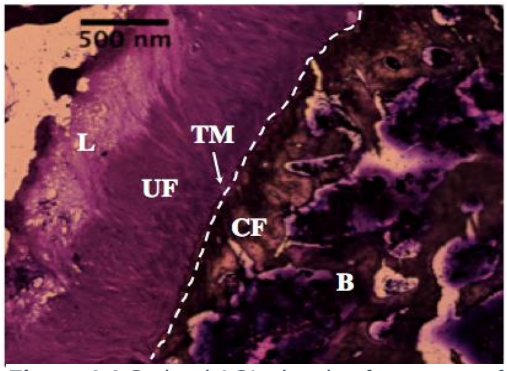

Figure 1.1 *Stained ACL showing four zones of the enthesis (B, bone; CF, calcified fibrocartilage; UF, uncalcified fibrocartilage; L, ligament)*

25 μm spatial resolution showing a steady increase in collagen across the insertion (L→B) and an abrupt increase of the mineral between the uncalcified to the calcified fibrocartilage regions.[13] The regional variation in collagen and mineral content reflects adaptations to mechanical stress generated at the junction in order to minimize stress and aid in load transfer between the soft and hard tissue at the ACL enthesis. Computational studies have shown that

gradient like compositions aid in stress dissipation at the soft tissue to bone interface thus decrease the risk of failure.[11,14] However, animal models of graft-bone healing show that the tissue formed after reconstructive surgery do not develop the four zones characteristic of the enthesis.[5] This insertion presents inferior mechanical properties than the native ACL enthesis.

Heterogeneity of collagenous tissue stems from type 1 collagen, which is composed of three polypeptide alpha – chains with a repetition of Gly-X-Y sequence, with X being proline and Y hydroxyproline being the most common.[15] The glycine residue must occur at every third residue along the chain, as their small size allows the three polypeptide chains to wind into a triple helix structure.[15] Proline and hydroxyproline make up about 22% of collagen, in which the pyrrolidine side chains of proline provide stability of the helices by steric repulsion and the hydroxyl group in hydroxyproline enables the formation of water-mediated hydrogen bonds that stabilize the folded-triple helix.[16] These lead to the ubiquity of the hydrogen bond N – H (gly) ••• O = C(X) within the helix. These molecules, approximately 300 nm in length and 1.5

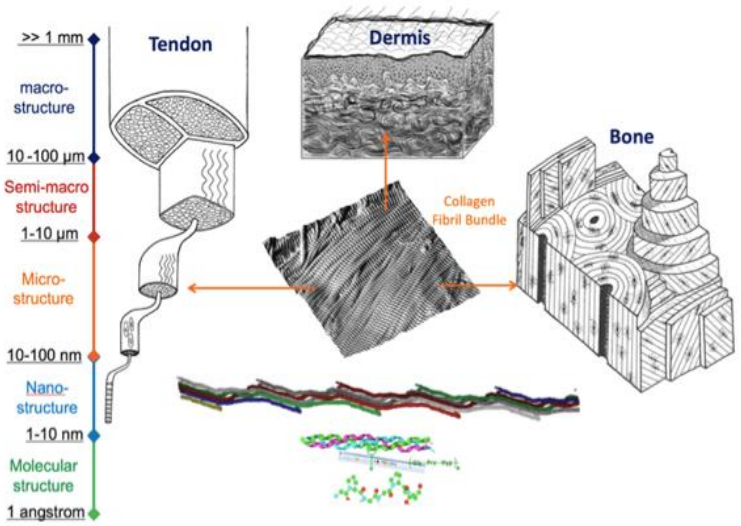

Figure 1.2 *Hierarchical structure of Type 1 collagen in bone, skin and tendon. Chen JJ, Ahn T, Colon-Bernal ID, Kim J, Banaszak Holl MM.ACS Nano. 2017 11(11) 10665-10671*

nm in diameter, then self-assemble into soluble procollagens, followed by collagen fibrils, then into fibers, which then forms macro-hierarchical structures allowing shape and form of tissues to be defined and maintained (Figure 1.2).[10] Thus the ACL owes its mechanical strength to the

heterogeneity of its structure and composition which are present at the molecular level. To understand the extent of how fatigue impacts the ACL, techniques with appropriate spatial resolution must be used.

1.4 Collagen characterization techniques

While electron microscopy (EM) and X-ray diffraction techniques have been used to characterize collagen structure, these techniques possess some downsides. While the diffraction studies have advanced our understanding of the collagen triple-helical structure accepted today – the technique is an ensemble method, which fails to provide information of a single unique fibril.[10] Furthermore, the EM techniques indirectly measures structural information of the fibrils based on electron density through staining rather than a direct measurement from the source.

1.4.1 Atomic Force Microscopy – Infrared Spectroscopy

Atomic force microscopy (AFM) can provide structural information at the nanoscale level through a sharp probe which measures the atomic forces directly between sample and the tip.[12] The technique also requires minimal sample preparation and does not require vacuum, or staining. Paired with the infrared (IR) capability, the AFM-IR allows achieving spatial resolution of an AFM with chemical analysis capability of IR spectroscopy.[13] The AFM – IR can overcome the optical diffraction limit, defined by $\lambda/2$, where λ is the illuminating wavelength. The AFM – IR achieves this goal by a physical detection of a local photothermal expansion of the sample due to a local absorption of IR radiation with the AFM cantilever.[17] Most commercial fourier transform – infrared spectroscopy (FTIR) microscopes have a practical resolution in the range of 2.5 – 7.5 μm whereas AFM - IR can achieve spatial resolution on the ~10 nanometer scale. Although the AFM-IR signal strength depends on material properties of the sample such as sample thermal expansion coefficient, heat capacity,

density and modulus, these properties remain constant at a specific point on the sample, allowing correlation of AFM-IR spectrum to bulk FT-IR.[17] The nanoscale AFM topography map and the local chemical information from hydrated samples can help identify or qualitatively analyze complex heterogenous biomaterials such as the ACL.

1.4.2 Second Harmonic Generation Imaging

An additional technique to complement characterization of nanoscale heterogeneity of the ACL is second harmonic generation imaging (SHIM). SHG is a non-linear optical process, in which constructive interferences of two photons occur due to the non-centrosymmetric organization of collagen at the molecular level.[18,19] Over the past decade, SHG microscopy has emerged as a powerful tool for visualizing the supramolecular assembly of collagen in tissues, enhancing research in disease diagnosis.[20] Due to SHG's emanating from collagen's non-centrosymmetric structure, changes in collagen's micro and macrostructural properties can influence the SHG signal intensity, allowing the technique to act as a structural probe for hierarchical organization of type 1 collagen in ACL.[19,21] Thus unravelling of the collagen molecule would propagate into hierarchical disorder resulting in a loss of second harmonic signal. The fibrillar proteins such as type I and type II collagen meet the structural requirements to generate a SHG signal, while non-fibrillar protein such as base membrane type IV collagen do not, thus lacks SHG signal for imaging. In addition to the high specificity and endogenous contrast mechanism of SHIM, its high sub-micron spatial resolution, reduced photobleaching relative to fluorescence methods, and optical sectioning make it an ideal technique for characterization of the ACL.[18] Together, AFM - IR and SHIM can provide direct measurements of the hierarchical structures of collagen, which can enhance current understandings of fatigue loading impacts on the nano-and-microscale structure of the human ACL.

1.5 References

1. Marieswaran M, Jain I, Garg B, Sharma V, Kalyanasundaram D. A review on biomechanics of anterior cruciate ligament and materials for reconstruction. *Appl Bionics Biomech*. 2018;2018. doi:10.1155/2018/4657824

2. Nessler T, Denney L, Sampley J. ACL Injury Prevention: What Does Research Tell Us? *Curr Rev Musculoskelet Med*. Published online 2017. doi:10.1007/s12178-017-9416-5

3. Bojicic KM, Beaulieu ML, Imaizumi Krieger DY, Ashton-Miller JA, Wojtys EM. Association between lateral posterior tibial slope, body mass index, and ACL injury risk. *Orthop J Sport Med*. 2017;5(2):1-7. doi:10.1177/2325967116688664

4. Mather RC, Koenig L, Kocher MS, et al. Societal and economic impact of anterior cruciate ligament tears. *J Bone Jt Surg - Am Vol*. Published online 2013. doi:10.2106/JBJS.L.01705

5. Lohmander LS, Englund PM, Dahl LL, Roos EM. The long-term consequence of anterior cruciate ligament and meniscus injuries: Osteoarthritis. *Am J Sports Med*. Published online 2007. doi:10.1177/0363546507307396

6. Beaulieu ML, Carey GE, Schlecht SH, Wojtys EM, Ashton-Miller JA. On the heterogeneity of the femoral enthesis of the human ACL: microscopic anatomy and clinical implications. *J Exp Orthop*. 2016;3(1). doi:10.1186/s40634-016-0050-8

7. Levine JW, Kiapour AM, Quatman CE, et al. Clinically relevant injury patterns after an anterior cruciate ligament injury provide insight into injury mechanisms. *Am J Sports Med*. Published online 2013. doi:10.1177/0363546512465167

8. Boden BP, Dean CS, Feagin JA, Garrett WE. Mechanisms of anterior cruciate ligament injury. *Orthopedics*. Published online 2000. doi:10.3928/0147-7447-20000601-15

9. Lipps DB, Wojtys EM, Ashton-Miller JA. Anterior cruciate ligament fatigue failures in knees subjected to repeated simulated pivot landings. *Am J Sports Med*. 2013;41(5):1058-1066. doi:10.1177/0363546513477836

10. Chen J, Ahn T, Colón-Bernal ID, Kim J, Banaszak Holl MM. The Relationship of Collagen Structural and Compositional Heterogeneity to Tissue Mechanical Properties: A Chemical Perspective. *ACS Nano*. 2017;11(11):10665-10671. doi:10.1021/acsnano.7b06826

11. Veres SP, Harrison JM, Lee JM. Mechanically overloading collagen fibrils uncoils collagen molecules, placing them in a stable, denatured state. *Matrix Biol*. 2014;33:54-59. doi:10.1016/j.matbio.2013.07.003

12. Zitnay JL, Li Y, Qin Z, et al. Molecular level detection and localization of mechanical damage in collagen enabled by collagen hybridizing peptides. *Nat Commun*. 2017;8:1-12. doi:10.1038/ncomms14913

13. Qu D, Subramony SD, Boskey AL, Pleshko N, Doty SB, Lu HH. Compositional mapping of the mature anterior cruciate ligament-to-bone insertion. *J Orthop Res*. 2017;35(11):2513-2523. doi:10.1002/jor.23539

14. Benjamin M, Toumi H, Ralphs JR, Bydder G, Best TM, Milz S. Where tendons and ligaments meet bone: Attachment sites ('entheses') in relation to exercise and/or mechanical load. *J Anat*. 2006;208(4):471-490. doi:10.1111/j.1469-7580.2006.00540.x

15. Kadler KE, Holmes DF, Trotter JA, Chapman JA. Collagen fibril formation. *Biochem J*. 1996;316(1):1-11. doi:10.1042/bj3160001

16. Shoulders MD, Raines RT. Collagen structure and stability. *Annu Rev Biochem*. 2009;78:929-958. doi:10.1146/annurev.biochem.77.032207.120833

17. Dazzi A, Prater CB. AFM-IR: Technology and applications in nanoscale infrared spectroscopy and chemical imaging. *Chem Rev*. 2017;117(7):5146-5173. doi:10.1021/acs.chemrev.6b00448

18. Campagnola P. Second harmonic generation imaging microscopy: Applications to diseases diagnostics. *Anal Chem*. 2011;83(9):3224-3231. doi:10.1021/ac1032325

19. Latour G, Robinet L, Dazzi A, Portier F, Deniset-Besseau A, Schanne-Klein MC. Correlative nonlinear optical microscopy and infrared nanoscopy reveals collagen degradation in altered parchments. *Sci Rep*. 2016;6(April):1-10. doi:10.1038/srep26344

20. Chen X, Nadiarynkh O, Plotnikov S, Campagnola PJ. Second harmonic generation microscopy for quantitative analysis of collagen fibrillar structure. Published online 2012. doi:10.1038/nprot.2012.009

21. Kottmann RM, Sharp J, Owens K, et al. Second harmonic generation microscopy reveals altered collagen microstructure in usual interstitial pneumonia versus healthy lung. *Respir Res*. 2015;16(1):1-13. doi:10.1186/s12931-015-0220-8

CHAPTER 2

Hierarchical Detection and Assessment of Material Fatigue Damage of the Human Anterior Cruciate Ligament caused by Repetitive Sub-maximal Mechanical Loading

Based on Junjie Chen, Jinhee Kim, Wenhao Shao, Stephen H. Schlecht, So Young Baek, Alexis K. Jones, Taeyong Ahn, James A. Ashton-Miller, Mark M. Banaszak Holl, Edward M. Wojtys. An ACL Failure Mechanism. American Journal of Sports Medicine. 2019, 47 (9):2067-2076

2.1 Introduction

It is well recognized that most ACL injuries, nearly three quarters, occur without contact even in a high collision sport such as NFL football.[6] Hypotheses proposed to explain the mechanism of non-contact ACL injury include aggressive quadriceps loading [14] excessive joint compressive loading,[20] awkward landing or decelerating maneuvers,[7] neuromuscular control deficit[12] and the induction of macroscopic tissue damage from repetitive sub-maximal ligament loading after simulated strenuous jump landings.[26]

The ACL consists of dense connective tissue whose major component is type I collagen.[22] Those fibril forming collagen molecules are assembled in a hierarchical order into ligaments.[8] This hierarchical assembly starts with collagen molecules aggregating to collagen fibrils at the nanometer scale, to collagen fibers at the micrometer scale, and eventually aggregate into bundles to form ligament at the macroscale. Disruption of the collagen helical assembly results in reduced tensile strength and abnormal development of the collagen fibrils.[9]

Among all characterization methods, magnetic resonance imaging (MRI) is the most commonly used tool for the clinical diagnosis of ACL injury.[21] While MRI may also someday have the potential to detect molecular, nano- and micro-level damage, the challenge of conducting the appropriate MRI experiment and interpreting those results remains. Widely used research techniques include microCT and histology for characterizing ACL "microdamage" with micrometer level spatial resolution.[23] However, these methods fail to inform on any sub-micrometer ACL damage that might exist.

We hypothesized that damage can accumulate in the ACL across the different hierarchical levels ranging from the molecular to micrometer level, and that this damage could be responsible for the ACL failures observed *in vitro* and *in vivo*.[26] To test this hypothesis, we investigated molecular level collagen unravelling using AFM-IR and CHP-TAMRA, nanometer level collagen fibril damage using AFM, and micrometer level collagen fiber damage using SHIM in both mechanically tested cadaveric ACLs and injured ACLs of patients.

Most orthopaedic studies focus on the acute triggers of ACL injury, in accord with the view that non-contact ACL injury is caused by a single overload of a normal ligament.[13] Fewer studies have explored the development of pre-injury ACL damage caused by repetitive, sub maximal loading[26] that does not exceed the ligament ultimate tensile strength.[2] In this study, we address two key questions: 1) what is the chemical and structural nature of any damage incurred in a cadaver ACL during repeated simulated jump landings compared to its untested contralateral knee, and 2) is the damage signature observed in the cadaveric specimens comparable to that observed in patient ACLs that failed in a noncontact mechanism?

We previously demonstrated *in vitro* that the ACL can experience fatigue failure in fewer than 100 repeated jump landings when internal femoral rotation is limited.[18] The characterization of ACL microstructural change at the femoral enthesis in one of each pair of

cadaver knees having been subjected to a repetitive loading regimen was the major focus of that earlier work. The work herein provides characterization of ACL damage from knees subjected to similar loading tests at multiple levels of the collagen hierarchical structure: namely at the molecular, nanoscopic and microscopic levels.

2.2 Methods

The multiscale ACL femoral enthesis damage present in paired adult cadaveric knees, one mechanically tested repetitively, the other untested, was evaluated at the molecular, fibril, fiber, and tissue levels. Molecular level ACL damage was observed using atomic force microscopy – infrared spectroscopy (AFM-IR) as an Amide I band shift from 1664 cm^{-1} to 1740 cm^{-1}, consistent with the unravelling or denaturation of the collagen triple helix.[17] Although the sample preparation methods employed did not generate a similar band shift in the control samples, an additional validation test was performed to ensure that the 1740-cm^{-1} band assigned to triple-helix denaturation was not the result of tissue dehydration. This spectroscopic

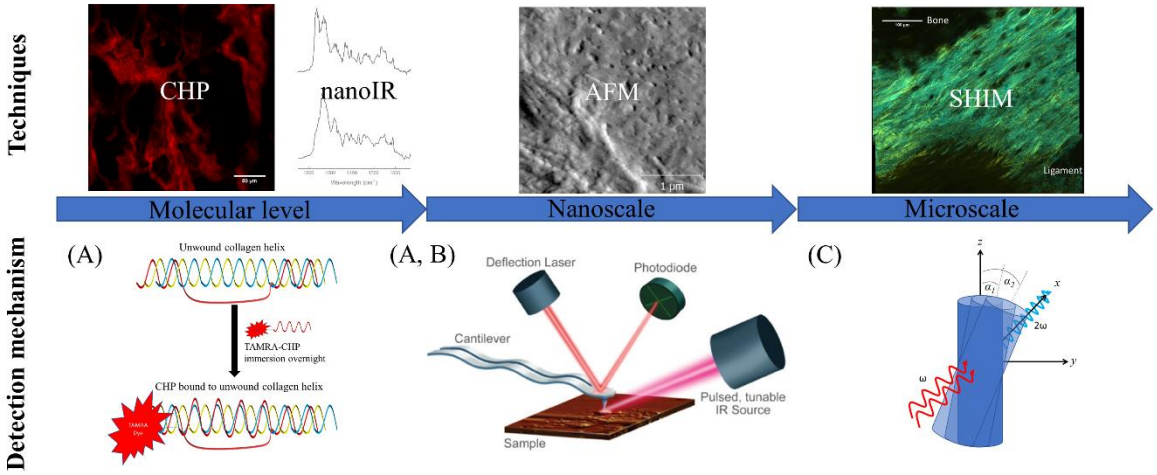

Figure 2.1 *Hierarchical detection of chemical and physical anterior cruciate ligament damage. (A) Mechanical force induces collagen triple-helix unravelling concomitant with the disruption of intra- and intermolecular amino acid chain and water hydrogen bonding. CHP-TAMRA binds to the unravelled collagen strands and is detected by fluorescence microscopy. AFM–infrared spectroscopy is also used to detect collagen triple-helix unravelling via the distinctive infrared band at 1740 cm-1. (B) AFM is utilized to detect nanoscale topographical defects at the ~30- to 100-nm scale, which is similar to the size of collagen fibrils. Figure for AFM-IR schematic reprinted with permission from received from Bruker Corp. (C) Second harmonic imaging microscopy imaging is employed to detect regions of dis- ordered collagen at the 10- to 100-mm scale, which is similar in size to collagen fibers. AFM, atomic force microscopy; CHP, collagen hybridizing peptide; IR, infrared; SHIM, second harmonic imaging microscopy; TAMRA, carboxytetramethylrhodamine.*

assignment of the 1740-cm^{-1} band was confirmed with a carboxytetramethylrhodamine (TAMRA) dye conjugated to a fluorescent CHP probe that specifically binds to single- stranded collagen associated with denatured helices.[26] Fibril-level collagen nanoscopic damage was further characterized as a reduction in surface topological height ranging from 30 nm to 100 nm in diameter. Fiber- to tissue-level collagen microscopic damage was characterized as 10- to 100-mm regions of disordered collagen per SHIM. A summary of the hierarchical detection scheme is shown in Figure 2.1[a]. Explants removed from the femoral enthesis of failed ACLs in 5 injured patients were also examined for multi-scalar damage signatures to cross-check whether they were consistent with signatures from the tested cadaveric knees.

2.2.1 ACL cadaver samples and jump landing simulation

Seven pairs of cadaveric knees were acquired from adult donors (Table 2.1) at the University of Michigan Medical School and Gift of Life Michigan within 48 hours of death. Use of all human tissue was approved by the University of Michigan Institutional Review Board and given exempt status. Upon tissue harvesting, knees were stored at –20°C. One of each pair of knees was randomly selected for repetitive mechanical loading, while the contralateral knee was reserved as an internal untested control. The paired knees were set to thaw for 48 hours at room temperature before use. The

Table 2.1 *Demographic donor information*

Specimen	Sex	Age, y	Cause of Death
Tested cadaveric donors			
T1	F	57	COPD
T2	M	43	Strangulation
T3	M	64	Liver cancer
T4	F	36	Drug overdose
T5	M	36	Drug overdose
T6	M	34	Cardiac arrest
T7	F	31	Drug overdose
Untested cadaveric donors			
C1	F	21	Alcohol poisoning
C2	M	40	Unknown
C3	F	21	Head trauma
C4	F	26	Drug overdose
C5	M	28	Cardiac arrest
Injured patient donors			
P1	F	44	12 wk
P2	F	40	12 wk
P3	M	45	5 wk
P4	F	16	12 wk
P5	F	44	20 wk

[a]Cadaveric donor knees had no external signs of surgery or trauma upon inspection and palpation. Donors were kept refrigerated upon death. Injured patient tissue was placed in saline and refrigerated immediately. COPD, chronic obstructive pulmonary disease; F, female; M, male.

[a] Figure 2.1 made by Jinhee Kim.

knee chosen for mechanical testing was dissected down to the knee capsule, with care taken to leave intact the ligaments and tendons of the quadriceps (rectus femoris muscle), medial hamstrings (semitendinosus, semimembranosus, gracilis muscles), lateral ham- strings (biceps femoris muscle), and medial and lateral heads of the gastrocnemius muscle. After dissection, the paired knees were stored at 4°C until testing. Just before testing, the proximal femoral and distal tibial and fibular diaphyses were cut to a length of 20 cm from the joint line, and the bone extremities were potted in PMMA (poly- methylmethacrylate). Once the PMMA cured, the knee was mechanically tested with a custom-built apparatus to simulate repeated single-legged pivot landings with a 4 times– body weight impulsive load that combines knee compression, knee flexion, internal tibial torque, and trans-knee muscle force loads as described previously.[4] Each tested knee was subjected to cyclic loading until ACL failure or until a minimum of 100 loading trials were completed. After mechanical testing, the femoral portion of the ACL and its enthesis were removed from both the tested cadaveric knee and its contralateral control with the same tools and methods employed during ACL reconstructive surgery. With an ‘‘outside-in’’ approach, the femoral explant was reamed with a 10-mm trephine (Figure 2.2), placed in normal saline, and stored at 4°C until cryoembedding and sectioning. To determine whether the fatigue damage generated in vitro was comparable to that generated in vivo, ACL explants from 5 patients who had suffered a noncontact ACL injury within the past 3 months requiring primary ACL reconstructive surgery were analyzed (Table 2.1). In preparation for receiving a bone–patellar tendon–bone graft, the native femoral and tibial remnants of the ACL and its associated entheses were removed with the same surgical and storage protocols applied to the cadaveric tissue.

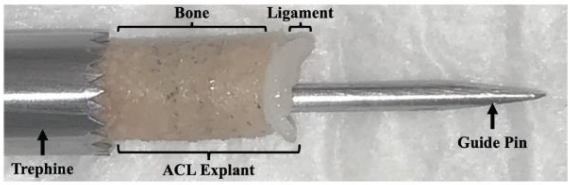

Figure 2.2 *View of the anterior cruciate ligament (ACL) explant and equipment used in the outside-in extraction procedure for both patients and cadavers.*

2.2.2 Preparation of ACL explants[b]

Before imaging, the cadaveric and patient ACL explants were longitudinally sectioned in half with a pathology diamond band saw (model 312; EXAKT Technologies, Inc). Each half was embedded in a water-soluble Super Cryo Embedding Medium (Section-Lab Co), and 20 mm–thick sections were cryosectioned (model 3050S; Leica Biosystems, Inc) with a tungsten carbide blade (TC-65; Leica Microsystems, Inc) set at an 8° angle at –25°C. The sectioned tissue was transferred to adhesive tape via the Kawamoto method[15,16] and stored in a moisturized chamber at –20°C until imaged. Immediately before imaging, sectioned sample slices were immersed in deionized water to remove the embedding media and to keep the sample hydrated. Sections were cut to a ~2-cm square and glued to a stainless- steel AFM sample puck for AFM and AFM-IR imaging.

2.2.3 AFM and AFM- IR studies[c]

The AFM-IR data were collected with a NanoIR2 system (Anasys Instruments). AFM images were taken on a 5 x 5–μm area at a 0.8-Hz line scan rate with 512 x 512–pixel density under contact mode with nIR2 probes (parameters: gold-coated silicon cantilever; nominal radius, 25 nm; force constant, 0.07-0.4 N/m; resonance frequency, 13 ± 4kHz). Four IR spectra

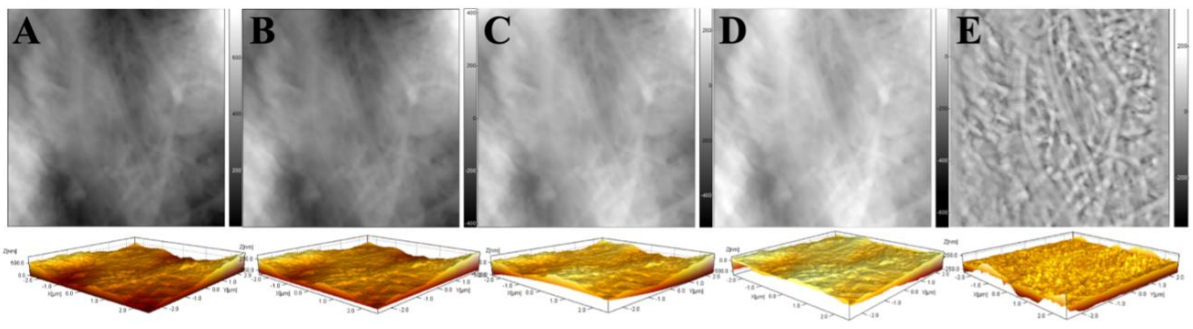

Figure 2.3 *Raw AFM image processing steps on the Scanning Probe Image Processor (A) Raw AFM topography image and corresponding 3D viewer with SPIP. The following images are processed in the order of (B) Global levelling, (C) Global bow removal, (D) Linewise bow removal with zeroed background and (F) Statistical difference filter applied where both mean and standard deviation equalization is performed with a window size of 33 pixels. After steps (A) - (E), image contrast is equalized and enhanced all over image with long-range waves and image bow reduced.*

[b] Preparation of ACL explants performed by Junjie Chen and Jinhee Kim
[c] AFM, AFM-IR studies performed by Junjie Chen and Jinhee Kim

were taken at a power of 2.07% and aver- aged for the final data. The detection range was set between 860 and 1900 cm^{-1}. Roughness and pore analysis were performed with Scanning Probe Image Processor software (v 6.7.5; Image Metrology A/S) to quantify the samples' topography thickness and fibril void density, respectively. Four AFM topography images per knee of T4, T5, T6, and T7 explants were analyzed after each raw image was processed per the following steps on the Scanning Probe Image Processor: global levelling → global bow removal → linewise bow removal → zero back- ground → statistical difference filtering (Figure 2.3) [d]. Sample topography thickness was determined by the peak-peak (Sz) roughness parameter, which is defined as the height difference between the highest and lowest pixels in the image. Fibril void density was calculated by dividing the number of voids detected in 1 AFM height image by its image area (25 μm^2). A mean and SD of fibril void density were calculated for the T4 to T7 specimens after the processing of 4 images per knee. The voids were detected via pore analysis under automatic threshold settings and 3 postprocessing parameters (0.03- to 1.0-

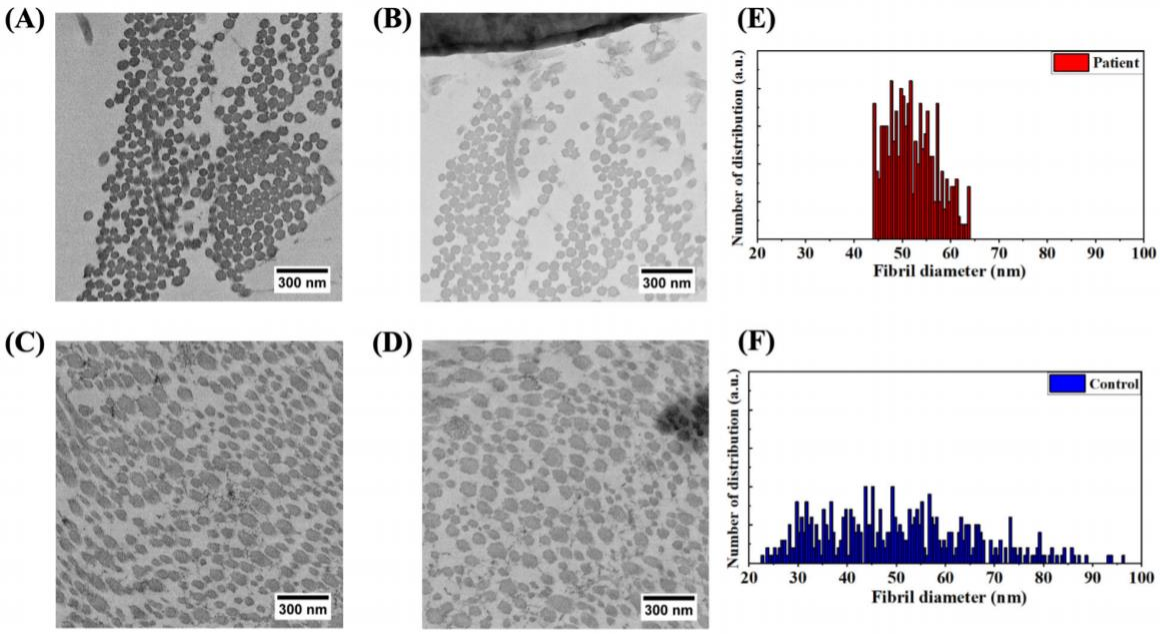

***Figure 2.4**. TEM (JEOL JEM 1400 + Transmission Electron Microscope) studies to quantify human ACL fibril cross section diameter distribution. (A), (B) Cross section image of ACL fibril of 16-year-old female post trampoline injury and its fibril diameter distribution shown in (E). (C), (D) Cross section image of ACL fibril of 28-year-old male cadaver control and its fibril diameter distribution shown in (F). The lower limit of void diameter parameter during pore analysis was selected based on these analyses. Upper limit was set to 1µm to allow room for potential submicron feature detection.*

[d] Figure 2.3 made by Jinhee Kim

mm diameter range, 0.3-1.0 roundness, and 1.0-3.0 aspect ratio). The void diameter range was determined by transmission electron microscopy studies of cross-sectioned human ACL fibril diameters (Figure 2.4) [e].

2.2.4 CHP-TAMRA Fluorescence studies[f]

After AFM and AFM-IR analyses, the samples were stained with a CHP-TAMRA reagent containing a previously published hybridization sequence (Pierce Custom Peptides).[26] The TAMRA fluorophore was selected to avoid spectral overlap with tissue autofluorescence as well as the signal produced by SHIM when employing a laser with 910-nm incident wavelength. Before staining, a 25-mL CHP stock solution (150 mm) was heated at 80°C for 10 minutes to disaggregate the peptide. The solution was quenched by immersion in water for 15 seconds at 4°C. The aliquot was diluted to a total volume of500 mL and pipetted onto the ACL section. The sample was incubated in the dark at 4°C for 12 hours and then rinsed with 13 phosphate-buffered saline before being immersed in Leica type F immersion oil (Leica Microsystems, Inc) for microscopic imaging. Images were collected with a Leica SP8 confocal microscopy system (Leica Microsystems, Inc). The light source was a 910-nm IR laser (10% laser power [LP], 33% gain, 38% offset, pinhole wide open). The TAMRA fluorescence signal was detected at a 570- to 590-nm window on a photo- multiplier detector. A 40x lens was used for imaging 300 x 300-mm image tiles stitched together in a 5 (perpendicular to enthesis) x3 (along with enthesis) area automatically to cover a wide area.

2.2.5 SHIM studies[g]

Microscopic images were collected with a Leica SP8 confocal microscopy system and the type F immersion oil as described earlier. The light source was a 910-nm Coherent

[e] Figure 2.4 made by Jinhee Kim
[f] CHP-TAMRA studies performed by Junjie Chen and Jinhee Kim
[g] SHIM studies performed by Junjie Chen and Jinhee Kim

Chameleon 2-photon IR laser (10% LP, 33% gain, 38% off- set, pinhole wide open). Two photomultiplier detectors were set at 440 nm for the detection of SHIM forward/ backward signal. The signal from forward channels was colored cyan, while that from the backward channel was colored yellow to increase contrast. All Z planes (8.6 mm each) were scanned to cover the entire tissue thickness across the scanning area. Similar to the CHP study, a 40x lens was used for SHIM imaging, and image tiles with a 300 x 300-mm area were stitched together creating a 5 (perpendicular to enthesis) x 3 (along with enthesis) tile area. The mean intensity of a 100 x 100–mm area of SHIM and TAMRA images was measured for both the mechanically tested and contralateral control knees. The TAMRA fluorescence and SHIM signal of paired untested cadaveric knees were also measured to determine the extent of normal signal variation between knees (Table 2.1). The intensity values of SHIM and TAMRA images for

	CHP-TAMRA Intensity		SHIM Channel Intensity	
Specimen	**Left**	**Right**	**Left**	**Right**
C1	6.5 ± 3.4	6.6 ± 3.6	106.4 ± 42.0	127.7 ± 48.7
C2	12.1 ± 7.0	8.5 ± 11.6	36.7 ± 14.6	43.4 ± 17.7
C3	7.6 ± 8.5	5.3 ± 8.2	41.8 ± 22.8	33.6 ± 17.3
C4	7.9 ± 1.6	7.4 ± 1.9	196.7 ± 82.5	164.7 ± 31.3

***Table 2.2**. CHP-TAMRA and SHIM backward channel intensity data for the mechanically untested control knees. Sample C2 is male and C1 and C3-4 are females. These results show the signal variation within the same pair of knees; however, the difference is very low compared to mechanically tested knees which are 2 - 5-fold higher than the control pair.*

mechanically tested knees were reported as a percentage of its contralateral control, set as the baseline intensity, as a way to control for age and other differences in the patient knees. For these untested control knee pairs, the SHIM and TAMRA signal variation was within 20% (Table 2.2). Analysis of disordered or void regions lacking SHIM signal was done on a total of 5 x 3 tiles for each sample, covering a total area of 1500 x 900 μm (1,350,000 μm^2). The diameter and density of disordered regions were quantified with ImageJ and a particle analysis macro (National Institutes of Health). For each knee, 1 tiled SHIM image (as stated earlier) with the best resolution in the forward or backward channel was selected. Then, the grayscale threshold was adjusted to include as much of the disordered regions as possible with limited

noise. Finally, particle analysis was performed with a detection diameter of 100 μm and an infinity and roundness setting of 0.5 to 1.0 to avoid detecting elongated shadows.

2.2.6 Statistics[h]

Based on an a priori power analysis estimated to detect a difference in fibril void density between mechanically tested (ipsilateral) and control (contralateral) specimens at a power of 0.8, given an alpha of .05 and an effect size of 1.1, a sample size of 4 paired knees was required (we included 5 pairs in our study). According to an a priori power analysis estimated to detect at least a 2-fold difference in topography thickness between mechanically tested (ipsilateral) and control (contralateral) specimens at a power of 0.8, given an alpha of .05 and an effect size of 1.6, a sample size of 4 paired knees was required (we included 5 pairs in our study). Based on an a priori power analysis estimated to detect at least a 2-fold difference in SHIM intensity between mechanically tested (ipsilateral) and control (contralateral) specimens at a power of 0.8, given an alpha of .05 and an effect size of 0.8, a sample size of 7 paired knees was required (we included 7 pairs in our study). According to an a priori power analysis estimated to detect at least a 2-fold difference in CHP-TAMRA intensity between mechanically tested (ipsilateral) and control (contralateral) specimens at a power of 0.8, given an alpha of 0.05 and an effect size of 0.8, a sample size of 7 paired knees was required (we included 7 pairs in our study). Therefore, the number of samples included in each multi-scalar damage assessment was sufficient for testing the null hypothesis. Paired t tests were performed to test for significant differences in fibril void density, topography thickness, SHIM intensity, and CHP-TAMRA intensity between paired tested and untested cadaveric knees. Statistical analyses were not performed for patient samples, owing to the lack of control samples.

[h] Statistical analysis performed by Jinhee Kim

2.3 Results

2.3.1 Molecular-Level Ligament Damage Detected by AFM-IR and CHP-TAMRA

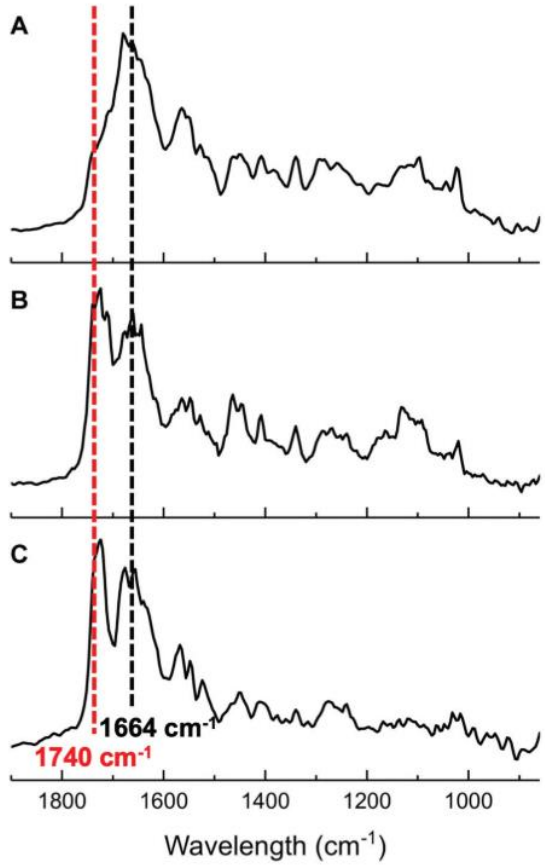

Figure 2.5 *Atomic force microscopy–infrared spectroscopy spectra of tissue at the anterior cruciate ligament (ACL) femoral enthesis from (A) nonmechanically tested cadaveric ACL control, (B) mechanically tested cadaveric ACL, and (C) clinically injured patient ACL. The 1740-cm^{-1} (light dashed line) disordered collagen band was prominently observed for the mechanically tested and patient sample, while only the nor- mal 1664-cm^{-1} (dark dashed line) collagen backbone band was most prominent for the untested cadaveric ACL control.*

Healthy, normal-looking ACLs should exhibit an IR spectrum with the strongest signal at 1664 cm-1, the amide I band from the protein backbone (Figure 2.5A). Indeed, the IR spectrum from the untested cadaveric ACL controls is almost identical to that reported by Spalazzi et al.24 How- ever, a strong 1740-cm^{-1} feature emerges after mechanical testing (Figure 2.5B). The 1740-cm^{-1} band is a chemical signature of a disrupted collagen backbone structure (Figure 2.6).[17] Computational studies of stabilization of collagen-like peptides in water revealed that the stability is provided by interstitial water bridges anchoring amine-carbonyl (δ bridges: N – H ••Wn••O=C), which are further stabilized by polar –OH side chain of Hydroxyproline (Hyp) through H-bonding with water.[5,10] Molecular dynamics simulation calculates that the average residence time of waters on external hydration sites (from Hyp and exposed carbonyl groups) of the triple helix is 50 ps, while the δ bridge waters exhibited a residence time >100 ps.[2] Another molecular dynamics simulation exploring water gelation around collagen triple helix shows that radial distribution function of O – H became distorted under 4 A˚ , followed by deformation of a tetrahedral

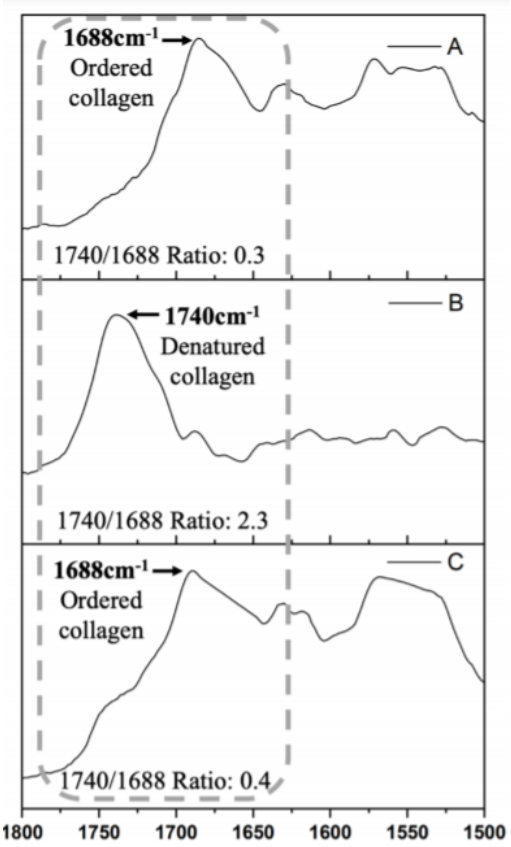

***Figure 2.6**. Reversibility of 1740 cm^{-1} peak with N_2 gas dehydration and water rehydration. (A) Normal ligament exhibits an ordered collagen peak 1688 cm^{-1} and a low disordered (1740 cm^{-1}) / ordered (1664 cm^{-1}) IR amplitude peak ratio of 0.3. (B) Dehydrated ligament subjected to N2 gas for 3 minutes exhibits a strong 1740 cm^{-1} peak and a high disordered (1740 cm^{-1}) / ordered (1664 cm^{-1}) ratio of 2.3. (C) Immediate hydration of ligament with 5 drops of DI water exhibits a reversed 1740 cm^{-1} peak back to 1688 cm^{-1}, producing a low disordered (1740 cm^{-1}) / ordered (1664 cm^{-1}) ratio of 0.4.*

network of hydrogen bonds in the kinetically labile first hydration shell.[11] Based on these studies, the mechanical forces leading to weakened δ bridges and destabilization of the triple helix will generate an effective local dehydration of the collagen molecules that is consistent with our localized observation of the 1740-cm^{-1} band, as illustrated in Figure 2.6[i]. This effect generates change in the stochiometric amount of water associated in a bonding fashion with collagen triple helix and has a significant effect on spectroscopic signature as well as structural and mechanical properties. We believe that it is most useful to view this as chemical change of the material. It is worth noting that the 1740-cm^{-1} band was also observed in the explants from the ruptured patient ACLs obtained before surgical reconstruction (Figure 2.5C). In the discussion, we argue that this similarity in collagen backbone disruption suggests that the ACLs from the patients may also have been subjected to severe repetitive loading cycles. To confirm the spectroscopic assignment of the 1740-cm^{-1} band, a fluorescent CHP conjugated to a TAMRA dye was deployed. The peptide sequence is GGG(GPO)9 with a fluorescent TAMRA dye conjugation on the N-terminus (G-glycine, P-proline, O-hydroxyproline). The TAMRA dye has an excitation wavelength at 551 nm and a maximal emission at 576 nm, which effectively avoided the interference from the possible collagen autofluorescence. The CHP sequence resembles the

[i] Figure 2.6 made by Jinhee Kim

sequence of type I collagen, offering a specific strong binding toward dissembled collagen molecules, as demonstrated by Zitnay et al.[26] After mechanical testing, the mean percentage intensity of the CHP-TAMRA probe was at least twice that of the untested contralateral controls (P = .02) (Figure 2.7). This indicates the disruption of the collagen triple-helical structure by unraveling of the collagen molecule after the repeated mechanical loading. Taken with the AFM-IR data, this provides strong evidence of collagen fatigue damage at the molecular level. To further probe the nature of the chemical and structural change associated with the collagen triple-helix disruption, we dehydrated fresh human ACL at 22°C by exposure to a stream of N_2 for 7 days. Dehydration under these conditions resulted in almost complete disruption of the collagen triple helices in the sample, as indicated by the almost complete replacement of the 1688-cm^{-1} band by the 1740-cm^{-1} band (Figure 2.6). This indicates that the 1740-cm^{-1} band can arise from a number of chemical and structural changes, including

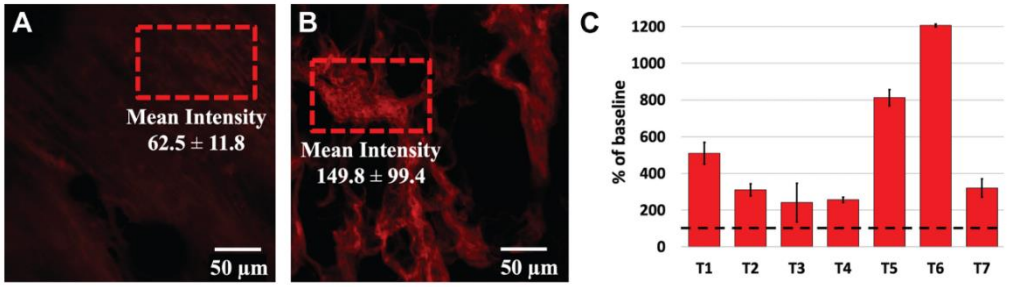

Figure 2.7 *Representative fluorescent images of CHP-TAMRA binding at the femoral enthesis of the ACL in (A) an untested control knee and (B) a mechanically tested knee. Red dashed boxes represent the 5 x 3 tile regions of interest analyzed for pairs of knees. (C) The ACL CHP-TAMRA fluorescent intensity was compared between the tested and untested knee regions of interest and normalized as an intensity ratio. Values are presented as mean 6 SD. Black dashed line represents the baseline intensity for the untested control knees. ACL, anterior cruciate ligament; AFM, atomic force microscopy; CHP, collagen hybridizing peptide; TAMRA, carboxytetramethylrhodamine.*

breaking of the internal amino acid hydrogen bonding, inter- and intramolecular hydrogen bonding with water, and a change in the collagen triple helix:water stoichiometric ratio. This dehydration experiment suggests that water is an integral part of the collagen triple-helix structure and an important component of the ‘‘collagen molecule,’’ as it is present in ligamentous tissue.

2.3.2 Ligament nanodamage detected by AFM

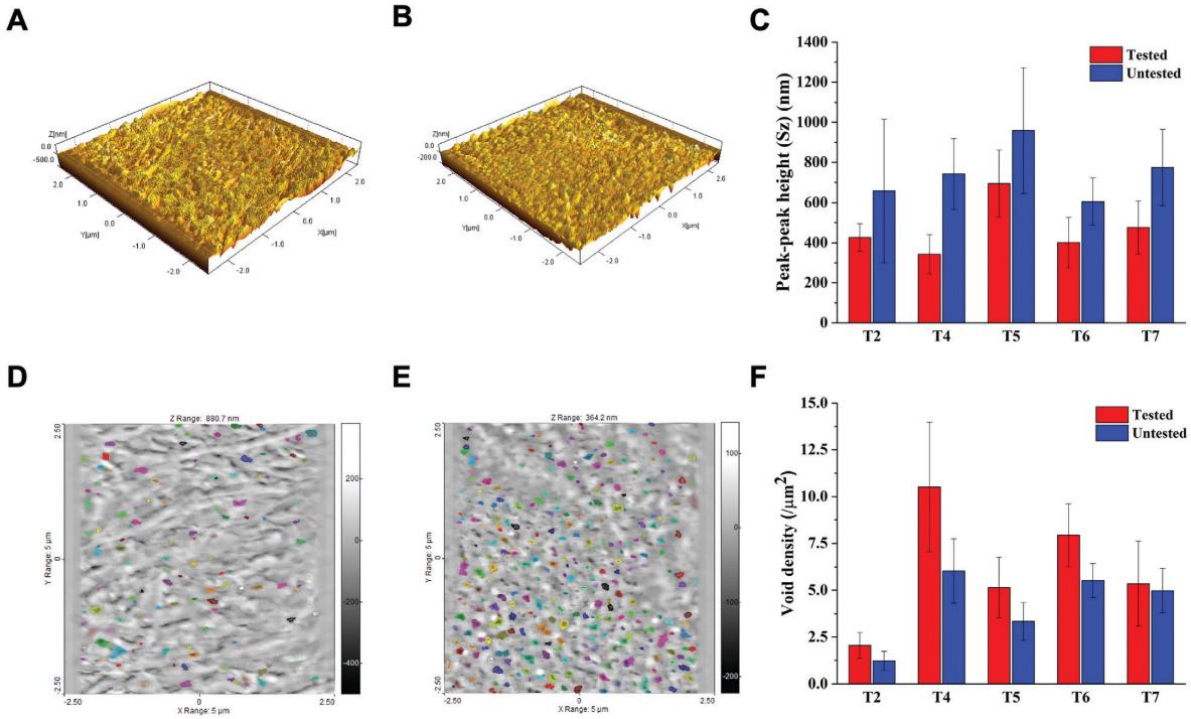

Figure 2.8 *Representative 3-dimensional views of postprocessed atomic force microscopy topography images of (A) untested control knee and (B) tested knee and void density plots of (D) untested control knee and (E) tested knee of T4 donor (colors are only for visualization of the voids). (C) A comparison of the mean 6 SD topography thickness for tested and untested knee images for T2 and T4 to T7. (F) A comparison of the mean 6 SD void density for the same sample set as in panel C, highlighting that tested knees were denser in fibril voids as compared with nontested knees.*

Type I collagen molecules assemble into nanometer-level collagen fibrils and further stack into micrometer collagen fibers. At the nanometer scale, AFM is a commonly used tool for studying collagen order and morphology. After mechanical testing, the mean surface thickness decreased ($P < .01$) (Figure 2.8C)[j] and a 49% higher mean fibril void density ($P = .06$) was observed when compared with untested contralateral controls (Figure 2.8F). Similar fibril voids were also repeatedly observed in the patient specimens (Figure 2.9A) and the submaximally loaded cadaveric ACLs (Figure 2.9B) as compared with the cadaveric control specimens (Figure 2.9C). These fibril voids were distributed across a size range from ~30 nm to 100 nm, often with similar shapes and consistent with the range of ACL fibril width measured with cross-sectional transmission electron microscopy (Figure 2.4). All AFM void

[j] Figure 2.8 made by Jinhee Kim

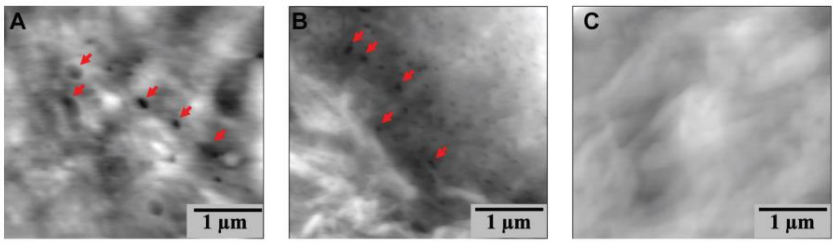

Figure 2.9 *Representative atomic force microscopy images (height) of fibril voids in the anterior cruciate ligament (ACL) associated with mechanically induced nanoscale damage. The holes with darker contrast (red arrows) are locations without the presence of collagen molecules. (A) Explant from patient ACL femoral enthesis at the time of surgical reconstruction. (B) Mechanically tested cadaveric ACL femoral enthesis. (C) Untested cadaveric contralateral (control) ACL femoral enthesis.*

distribution analyses were performed on images that covered a 5 x 5–µm^2 area. The mechanically tested samples overall had 6 ± 3 voids/ µm^2 as compared with 4 ± 2 voids/ µm^2 for the untested controls, for a mean increase of about a factor of 2. Specifically, individual evaluation of samples, except T7, showed a range of 40% to 75% of fibril void density increase as compared with that of their contralateral controls (Figure 2.8F). Since the fibril voids were observed in the mechanically tested cadaveric knees, where biological activity had ceased, those fibril voids could not have resulted from postinjury responses such as lipid infiltration or collagen regeneration. The increase in the presence of fibril voids correlated with a concomitant decrease in surface thickness, as measured by the peak-peak (Sz) roughness parameter from a mean 750 ± 150 nm for the control samples to 430 ± 150 nm for the mechanically tested samples (Table 2.3).

	Peak-Peak Height, Sz (nm)		Fibril Void Density (µm^2)	
T2 Specimen	Tested	Untested	Tested	Untested
T4	342± 98	742 ± 177	11 ± 3	6 ± 2
T5	694 ± 167	959 ± 314	5 ± 2	3 ± 1
T6	401 ± 126	605 ± 117	8 ± 2	6 ± 1
T7	476 ± 132	775 ± 189	5 ± 2	5 ± 1

Table 2.3. *Comparisons of average peak-peak height (Sz) and fibril void density of four sets of paired knee images per sample.*

2.3.3 Ligament microdamage detected by SHIM

Since evidence of ACL femoral enthesis damage at the molecular level and nanometer level was observed, we then extended the study to see if damage also occurred at the micrometer or fiber level. Collagen molecules are well-aligned biopolymers that can be

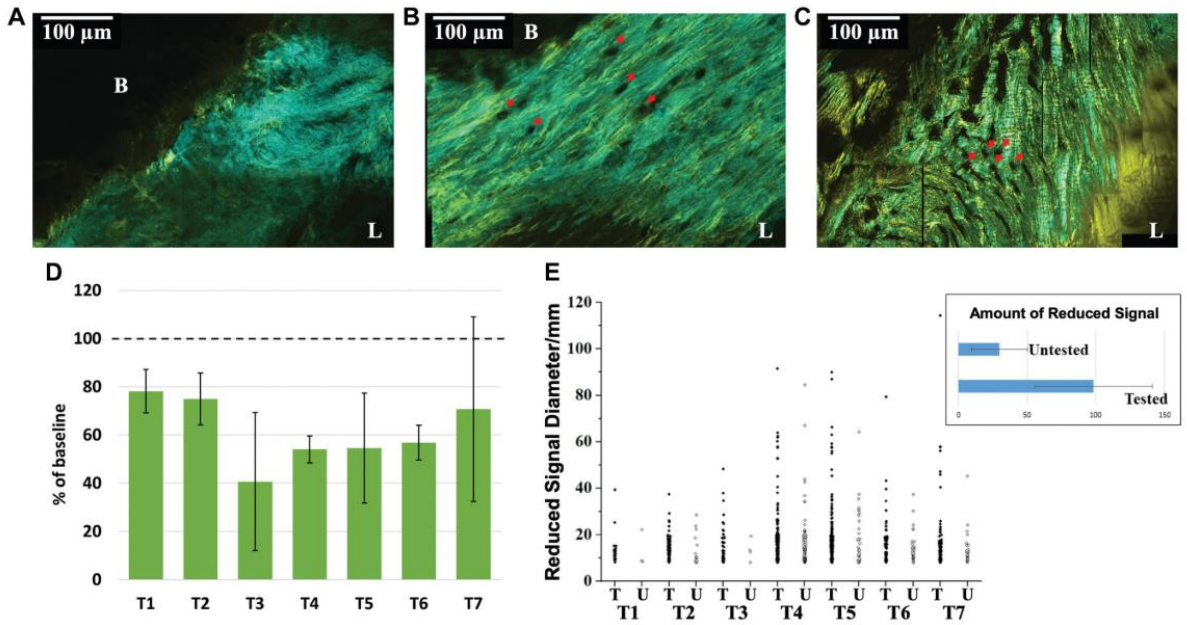

Figure 2.10 *SHIM images from the ACL femoral enthesis: (A) untested cadaveric ACL control femoral enthesis, (B) mechanically tested cadaveric ACL femoral enthesis, and (C) explant from patient ACL femoral enthesis at the time of surgical reconstruction. Red arrows indicated regions of reduced second harmonic signal induced by mechanical damage. (D) The SHIM signal intensity was also reduced after the mechanical testing as compared with the untested contralateral control ACL enthesis. Black dashed line represents the base- line intensity for the untested control knees. (E) Distribution of reduced SHIM signal areas in the femoral ACL enthesis of the mechanically tested knees (T) and the corresponding controls (U). Values are presented as mean 6 SD. ACL, anterior cruciate ligament; B, bone; L, ligament; SHIM, second harmonic imaging microscopy.*

specifically detected by SHIM. SHIM exhibited micrometer-scale regions of reduction in signal (Figure 2.10D) for both the mechanically tested (Figure 2.10B) and patient (Figure 2.10C) explants, indicating the absence of organized collagen fibers. In contrast, there was less ligament disruption in the untested cadaveric control (Figure 2.10A). A comprehensive analysis showed that the mechanically tested ACLs contained 10- to 100-µm regions of reduced signal (Figure 2.10E). The distribution and size of these regions were extracted from interest areas covering the same size (see Methods). The quantification for the disrupted region density showed that, for every square millimeter sample, the mechanically tested ligament had 73.0 ± 42.8 disrupted regions, roughly 3 times the density of untested control at 22.2 ± 20.3 (Figure 2.10E inset). The mean percentage intensity values of mechanically tested samples significantly differed from that of contralateral controls ($P<.01$), as well as the mean number of SHIM signal areas ($p =.01$).

2.4 Discussion

These results, acquired from different analytical tools (AFM, AFM-IR, fluorescence microscopy, SHIM), provide the first independent evidence of hierarchical multiscale damage at the ACL femoral enthesis induced by strenuous repetitive impulsive knee loading known to place the ACL under significant strain in vitro.[25] These damage signatures were compared with explants acquired from patients who had an ACL injury to determine whether their tissue would exhibit the same characteristics. Indeed, the same indicators of multiscalar material fatigue damage were seen at the femoral enthesis of torn ACLs obtained from these patients. This finding suggests that the failure of the femoral ACL enthesis in these patients may be due to an accumulation of material fatigue damage of collagen fibrils and fibers resembling an injury from prior ACL multiscalar damage that has not had sufficient time to repair. It was induced by too many severe ACL loading cycles in a time frame inadequate for any physiological repair mechanisms to restore ligament homeostasis before the next severe loading cycle. The potential for ACL repair at the molecular, nanoscale, or microscale, if it exists in children and/or adults, remains unknown. However, others have shown that in the tendon that rests after the initiation of fatigue damage, there is a capacity for the extracellular matrix within the midsubstance to remodel once activity is reinitiated.[1]

The present experimental study found evidence of structural and chemical degeneration at the femoral enthesis of the ACL, the same location previously shown to be particularly prone to failure under repetitive loading in vitro as well as in vivo.[18] Moreover, the finding of failure at this entheseal location is consistent with purely theoretical analyses demonstrating a strain concentration in the ACL ligament at its femoral enthesis.[19] This strain concentration increased with the acuteness of the ligament attachment angle with the femur as well as with the concavity of the femoral enthesis.[3] So, the aforementioned theoretical study shows that the ACL femoral enthesis contains a region that has a strain concentration, and this study shows that hierarchical

damage can accumulate in that region under a particular ACL loading regimen. Further studies are needed to determine whether this is where ACL fatigue failure indeed initiates.

Another important observation is that our results support the hypothesis that ACL multiscalar damage can result from submaximal mechanical loading and that damage can accumulate under realistic repetitive loading to eventually become a risk factor for ACL injury. ‘‘Realistic’’ here means a knee loading that has previously been shown to have the same magnitude and time course as a real jump landing. Nanoscopic detection of collagen unravelling observed by the 1740-cm^{-1} peak and CHP-TAMRA probe is consistent with the observation of a reduced SHIM signal, which identifies microscopic domains where this is occurring at a greater concentration. Similarly, the reduction in surface topological height (Sz) is also consistent with the unravelling of collagen fibrils—a value that appears largely controlled by the dimensional scale of the collagen fibril widths. Questions that remain to be answered by future studies include the following: (1) How does molecular-level collagen triple-helix unravelling relate to the observed fibril voids and decrease in surface thickness? (2) What contributes to the formation of microscopic regions of fibril disruption? (3) How are all these features associated with clinical diagnosis on MRI and, ultimately, ACL failure? The combination of AFM-IR, CHP-TAMRA, and SHIM data indicates that the collagen triple helix has unravelled into individual strands. Thus, glycine-proline intramolecular hydrogen bonding has been broken in addition to the water hydrogen bonding that is integral to the collagen structure. Our control experiments indicate that these changes are also consistent with local changes in triple-helix/water stoichiometry. Thus, we ascribe the observed changes to both their structural and their chemical nature. We believe that this wider perspective of the nature of multiscalar damage is important for the design of future studies to understand the physiological repair mechanism of this damage as well as the changes in biomechanics that lead to ACL failure.

The presence of fibril voids in the tested knees and patients as well as, to a lesser degree, in the control knees is interesting. We hypothesize that each void represents an individual collagen fibril in the ligament rupturing and pulling out during loading, leaving a fibril-sized void in the ligament. The presence of these voids in the untested control knee ACLs suggests that pre-existing damage was present in the ACL that accumulated in these donors during their lifetimes. Additionally, the measured SHIM intensities were reduced in the mechanically tested knees as com- pared with the corresponding untested paired controls. This indicates that the non-centrosymmetric collagen crystallinity was partially broken during mechanical testing, suggesting another level of ligament damage as a result of the strenuous repetitive impulsive knee loading. These signatures of nano- and microscopic damage can be easily missed in the clinical MRI used for diagnostic purposes. The sum of these hierarchical structural changes corresponds to the multiscalar damage that was hypothesized in, but not directly demonstrated in, the original cadaveric studies of the effects of ACL repetitive loading.[18]

For the purposes of this study, we clarify that ‘‘submaximal repetitive loading of the ACL’’ means knee loading that did not generate enough force in the ACL to fail it during the first knee loading cycle (ie, as evidenced by our data showing >3-mm anterior tibial translation during that loading cycle). Many strenuous sports activities may place large loads on the knee in stopping, turning, cutting, and landing, but only a subset of those will place larger-than-normal loads on the ACL: specifically, those that include substantial internal tibial torques while landing a jump or making acut.[18] Hence, strenuous athletic activity in itself does not necessarily place unusual loads on the ACL and there- fore would not necessarily cause a concerning increase in multiscalar fatigue damage at the femoral enthesis.

Strengths of the study were the randomization of one of each pair of cadaveric knees to mechanical testing, as well as the inclusion of data from the untested contralateral cadaveric knee. Limitations of this study include the small sample size, the nonblinded operators

conducting the structural and chemical studies, and the sole assessment of fatigue damage at the femoral enthesis at the location where proximal failures are most often observed clinically.[25] In the patients included in the present study, 1 to 3 months was the usual time course to ACL reconstruction to allow for knee effusions to dissipate and knee muscle strength to be restored. It is possible that some of the collagen alterations in the patient explants may reflect partially repaired hierarchical damage. However, the same signs of multiscalar damage seen in the mechanically tested cadaveric ACLs were also observed in the patients, supporting our material fatigue hypothesis for ACL failure.

Larger randomized and blinded studies are needed to confirm these results. However, it does appear that the solution to preventing many noncontact ACL injuries may require consideration of the potential for multiscalar collagen fatigue-related damage to accumulate at the ACL femoral enthesis as identified in this article.

2.5 Conclusion

In summary, from each pair of adult cadaveric knees, one of them was randomly selected for repetitive mechanical testing which simulated a single-legged pivot landing with a 4 times bodyweight impulsive load that combines knee compression, knee flexion, internal tibial torque, and trans-knee muscle force loads. The multiscalar ACL femoral enthesis damage present in paired adult cadaveric knees – one mechanically tested and the other untested – was evaluated at the molecular, fibril, fiber, and tissue levels. Molecular-level ACL damage was observed via AFM-IR as an Amide I band shift from 1664 cm^{-1} to 1740 cm^{-1}, consistent with the unravelling or denaturation of the collagen triple helix.[17] This spectroscopic assignment of the 1740-cm^{-1} band was confirmed with a carboxytetramethylrhodamine (TAMRA) dye conjugated to a fluorescent CHP probe that specifically binds to single- stranded collagen

associated with denatured helices.[26] Fibril-level collagen nanoscopic damage was further characterized as a reduction in surface topological height ranging from 30 nm to 100 nm in diameter. Fiber- to tissue-level collagen microscopic damage was characterized as 10- to 100-mm regions of disordered collagen per SHIM. These are the first fatigue damage signatures in the ACL elucidated across the different hierarchical levels of collagen structure, highlighting the shortcomings of the low spatial resolution of MRIs, which is the most common clinical diagnostic tool of ACL injury. Our results suggest that the multiscalar, hierarchical structural changes observed at the femoral ACL enthesis are at least in part responsible for the reduction in structural integrity leading to noncontact ACL failure as a result of strenuous repetitive impulsive athletic maneuvers. These findings suggest that at least some ACL injuries may be attributable to an overuse injury caused by damage that accumulates in the absence of the time needed for repair.

2.6 Acknowledgement

The authors thank the Michigan Integrative Musculoskeletal Health Core and Carol Whitinger for technical assistance with tissue sectioning. They also extend their gratitude to Gift of Life Michigan and University of Michigan Medical School for the cadaveric and donor tissue used in this study.

2.7 References

1. Andarawis-Puri N, Flatow E. Promoting effective tendon healing and remodeling. J Orthop Res. 2018;36:3115-3124.

2. Bates N, Schilaty N, Nagelli C, Krych AJ, Hewett TE. Validation of noncontact anterior cruciate ligament tears produced by a mechanical impact simulator against the clinical presentation of injury. Am J Sports Med. 2018;46:2113-2121.

3. Beaulieu M, Carey G, Schlecht S, Wojtys E, Ashton-Miller J. Quantitative comparison of the microscopic anatomy of the human ACL femoral and tibial entheses. J Orthop Res. 2015;33:1811-1817.

4. Beaulieu M, Wojtys E, Ashton-Miller J. Risk of anterior cruciate ligament failure is increased by limited internal femoral rotation during in vitro repeated pivot landings. Am J Sports Med. 2015;43:2233-2241.

5. Bella J, Brodsky B, Berman HM. Hydration structure of a collagen peptide. Structure. 1995;3:893-906.

6. Boden B, Dean G, Feagin J Jr, Garrett W Jr. Mechanisms of anterior cruciate ligament injury. Orthopedics. 2000;23:573-578.

7. Boden B, Torg J, Knowles S, Hewett TE. Video analysis of anterior cruciate ligament injury: abnormalities in hip and ankle kinematics. Am J Sports Med. 2009;37:252-259.

8. Chen J, Ahn T, Colon-Bernal I, Kim J, Banaszak Holl M. The relation- ship of collagen structural and compositional heterogeneity to tissue mechanical properties: a chemical perspective. ACS Nano. 2017; 11:10665-10671.

9. Danielson K, Baribault H, Holmes D, Graham H, Kadler K, Iozzo R. Targeted disruption of decorin leads to abnormal collagen fibril morphology and skin fragility. J Cell Biology. 1997;136:729-743.

10. De Simone A, Vitagliano L, Berisio R. Role of hydration in collagen triple helix stabilization. Biochem Biophys Res Commun. 2008;372: 121-125.

11. Handgraaf J-W, Zerbetto F. Molecular dynamics study of onset of water gelation around the collagen triple helix. Proteins. 2006;64: 711-718.

12. Hewett T, Myer G, Ford KR, et al. Biomechanical measures of neuro- muscular control and valgus loading of the knee predict anterior cruciate ligament injury risk in female athletes: a prospective study. Am J Sports Med. 2005;33:492-501.

13. Hewett TE, Di Stasi S, Myer G. Current concepts for injury prevention in athletes after anterior cruciate ligament reconstruction. Am J Sports Med. 2013;41:216-224.

14. Houde D, Berkowitz S, Engen J. The utility of hydrogen/deuterium exchange mass spectrometry in biopharmaceutical comparability studies. J Pharmaceut Sci. 2011;100:2071-2086.

15. Kawamoto T. Use of a new adhesive film for the preparation of multi- purpose fresh-frozen sections from hard tissues, whole-animals, insects and plants. Arch Histol Cytol. 2003;6:123-143.

16. Kawamoto T, Kawamoto K. Preparation of thin frozen sections from nonfixed and undecalcified hard tissues using Kawamot's film method. In: Hilton M, ed. Skeletal Development and Repair. Totowa, NJ: Humana Press; 2014:149-164. Methods in Molecular Biology; vol 1130.

17. Latour G, Robinet L, Dazzi A, Portier F, Deniset-Besseau A, Schanne- Klein M-C. Correlative nonlinear optical microscopy and infrared nanoscopy reveals collagen degradation in altered parchments. Sci Rep. 2016;6:26344.

18. Lipps D, Wojtys E, Ashton-Miller J. Anterior cruciate ligament fatigue failures in knees subjected to repeated simulated pivot landings. Am J Sports Med. 2013;41:1058-1066.

19. Luetkemeyer CM, Marchi BC, Ashton-Miller J, Arruda EM. Femoral entheseal shape and attachment angle as potential risk factors for anterior cruciate ligament injury. J Mech Behav Biomed Mater. 2018;30:313-321.

20. Meyer E, Baumer T, Slade J, Smith W, Haut R. Tibiofemoral contact pressures and osteochondral microtrauma during anterior cruciate ligament rupture due to excessive compressive loading and internal torque of the human knee. Am J Sports Med. 2008;36:1966-1977.

21. Ng W, Griffith J, Hung E, Paunipagar B, Law B, Yung P. Imaging of the anterior cruciate ligament. World J Orthop. 2011;2:75-84.

22. Petersen W, Tillmann B. Structure and vascularization of the cruciate ligaments of the human knee joint. Anat Embryol. 1999;200:325-334.

23. Ramme A, Lendhey M, Raya J, Kirsch T, Kennedy O. A novel rat model for subchondral microdamage in acute knee injury: a potential mechanism in post-traumatic osteoarthritis. Osteoarthritis Cartilage. 2016;24:1776-1785.

24. Spalazzi J, Boskey A, Pleshko N, Lu H. Quantitative mapping of matrix content and distribution across the ligament-bone insertion. PLoS One. 2013;8:e74349.

25. Wojtys E, Beaulieu M, Ashton-Miller J. New perspectives on ACL injury: on the role of repetitive sub-maximal knee loading causing ACL fatigue failure. J Orthop Res. 2016;34:2059-2068.

26. Zitnay J, Yang L, Qin Z, et al. Molecular level detection and localiza- tion of mechanical damage in collagen enabled by collagen hybridiz- ing peptides. Nat Comm. 2017;8:14913

CHAPTER 3

Collagen Autofluorescence Detected by Confocal Laser Endomicroscopy as a Sign of Anterior Cruciate Ligament Fatigue Damage

Jinhee Kim, So Young Baek, Stephen H. Schlecht, Melanie Beaulieu, James A. Ashton-Miller, Edward M. Wojtys M.D., Lindsay Bussau, Mark M. Banaszak Holl
(manuscript in preparation)

3.1 Introduction

3.1.1 ACL injury statistics

The anterior cruciate ligament (ACL) connects the distal femur to the proximal tibia in order to help provide stability of the knee joint as it is loaded and moved.[1] In the United States, over 350,000 ACL injuries occur annually with over half being in young athletes 15 to 25 years of age.[2,3] Due to the poor healing capacity of ruptured ligaments,[4] an ACL reconstruction is often performed using a replacement graft from part of the patient's patella or hamstring tendon.[1] Despite this treatment, 20% of patients experience re-injury and over 50% of patients develop osteoarthritis within 10 – 20 years after injury, inducing pain and functional impairment.[2] Thus, young athletes who sustain an ACL injury face the prospect of chronic pain throughout their adulthood.[5] In order to head off these sequelae, one needs a way of evaluating ACL injury risk before it is ever torn, preferably using some form of imaging.

3.1.2 Tissue fatigue as a mechanism for non-contact mode ACL failures

Recent cadaveric studies suggest that under repetitive sub-maximal loading the ACL can accumulate tissue fatigue damage, and this has been hypothesized to be the mechanism underlying the ACL injuries that occur in 75% of injuries when athletes are performing routine non-contact maneuvers.[6–9] Three dimensional impulsive repetitive loading of cadaveric knees demonstrated that the number of cycles to ligament failure was influenced by the magnitude of the applied load, that failure could occur within 100 sub-maximal loading cycles, and that the location of the ligament failure matched that seen in the clinic.[7,8]. However, the ligament microdamage generated by repetitive loading is presently more challenging to detect than a severe, acute, contact injury due to the limited spatial resolution of conventional imaging methods like magnetic resonance imaging or ultrasound. Nonetheless, characterization of the extent of any microdamage would allow a better understanding of the risk of impending injury and could even potentially serve as a diagnostic marker. Research shows microdamage signatures to encompass multi-scalar structural and chemical damage due to collagen denaturation,[9–11] and compromise the tissue's viscoelastic properties.[12] An additional study has highlighted the neurological disturbance and motor dysfunction observed in the knee of a sub-critically injured mouse that is similar to that of a critically injured mouse, indicating a potential predisposition of the sub-critically injured mouse to eventually sustain an ACL rupture.[13]

3.1.3 Shortcomings of current diagnostic methods for ACL fatigue damage

A routine evaluation of ACL tissue status aimed at detecting microdamage would have to be financially viable for patients as well as simple and safe to operate. Widely used diagnostic methods for ACL injury include, the anterior drawer, Lachman or pivot-shift test, magnetic resonance imaging (MRI) and micro-computed tomography (μCT).[14] Of the three physical examination techniques, the Lachman test is the best at determining ACL injury status

based on predictive value statistics.[15,16] However, predictive values can be highly influenced by the incidence of the condition in the study population.[15,17] In addition, the physical diagnosis only informs, if present, a compromise in the mechanics of the ACL in a binary format – failed or not failed. Even a partial ACL tear would often need a combination of physical, imaging and if necessary, arthroscopic examinations to determine it.[18] Thus, diagnosis of microdamage would likely not be possible with the current physical examinations options. Even though MRI is a common imaging examination used to diagnose ACL injury, its expense and limited spatial resolution pose challenges for routine clinical use, and it is not yet suitable as a tool to detect molecular to micro-scale damage signatures. Furthermore, the ACL fatigue signature has still not yet been identified using MRI. A recent study did report changes in the T2* signal on MRI images of the ACL in alpine ski racers, suspecting a decreased stressed tolerance and increased susceptibility for fatigue tears.[19] The T2* values reflect inherent tissue properties related to tissue composition such as collagen fiber and water content.[19] μCT can provide high resolution images of bone and soft tissues when enhanced with contrast agents; however, the radiation and contrast agents would be harmful to patients as a part of a routine diagnosis. Similarly, arthroscopic procedures are unable to detect molecular to microscale chemical and structural anomalies.

Recent advances in fiber-optics and confocal endomicroscopy have led to the detection of pathological signatures *in vivo* through the development of miniaturized confocal endoscopes with high spatial resolution that can access deeper parts of the body.[20] For example, endomicroscopic examination of the villi of small intestine detected abnormalities associated with celiac disease not seen in conventional histology.[21] Additionally, examination of the mucosa of GI tracts with administration of exogenous contrast agents have been performed to aid in *in vivo* cellular morphology imaging to identify gastroesophageal cancer in its early stages.[20,22] However, exogenous contrast agents *in vivo* may not be favourable due to potential

immune response, cost, and challenging administration for the case of ACLs. Collagen autofluorescence has been exploited for monitoring pathological conditions such as wound healing of scar tissues.[23] Endogenous fluorophores such as phenylalanine, tyrosine, pyridinoline cross-links, and the advanced glycation end products have been associated with autofluorescence of collagen.[24–27] Ligament autofluorescence, however, depends not only on the endogenous fluorophores but their architecture due to its effect on optical properties of tissue such as absorption or scattering of light.[28] Pathological disorders can alter tissue architecture and biochemical composition, which can in turn induce changes in autofluorescence.[29] For example, Hansch et al. demonstrated that changes in autofluorescence signal intensities in arthritic mouse knees depended on the stage of inflammation associated with changes in collagen/elastin structures and NAD(P)H from cell metabolism.[30] Furthermore, type 1 collagen's high degree of order and non-centrosymmetric structure lends itself to second harmonic generation (SHG) imaging. Using SHG and autofluorescence lifetime measurement of skin from Ehlers-Danlos syndrome patients, an increase of the SHG signal and a decrease of the autofluorescence lifetime has been detected as a result of defects in the mature collagen crosslinks.[26] The combination of CLE and the intrinsic fluorescence of collagen offer opportunities to expand its application toward diagnosis of ACL.

Previously, we have demonstrated that repetitive mechanical loading of adult, human cadaveric knees developed accumulated damage to collagen fibrils and fibers at the femoral enthesis, suggesting that some non-contact ACL injuries may occur due to an exacerbation of pre-existing hierarchical tissue damage.[9] In the present study, we employed confocal multiphoton microscopy to measure changes in the second harmonic and autofluorescence signal intensity of control and mechanically loaded ACLs. The autofluorescence (AF) intensity was tracked in 10 knees prior to loading, and 7 knees during 3-4*bodyweight jump landing loading for up to 100 cycles, and post failure which was defined as anterior tibial translation >

3mm, if it occurred prior to completing the 100 cycles. We tested the hypothesis that collagen autofluorescence, via a confocal laser endoscopic microscope, can be used to quantify ACL fatigue damage. We also tested the hypothesis that as damage progresses in relation to the number of sub-maximal loading cycles, the collagen autofluorescence would be greatest near the femoral enthesis; the region that not only has been theoretically predicted to be at highest risk[31], but is also the most common site of ACL injury in patients (for review, Wojtys et al. 2016).

3.2 Methods

3.2.1 Preparation of cadaveric knees and paired knees mechanical loading

Table 3.1 *Demographic information for the 10 knees: 3 paired (P) knees, of which one of each pair would serve as an untested control, and the 4 single (S) knees used for repeated measures experiments.*

Specimen	Sex, tested limb	Age (yr)	Height (cm)	Weight (kgs)	BMI (kg/m^2)	Weight category	PTS (deg)	# loading cycles
P1	M, L	34	185	73	21.2	Normal	5.15	100
P2	M, L	36	175	82	29.4	Overweight	5.94	100
P3*	F, R	31	-	68	-	-	2.02	100
S1	F, L	38	160	58	23	Normal	0.94	5
S2	F, R	30	172	82	27.5	Overweight	9.07	9
S3	F, L	38	165	48	17.6	Underweight	9.11	50
S4	F, R	26	167	61	21.6	Normal	4.78	100

For this study, four paired knees and four single knees were acquired from the University of Michigan Anatomic Donations Program and Gift of Life Michigan (Table 3.1). We followed the same procedures for preparing and mounting the adult human knees for mechanical testing as published previously.[9] The proximal femoral and distal tibial were cut to a length of 20 cm from the knee joint line and mounted in cylindrical grips using polymethylmethacrylate. One of each pair of knees was randomly selected for mechanical testing, while the other was used as an untested control. Each leg underwent preloading cycles

prior to the jump landing loading cycles. The preloading cycles are performed to calibrate the load cell to apply a 4 times-bodyweight impulsive load to the quadriceps muscle which are detected by a sensor. This is performed without the internal tibial torque to minimize ACL damage. The loading cycles consist of simultaneous impulsive flexion and internal rotation moments combined with 3-4x bodyweight compression of the knee joint peaking in ~70 ms[9]. The selected knee for mechanical testing was subjected to 100 loading trials or until ACL failure (> 3 mm anterior tibial translation).

3.2.2 Preparation of ACL explants of paired knee cadavers

After mechanical testing was completed the methods for extracting each ACL from its knee complete with its bony origin and insertion, preserving and embedding the explant, and Kawamoto cryosectioning were performed as described previously.[9]

3.2.3 Preparation for Confocal Laser Endomicroscopy and single knee mechanical loading

With the knee in flexion, two small incisions were cut with a scalpel through the skin, fascia and joint capsule, one medial and one lateral to the patellar tendon for each knee. Each port formed a tunnel through which the arthroscopy (AR) and the CLE probes could be introduced intraarticularly to visualize the joint internally and conduct the autofluorescence imaging of the ACL. The 4 mm diameter AR probe (Model 1288 HD with an X8000 Light Source, Stryker Inc., Kalamazoo, MI) was used during isotonic saline irrigation with a DePuy Duo Fluid Management System (DePuy Mitek, Inc., Raynham, MA) for guiding the 4 mm diameter CLE probe (Optiscan, Model 'ViewnVivo2', Optiscan Imaging Ltd, Mulgrave, VIC, Australia) to its region of interest on the ACL. A custom probe holder was used to stabilize the probe during

Figure 3.1 *Custom probe holder attached to bars of mechanical testing instrument*

Figure 3.2 *Images of the apparati used for impulsive fatigue loading of ACL while confocal laser endomicroscopy (CLE) was used to detect changes in the ACL before, during and after the loading regimen. Changes in fluorescence were monitored approximately every 33 cycles up to 100 cycles. a) Mechanical loading device with inverted cadaver leg at an initial angle of 15º flexion generates material fatigue in the ACL after repeated pivot jump landing maneuvers. b) CLE set up with the base unit, display monitor and handheld probe attached to the base unit via a flexible waterproof cable. c) Dual probe insertion (arthroscope (AR) and CLE) through two ports located medial and lateral to the patellar tendon in order to access the proximal and distal ACL for internal joint visualization and navigation with AR and autofluorescence imaging with the CLE.*

Table 3.2 *Summary of the repeated measures experimental design for each single (S) knee.*

Specimen	Mechanical loading and CLE imaging sequence
S1	Image → 5 preloading cycles → tibial avulsion → dissect → image (END)
S2	Image → 5 preloading cycles → 4 cycles (> 3mm translation) → image (END)
S3	Image → 5 preloading cycles → image → 33 cycles → image → 45 cycles → image (END)
S4	Image → 5 preloading cycles → 33 cycles → image → 66 cycles → image → 100 cycles → image(END)

Table 3.3 *Peak cumulative kinematic measures for each knee. Internal tibial rotation (ITR) and anterior tibial translation (ATT) recorded after the last mechanical loading cycle corresponding to sample*

Specimen	ITR (deg)	ATT (mm)	Peak impact force (N)
P1	0.23	0.13	N/A
P2	5.28	6.88	N/A
P3	9.49	8.47	N/A
S1*	-	-	2045
S2	1.17	3.03	3376
S3	1.93	1.14	1837
S4	0.79	0.11	2868

image acquisition. The holder had a long flexible arm with a steel sleeve to encase the CLE probe (Figure 3.1). The ports were strategically positioned to enable the CLE probe to be navigated by the surgeon to access the most proximal, the midsubstance as well as the distal

regions of the ACL while maintaining the probe normal to the surface of the ACL tissue to enable optimal image acquisition. CLE and AR images were then obtained before mechanical testing of the knee from the proximal and distal ACL regions. The development of any material fatigue damage in those regions was then observed by capturing autofluorescence images with CLE after 33 impulsive mechanical loading cycles of the knee, until either ACL failure was observed or 100 loading cycles was reached (Figure 3.2, Table 3.2 for details). The cumulative internal tibial rotation (ITR) and anterior tibial translation (ATT) are reported for all specimens (Table 3.3).

3.2.4 Second harmonic generation and autofluorescence imaging with confocal microscopy[k]

The procedures for SHG imaging were carried out as previously published.[9] Autofluorescence images were collected using a Leica SP8 confocal microscope using a white light laser source (20% laser power, 50% gain) tuned to 488 nm. The photomultiplier detector was set at 520 – 560 nm for autofluorescence detection. Autofluorescence images were captured over the same regions as measured for SHG imaging.

3.2.5 Autofluorescence imaging with Confocal Laser Endomicroscopy[l]

The autofluorescence images were collected with ViewnVivo2 a CLE probe with 4 mm diameter. The light source was a 488 nm visible light laser (500 µW, 94% brightness, 2400 gain, 1x zoom 475 x 475 µm field of view, 1024 x 1024 pixels, lateral resolution: 0.55 µm, axial resolution: 5.1 µm). The detection filter was set to LP515 (longpass 515nm). CLE offers optical sectioning in a z-stack image sequence mode. This feature was used to capture up to 50 µm of autofluorescence into the tissue using a 5 µm step size. Two to five locations were

[k] SHG and AF imaging with confocal microscopy performed by Jinhee Kim
[l] AF imaging with confocal laser endomicroscopy performed by Jinhee Kim

sampled from each of the three regions of the ACL: proximal, midsubstance and distal. The selection of the three regions was made by an experienced orthopaedic knee surgeon (E.W.).

3.2.6 SHG and Autofluorescence image analysis[m]

The signal intensity of SHG and AF images were quantified using a protocol that has been published previously.[9] In brief, the intensity values were quantified with Fiji (National Institutes of Health). For each image, the mean intensity of a 100 x 100 μm^2 area was measured for all mechanically tested and control knees (one of each pair of P1-3). Then the intensity values from the ACLs of tested knees were reported as a percentage of that of their contralateral control, set as the baseline intensity.

3.2.7 CLE autofluorescence image analysis[n]

3.2.7.1 Signal intensity quantification

Autofluorescence intensity values will be reported separately for the three regions of the ACL (e.g., proximal, midsubstance and distal) as a cumulative percentage change as a function of mechanical loading cycles. The brightness of the z-stack autofluorescence images were quantified with Fiji (National Institutes of Health). From each z-stack, the image with the highest brightness was selected be averaged with two to five other images from the same region at the same point in loading cycle to represent the average autofluorescence intensity at the specific point of loading cycle. The brightest image typically had the best resolution of the fiber structures. Then a cumulative percentage change was calculated in reference to the autofluorescence intensity of ACL prior to mechanical testing, set as the baseline intensity.

[m] SHG and AF image analysis performed by Jinhee Kim
[n] CLE AF image analysis performed by Jinhee Kim

3.2.7.2 Collagen fiber structure analysis

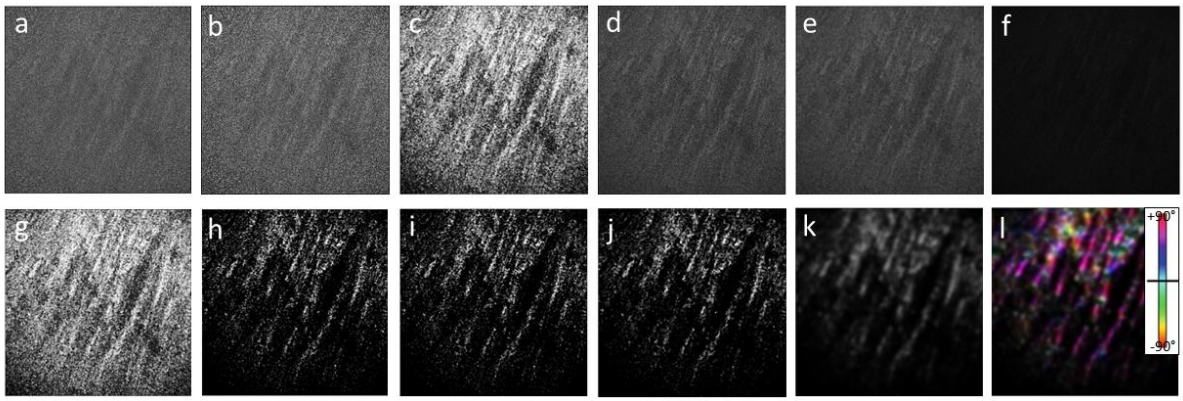

Figure 3.3 *Imaging processing steps of CLE AF images with Fiji for fiber orientation distribution and anisotropy analysis. A) Raw image b) Auto brightness and contrast c) Gamma adjustment gamma = 1.3 d) Noise reduction with Despeckle e) Median filter pixel = 4 f) Mexican hat filter r = 1, separable selected g) Enhance contrast. Saturated pixels = 1.0%, equalize histogram selected h) Gamma adjustment gamma = 4 – 5, i) Noise reduction with Despeckle j) Median filter pixel = 4 – 8 k) Gaussian blur filter 6 – 10 l) OrientationJ Analysis results of color-coded map of fiber orientations.*

Quantification of changes in collagen fiber orientation distributions as a result of fatigue loading was analysed using the Fiji plugin OrientationJ (National Institutes of Health). OrientationJ evaluates local orientation and anisotropic properties of the image.[32] Prior to running the analysis, raw images were processed to enhance brightness and contrast for optimal fiber detection with the software. A series of brightness and contrast enhancement, edge detection, noise reduction, and unsharpening filters were used to prepare the images to be analysed (Figure 3.3). The output from OrientationJ analysis, distribution and dominant direction were utilized, specifically the histogram of orientation angles, coherency parameter, and hue-saturation-brightness (HSB) color-coded map of fiber orientations. The changes in the distribution of orientation in the histogram was scrutinized rather than the absolute orientation values. A coherency parameter was used to quantify the degree of anisotropy in fiber orientations with values ranging between 0 and 1, with 1 indicating highly oriented structures and 0 indicating anisotropic areas.[32] For these analyses, a region of 10 pixels was designated as the local window for cubic spline interpolation. Representative figures of distribution of

fiber orientation angles in addition to coherency parameters summarizing comparison of all control and fatigue loaded samples are reported in Results.

3.3 Results

3.3.1 Second harmonic generation and autofluorescence imaging for paired knees

Representative images of SHG and AF comparing a paired control and mechanically loaded ACL are reported in Figure 3.4. The SHG and AF signal intensity values of tested knees are reported as a percentage of each contralateral control, set as the baseline intensity. Quantification of the paired knee specimens, P1 – P3, revealed the SHG signal intensity of mechanically loaded ACL fibers was reduced whereas the AF signal intensity increased compared to its contralateral untested control. An evaluation of tissue structure by quantification of the distribution of collagen fibers' local orientation and anisotropy revealed the control ACL to possess highly uniform orientation of fibers, as shown in overall green-hued color-coded map (Figure 3.5c) with the distribution of orientation centered around -38°

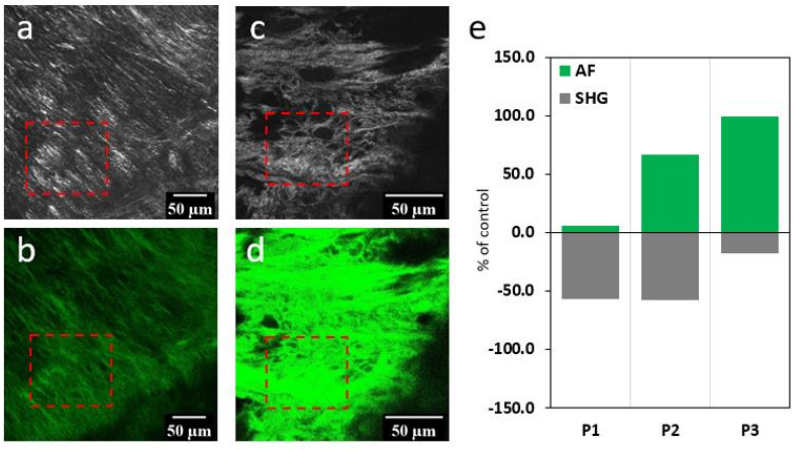

Figure 3.4 *Representative image of second harmonic generation (SHG) and autofluorescence (AF) images from a paired control (a, b) and mechanically loaded ACL (c, d). Red dashed boxes (100 x 100 µm2) indicate regions of interest (ROI) used to quantify SHG and AF intensity. The results of all paired knee samples P1 – P3 are shown in (e) which are reported as the intensity of mechanically loaded ACL as a percentage of contralateral control ACL. All mechanically tested knees displayed a reduced SHG signal intensity compared to its contralateral control, whereas the AF signal intensity was enhanced.*

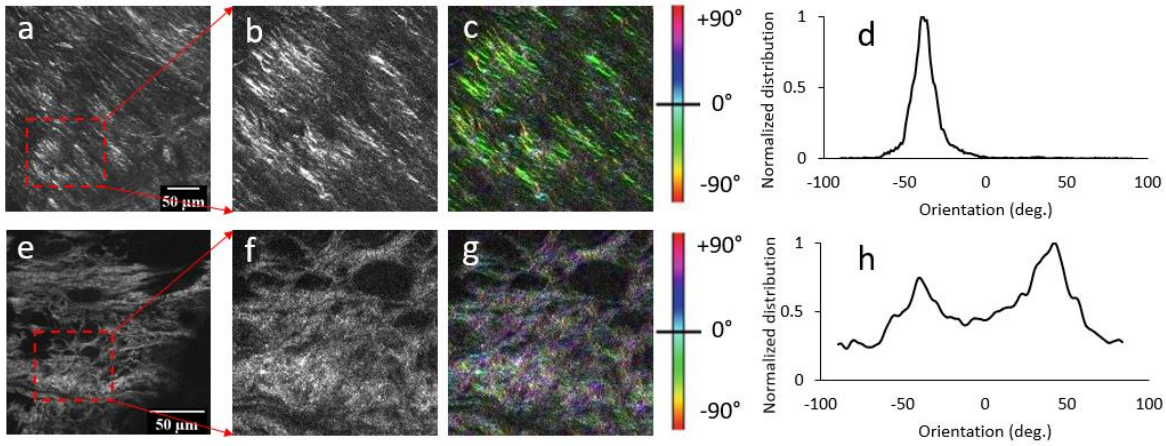

Figure 3.5 *Representative local fiber orientation distribution analysis results of SHG images from control (first row) and mechanically loaded ACLs (second row). a) SHG image of a control ACL with the cropped ROI shown in b. c) Color-coded map of orientation of fibers display a dominant green hue. d) Normalized distribution of orientation shows a narrow, single peak around -38° with FWHM of 15°. e) SHG image of a mechanically loaded ACL with the cropped ROI shown in f. g) Color-coded map of orientation of fibers does not display dominant hue. h) Normalized distribution of orientation displays a dispersed bimodal distribution with a FWHM of 120° .*

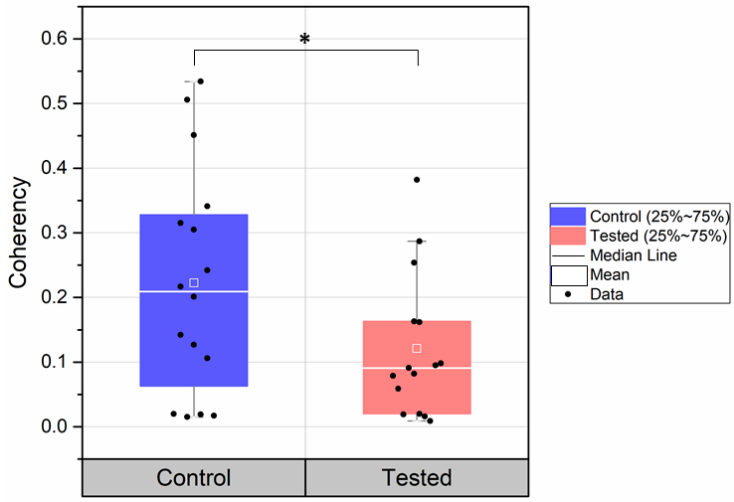

Figure 3.6 *Coherency analysis of control and fatigue loaded ACL SHG images showed a statistically significant loss of coherency in the loaded ACLs (coherency coefficient 0.10. ± 0.06) compared to a control ACL (coherency coefficient 0.26 ± 0.09). Therefore, control samples displayed a stronger coherent orientation of local fibers while tested samples display reduced preferential orientation of fibers.*

with a full width half max (FWMH) of 15° (Figure 3.5d). In contrast, the analysis of mechanically loaded ACL displayed no dominant hue in the HSB color-coded map (Figure 3.5g) due to a dispersed bimodal distribution of orientation with FWHM spanning nearly 120° (Figure 3.5h). (The orientation angles are arbitrary therefore we believe the distribution described by FWHM is the most meaningful parameter to quantify the changes the distribution of fiber orientations.) An analysis of coherency coefficients of all control versus mechanically loaded ACL fibers showed a statistically significant ($p < .05$) loss of coherency in the

mechanically loaded ACLs (coherency coefficient 0.10. ± 0.06) compared to each paired control ACL (coherency coefficient 0.26 ± 0.09) (Figure 3.6). Chen et al. demonstrated in his cadaver knee loading study, that repetitive mechanical loading of the knee leads to a disruption of collagen triple helix by unravelling of the molecule which was evidenced by the novel spectroscopic peak 1740 cm^{-1} and the CHP-TAMRA binding experiment.[9]

3.3.2 Confocal laser endomicroscopy autofluorescence imaging for single knees as a function of mechanical loading cycles

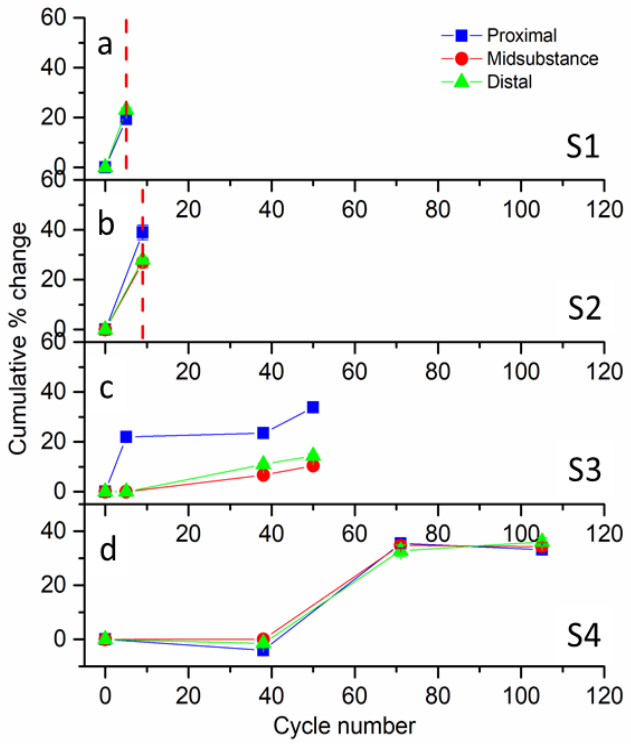

Figure 3.7 *Cumulative % change in autofluorescence intensity for proximal, midsubstance and distal region of ACL as a function of mechanical loading cycles. The failed specimen (a, b) displayed a sharp increase in autofluorescence while the non-failed specimen (c, d) displayed only a gradual increase. Red dashed line indicates the cycle of failure during loading.*

Evolution of fatigue damage was observed in the repeated measures experiments (that were conducted with the S specimens) via autofluorescence (AF) imaging and confocal laser endomicroscopy (CLE) as a function of mechanical loading. We also compared the AF signal changes from the proximal, midsubstance and distal regions of the ACL. Four single knee loading experiments were performed in which two knees failed prior to completing 100 loading cycles and the other two did not (Table 3.2). All four specimens showed increased autofluorescence intensity with progressive loading cycles. Specimen S1 underwent a tibial avulsion after 5 preloading cycles, leading to a greater increase in autofluorescence signal of 23% in the distal region fibers of the ACL (Figure 3.7a) compared to the proximal region. The midsubstance region was unable to be imaged due to tissue damage. Specimen S2

reached failure after 5 preloading and 4 loading cycles, leading to the largest autofluorescence increase of 40% in the proximal region compared to similar changes sustained between midsubstance and distal regions with 27% and 28% respectively (Figure 3.7b). Specimen S3 possessed a thick synovium sheath which hindered the AF imaging capability of ACL fibers underneath. Therefore, the synovium sheath around the proximal region was gently removed using a swab and the midsubstance and distal regions were cleared after 5 preloading cycles,

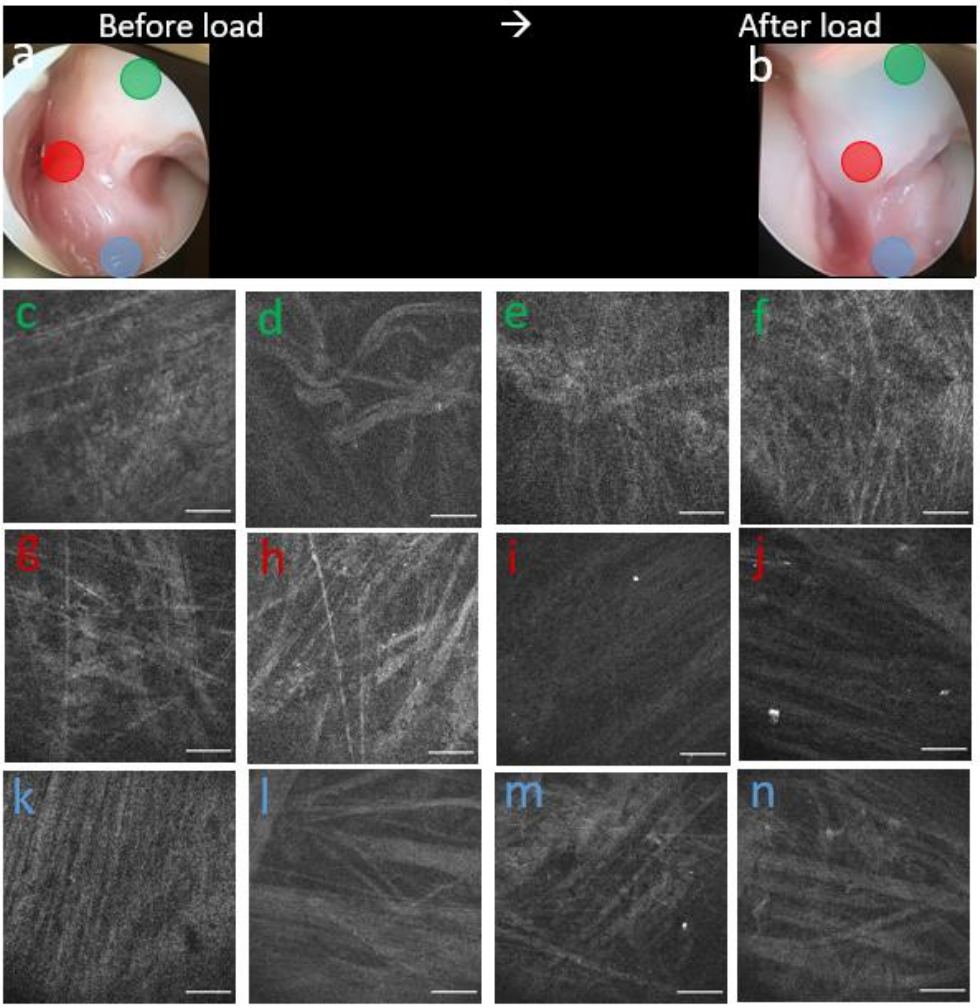

Figure 3.8 *Sample S3. Arthroscopy and CLE image of ACL with thick synovium a) before and b) after 50 total loading cycles. CLE probe placement for AF image capture at distal, midsubstance and proximal regions of ACL are marked by green, red and blue circles respectively. CLE images of distal ACL fibers c) before d) after 5 pre-loading cycles e) additional 33 cycles up to f) 45 cycles. CLE images of midsubstance ACL fibers g) before h) after 5 pre-loading cycles i) additional 33 cycles up to j) 45 cycles. CLE images of proximal ACL fibers k) before l) after 5 pre-loading cycles m) additional 33 cycles up to n) 45 cycles. Scalebar 100µm.*

which disintegrated the sheath. The synovial sheath is easily recognized optically by an opaque white layer over the ACL with the AR probe whereas the CLE AF imaging portrays thin, intertwined fibers over thicker, unidirectionally aligned fibers (Figure 3.8). For this specimen,

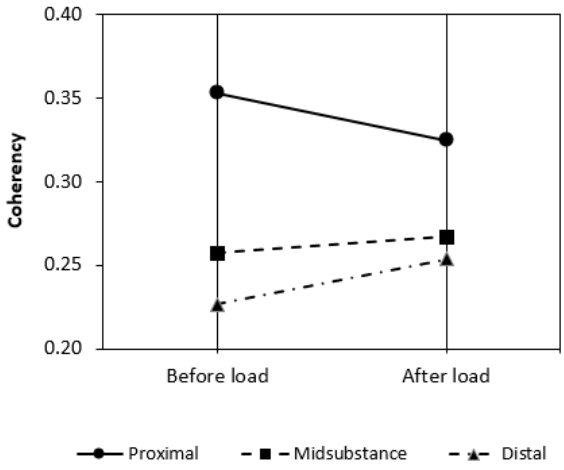

Figure 3.9 *Coherency coefficient analysis of AF image of proximal, midsubstance and distal region of ACL before and after loading shows the proximal region of fibers underwent a loss of preferential alignment or increase in anisotropy relative to the midsubstance and distal region fibers, which gain fiber alignment or decrease in anisotropy. Standard deviation values are approximately 30 – 40% of mean value (not displayed).*

the proximal region of ACL fibers, where the synovium sheath had been cleared, displayed the largest change in AF intensity of 34%. The midsubstance and distal regions with remaining sheath sustained changes of 10% and 14%, respectively (Figure 3.7c). Specimen S4 sustained the largest number of loading cycles of all single knee specimens. There was little to no change in autofluorescence in all three regions of the ACL during the first 38 cycles. However, during the 34th to the 66th loading cycle, there was an AF increase of approximately 35% for all three regions of the ACL (Figure 3.7d). This value proved to be a plateau and no further increase in autofluorescence was observed over the last 34 cycles. On average, the knees in which the ACL ruptured (S1, S2) had a 4% higher percentage change in AF signal intensity per loading cycle compared to the knees in which the ACL did not rupture (S3, S4); the latter exhibited an order of magnitude lower change in autofluorescence of 0.4% increase per cycle. Specimens S2 and S3 both exhibited 10 – 20% higher AF intensity change in the proximal region compared to the other regions of the ACL. The results of changes in the fiber orientation distribution and isotropy indicate that the proximal region of fibers underwent a loss of preferential alignment, or an increase in anisotropy, relative to the midsubstance and distal region fibers, which gained fiber alignment or a decrease in anisotropy (Figure 3.9). The difference in behavior of fiber organization with application of load reflects the gradient of loading force each region experiences. The loss of

coherency in the proximal region fibers are demonstrated by changes in the distribution of fiber orientation in Figure 3.10. (See Appendix for CLE images of S1, S2, S4)

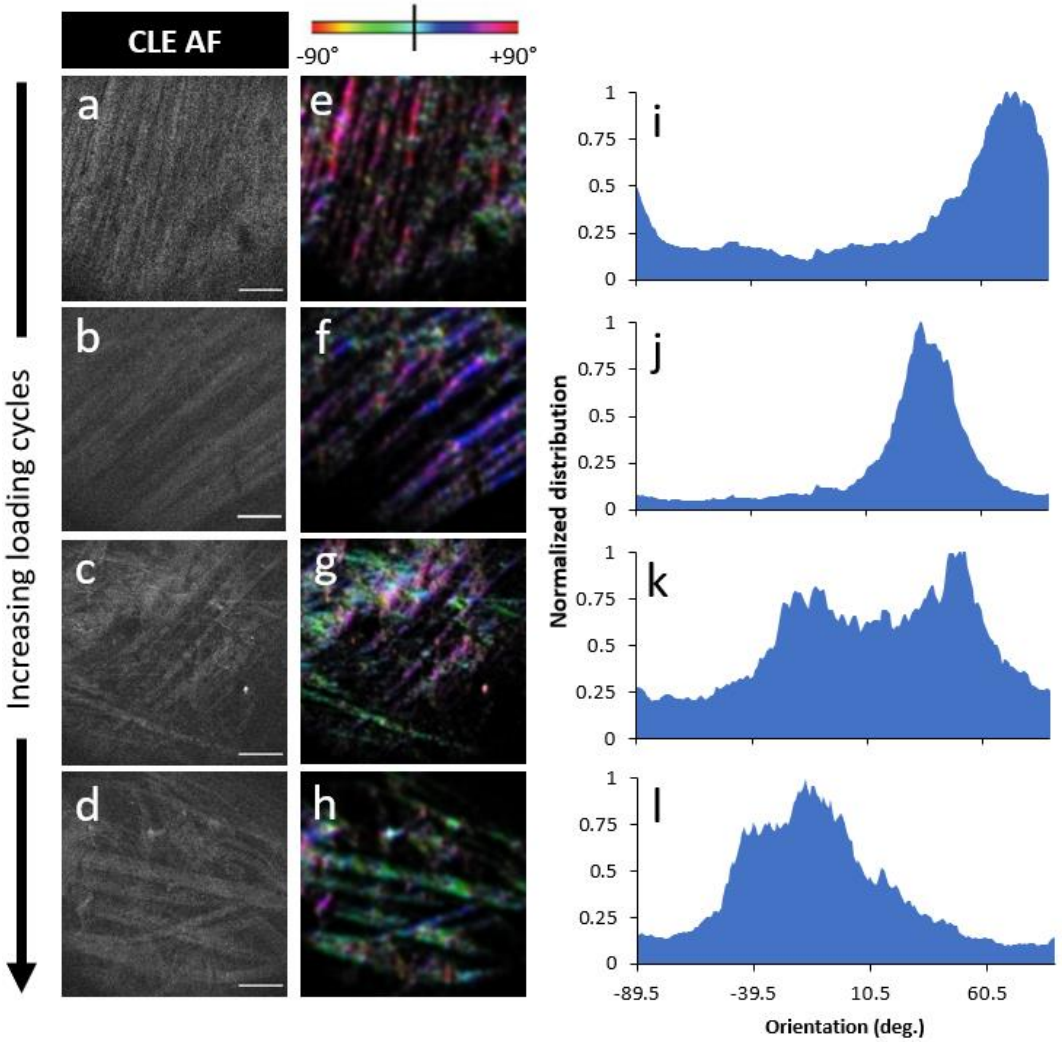

Figure 3.10 *Proximal region collagen fibers imaged with CLE display increased distribution of fiber orientation angles with increasing loading cycles. a – d) CLE AF images of proximal region fibers before load, post 5 preload, 33 cycles and 50 cycles. e-h) color-coded AF images of fiber orientations. i-l) normalized distribution of fiber angles*

3.4 Discussion

In this work, we evaluated the effect of fatigue damage between an internal control and contralateral ACL that has been mechanically tested by SHG and AF imaging with benchtop confocal microscopy. Subsequently, we utilized the intrinsic signal of collagen autofluorescence to measure the development of fatigue damage in a single knee before, during and after loading with a CLE. We confirmed the hypothesis that mechanical loading generated

fatigue damage in the tested knee seen by increased SHG signal intensity and decreased AF intensity in comparison to the contralateral control (Figure 3.4). A broad distribution of collagen fibers' orientation angles (Figure 3.5) and a statistically significant loss of coherency (alignment) in the mechanically loaded ACL (Figure 3.6) further validated the SHG and AF results. We also confirmed damage progression in relation to the number of mechanical loading cycles with the CLE AF signal intensity. Interestingly, the changes in AF varied for all four single leg cadavers, which may be attributed to age or physiological parameters such as BMI and PTS (posterior lateral tibial slope).

3.4.1 Mechanism of autofluorescence

Figure 3.4 shows a reduction in SHG signal and an increase in AF intensity for the mechanically loaded knee compared to its internal control. The label-free SHG process is influenced by the hyperpolarizability arising from collagen molecules, which forms the basis of the SHG contrast mechanism.[33] Therefore, the reduction in SHG signal intensity is consistent with the hierarchical structural changes that alter the molecular assembly due to attenuation of mechanical strain from sub-maximal repetitive mechanical loading.[9] Collagen autofluorescence depends not only on the endogenous fluorophores but their architecture due to its effect on optical properties of tissue such as absorption or scattering of light.[28] The disruption of non-centrosymmetric collagen crystallinity and unfolding effects of the collagen molecule can increase the separation between the endogenous fluorophores, reducing the fluorophores' self-quenching behaviour, thus leading to increased autofluorescence. Collagen contains fluorophores such as phenylalanine, tyrosine, pyridinoline cross-links and the advanced glycation end products where about 50% of these fluorophores are located within a cross-link site. [24–26] Cross-links are essential for maintaining tissues mechanical stability. It is possible that the cross-links become compromised as a result of mechanical loading, leading to exposure of the accumulated fluorophores within the cross-links as the molecular unwinding

takes place resulting in an increase in autofluorescence signal. Tyrosine residues in the non-helical telopeptide regions are known to play an important role in collagen self-assembly by providing hydrophobic interactions.[34] Additionally its fluorescence property have been used as a structural probe for collagen. It was shown that upon dissociation of aggregated type 1 collagen by collagenase, an increase in intrinsic fluorescence intensity of type 1 collagen was observed due to the increased in the number of exposed tyrosine residues which were initially wrapped in collagen during aggregation.[24] The unfolding effects of collagen may have increased the distance between the fluorophores with one another thereby reducing fluorescence quenching and thus enhancing the autofluorescence intensity. However, some discrepancies have been found in literature where a thermal denaturation of collage in an acidic solution resulted in a strong fluorescence quenching, and no wavelength shift, indicating that the microenvironment around the tyrosine and phenylalanine residues were not significantly changed.[35] Despite the advantages of a reductionist model of a tissues (a solution based study), extending its results to a complex biomacromolecule such as the ACL femoral enthesis may be limited in elucidating the effects of its heterogeneous local environment. A study investigating fluorescence signal in relation to mechanical properties of perimysium from bovine masseter indicated that the fluorescence spectra related to the most important tensile parameter – the breaking force of tissue.[36] They attributed their results to the chemical constituents (e.g. collagen I/collagen III, elastin, crosslinks), which are important for mechanical strength of tissue.

Reversibility of 1,740 cm^{-1} peak with dehydration and rehydration has been eliminated as the main driver of changes in autofluorescence signal in this study using three techniques as validation. A control ACL was subjected to dehydration by N_2 gas and overnight refrigeration which produced a strong 1740 cm^{-1} peak and exhibited at most 10% increase in AF intensity as measured by CLE (Figure 3.11). The single cadaver knees exhibited 20 – 40 % increase in

AF as a function of mechanical loading cycles as measured by CLE. The difference in the magnitude of change between the two methods of 1,740 cm^{-1} production leads us to believe the changes in AF are not driven by dehydration of tissue.

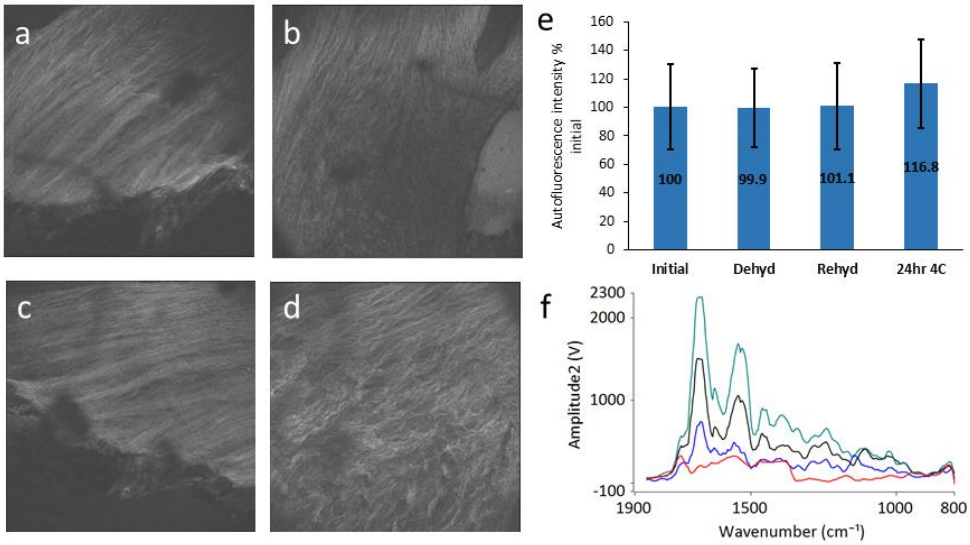

Figure 3.11 *Autofluorescence images of ACL in the initial, dehydrated, rehydrated and stored in fridge state with nanoIR spectrum. Autofluorescence images of ACL in the a) initial state b) dehydrated with N_2 gas for 8 minutes c) rehydrated with water d) stored in 4C fridge for 24hours shows that the e) autofluorescence remains steady from steps a – c however, increases 10% after preservation in the fridge for 24 hours. f) nanoIR spectrum parallels the lack of effect of dehydration seen by a steady 1672cm^{-1}/1740cm^{-1}ratio until the tissue is kept in the fridge which completely reduces the 1672cm^{-1} signal, remaining only the 1740cm^{-1} peak (red spectrum).*

3.4.2 Trend of autofluorescence as a function of loading

Figure 3.7 shows that percent change in autofluorescence alone cannot distinguish the specimens with failed ACL's from non-failure cases. In other words, the percent change cannot distinguish simply an accumulation of fatigue or the point of failure. However, there are variations in trends that may illustrate the differences between the failed versus non-failure cases during mechanical loading.

Failed specimens S1, S2 (Figure 3.7a,b) exhibited on average a larger change of autofluorescence intensity per loading cycle of approximately 4% per cycle compared to non-failed specimens S3, S4 (Figure 3.7 c,d), which exhibited an order of magnitude less 0.4% per cycle. However, the actual distribution per cycle in the failed specimens S1, S2 are unknown

due to the lack of AF measurements between the initial and final point of mechanical loading sequence. On the other hand, specimen S3 and S4 reveal a non-linear change of AF measurements from the initial state and a fatigued state of the ligament prior to failure. This non-linear change postulates that a large increase in AF may occur in a final few cycles immediately prior to or at failure, representing a greater plastic deformation immediately prior to ligament failure. The greater the change of AF signal intensity can reflect a larger perturbation to the structural integrity of tissue.

Furthermore, a larger AF signal intensity change in the proximal region relative to the midsubstance and distal regions may signal risk of failure. The enthesis is where the ligament meets the bone, a dynamic part of our body distributing loads applied to them to execute movement.[37] Clinically, most ruptures of the native ACL and graft ACL occur near the femoral enthesis.[38,39] In addition, a 3D finite element model simulation based on MRI of the ACL shows the largest shear strain occurs at the femoral enthesis.[40] The failed specimen S1 does not agree with this trend due to tibial avulsion. Curiously, the non-failed specimen S3 displays a 10% larger AF change in proximal region compared to other regions of the ACL. Physiological parameters such as BMI and knee morphological parameter such as PTS (posterior tibial slope) [41] may contribute to the AF trends. A higher chance of ACL tear was associated with BMI in the overweight category combined with a posterior lateral tibial slope (PTS) due to production of larger shear force from a larger axial compressive force which increased the degree of internal tibial rotation.[41] Despite the removal of most body mass, each cadaver leg was subjected to three – to – four times original bodyweight of the individual during mechanical loading, which was calibrated by the number of weighted plates and the distance dropped onto the cadaver. The loading force was monitored by the force sensor on the quadricep muscle. Therefore, the loading experiment simulates the axial compressive force exerted as if the individual would be performing a pivot or jump landing maneuver. Failed specimen S2

possessed both risk factors of high BMI and steep PTS of 9.07° which was nearly double the average PTS of non-failed ACL in Bojicic et al.'s work (5.4°). Specimen S3 fell in the underweight category based on her BMI however, S3 possessed a steep PTS of 9.11° which may have contributed to larger shear force at the femoral enthesis. While it is not covered in the scope of this study, the response of cadavers to the mechanical load may also be attributed to the composition of the tissue, which may have been influenced by the loading patterns based on the physiological parameters of the individuals such as BMI and PTS. In addition, the thick synovium sheath for specimen S3 with a steep tibial slope of 9.11° could be the result of body's response to stress to protect the ACL from the recurring large shear force since the synovium may shield cyclic forces for repair.[42]

Age may have affected our results. Figure 3.12 reports the change in AF signal intensity as an average of raw values, which reveals the variation in baseline of the AF intensity of each specimen prior to mechanical loading. The order of specimens from oldest to youngest parallels the order of specimens with the highest baseline AF intensity. The different states of collagen crosslinks resulting from the maturation process[26] may explain the variation in AF baseline.

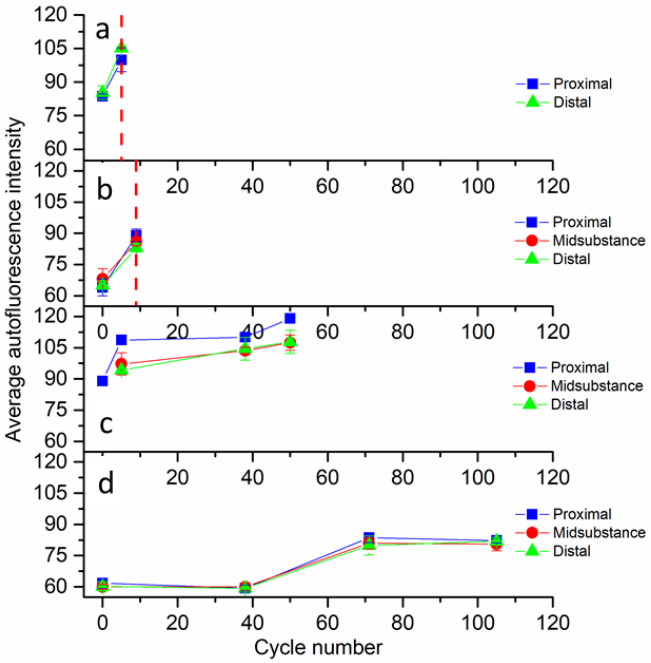

Figure 3.12 *Average change in autofluorescence intensity for proximal, midsubstance and distal region of ACL as a function of mechanical loading cycles. Red dashed lines indicate cycle of failure during loading. Raw average intensity values reveal varying baseline intensities across the specimen. The order of oldest to youngest specimen (a →c →b →d) is equivalent to order of highest to lowest baseline AF intensity (a →c →b →d).*

3.4.3 Diagnostic potential of CLE

This study demonstrates the potential of the CLE to evaluate the fatigue damage development *in vivo* at the molecular level of the collagen matrix of the ACL inside the knee capsule by direct measurements of collagen autofluorescence signals. This is supported by the miniaturised CLE probe with sub-micron lateral resolution imaging and video capture capability, optical sectioning, and adjustable power levels of an 488 nm excitation laser. The probe was able to reach the ACL inside the knee capsule and to capture high-resolution images without the need for contrast agents. The assessment of fatigue damage on ACL without administration of contrast agents in this study reflects the real-time scenario in an operating room, where surgeons are under tight time constraints and minimization of any toxicity is preferred. The traditional technique of ACL injury diagnosis, MRI, is used for static examinations which only presently inform on the status of the macroscopic structures of the ACL. However, the low spatial resolution and high cost of MRIs limit its use as a routine diagnostic tool.

3.4.4 Challenges

Detection of robust differences from an endogenous contrast mechanism may be challenging and thus compromise the diagnostic accuracy.[43] We found that robust signal detection can be hindered by poor probe-to-sample contact and any movement during image collection. Therefore, a custom probe holder was built to improve probe stability and sample contact while imaging. Considerable biological heterogeneity was found in the thickness and extent of the synovial sheath covering the ACL and this presented an unforeseen challenge in detecting autofluorescence signals from the collagen fibers of the ACL. ACLs with thick synovial sheath limited the detection of autofluorescence signals from the collagen fibers from the ACL under the sheath, while ACLs with little to no synovium sheath displayed higher

autofluorescence signal intensity. Another concern is the invasive nature of endoscopic examination of ACL which can limit its appeal due to the potential negative consequences of perturbing adjacent structures. Instead of a visible light excitation laser source, an ultrasound source might have potential as a non-invasive diagnosis strategy in the future. One limitation in this study is the small number of cadaver knees examined. A larger sample set would provide a more comprehensive view of the change in autofluorescence signal trends as a function of fatigue damage accumulation. In addition, it would be valuable to confirm in a larger sample set whether a larger autofluorescence signal intensity change at the proximal region of the ACL compared to midsubstance and distal regions indicate higher fatigue damage concentration at the femoral enthesis, thereby serving as a pre-injury marker. Finally, CLE can only image the surface layers of the ACL so fatigue damage can in deeper layers is unable to be evaluated. This would be less relevant if it was found that the risk of fatigue damage was greatest at the surface of the ACL particularly in the most distal part of its femoral enthesis. However, the physical presence of the lateral femoral condyle prevents an endoscopic probe from visualizing those fibers without it being a side probe.

3.5 Conclusions

1) The paired knee loading study exhibited a reduction in SHG and an increase in AF for the tested knee compared to its contralateral control. The changes in distribution of fiber orientation and increased anisotropy support multi-scalar tissue damage reported in our previous study.

2) The AF from CLE was successfully able to capture changes in autofluorescence as a result of mechanical loading. While the changes in AF intensity long were not sufficient to

distinguish failed vs non-failed ACL's, trends such as higher AF change in the proximal ACL fibers compared to midsubstance and distal regions may signal susceptibility for ACL failure.

3) Increased anisotropy of fiber orientation in the proximal region and the changes in distribution of fiber orientation support the AF trend.

3.6 Acknowledgements

The authors would like to thank Optiscan for the loan of the Five2 (Viewnvivo) system for part of this study, and for making the international collaboration possible. We would also like to thank (name individuals who helped) for their time. This work was supported by U.S. Public Health Service grant R01 AR054821.

3.7 References

1. Marieswaran M, Jain I, Garg B, Sharma V, Kalyanasundaram D. A review on biomechanics of anterior cruciate ligament and materials for reconstruction. *Appl Bionics Biomech*. 2018;2018. doi:10.1155/2018/4657824
2. Nessler T, Denney L, Sampley J. ACL Injury Prevention: What Does Research Tell Us? *Curr Rev Musculoskelet Med*. Published online 2017. doi:10.1007/s12178-017-9416-5
3. Griffin LY, Albohm MJ, Arendt EA, et al. Understanding and Preventing Noncontact Anterior Cruciate Ligament Injuries A Review of the Hunt Valley II Meeting , January 2005. 2006;34(9):1512-1532. doi:10.1177/0363546506286866
4. Yoshida M, Fujii K. Differences in cellular properties and responses to growth factors between human ACL and MCL cells. *J Orthop Sci*. 1999;4(4):293-298. doi:10.1007/s007760050106
5. Wiggins AJ, Grandhi RK, Schneider DK, Stanfield D, Webster KE, Myer GD. Risk of Secondary Injury in Younger Athletes after Anterior Cruciate Ligament Reconstruction. *Am J Sports Med*. 2016;44(7):1861-1876. doi:10.1177/0363546515621554
6. Boden BP, Dean CS, Feagin JA, Garrett WE. Mechanisms of anterior cruciate ligament injury. *Orthopedics*. Published online 2000. doi:10.3928/0147-7447-20000601-15

7. Lipps DB, Wojtys EM, Ashton-Miller JA. Anterior cruciate ligament fatigue failures in knees subjected to repeated simulated pivot landings. *Am J Sports Med*. 2013;41(5):1058-1066. doi:10.1177/0363546513477836

8. Bates NA, Schilaty ND, Nagelli C V., Krych AJ, Hewett TE. Validation of Noncontact Anterior Cruciate Ligament Tears Produced by a Mechanical Impact Simulator Against the Clinical Presentation of Injury. *Am J Sports Med*. 2018;46(9):2113-2121. doi:10.1177/0363546518776621

9. Chen J, Kim J, Shao W, et al. An Anterior Cruciate Ligament Failure Mechanism. *Am J Sports Med*. 2019;47(9):2067-2076. doi:10.1177/0363546519854450

10. Zitnay JL, Jung GS, Lin AH, et al. Accumulation of collagen molecular unfolding is the mechanism of cyclic fatigue damage and failure in collagenous tissues. *Sci Adv*. 2020;6(35). doi:10.1126/sciadv.aba2795

11. Veres SP, Harrison JM, Lee JM. Mechanically overloading collagen fibrils uncoils collagen molecules, placing them in a stable, denatured state. *Matrix Biol*. 2014;33:54-59. doi:10.1016/j.matbio.2013.07.003

12. Panjabi MM, Moy P, Oxland TR, Cholewicki J. Subfailure injury affects the relaxation behavior of rabbit ACL. *Clin Biomech*. 1999;14(1):24-31. doi:10.1016/S0268-0033(98)00046-1

13. Ishihara S, Blaker C, Miller R, Clarke E, Little C, Malfait A-M. Critical and sub-critical load-induced knee injuries promote long term pain and impaired locomotion in mice. *Osteoarthr Cartil*. 2018;26:S74. doi:10.1016/j.joca.2018.02.157

14. Hung Alex Ng W, Francis Griffith J, Hiu Yee Hung E, et al. Imaging of the anterior cruciate ligament. *World J Orthop*. 2011;2(8):75-84. doi:10.5312/wjo.v2.i8.75

15. J.A. Ostrowski. Accuracy of 3 diagnostic tests for anterior cruciate ligament tears. *J Athl Train*. 2006;41(1):120-121. Accessed January 21, 2021. http://www.ncbi.nlm.nih.gov/pubmed/16619105%0Ahttp://www.ncbi.nlm.nih.gov/pubmed/16619105

16. Huang W, Zhang Y, Yao Z, Ma L. Clinical examination of anterior cruciate ligament rupture: A systematic review and meta-analysis. *Acta Orthop Traumatol Turc*. 2016;50(1):22-31. doi:10.3944/AOTT.2016.14.0283

17. Fritz JM, Wainner RS. Examining diagnostic tests: An evidence-based perspective. *Phys Ther*. 2001;81(9):1546-1564. doi:10.1093/ptj/81.9.1546

18. Tjoumakaris FP, Donegan DJ, Sekiya JK. Partial tears of the anterior cruciate ligament: diagnosis and treatment. *Am J Orthop (Belle Mead NJ)*. 2011;40(2):92-97. doi:10.1016/j.rboe.2015.02.003

19. Csapo R, Juras V, Heinzle B, Trattnig S, Fink C. Compositional MRI of the anterior cruciate ligament of professional alpine ski racers: preliminary report on seasonal changes and load sensitivity. *Eur Radiol Exp*. 2020;4(1):0-6. doi:10.1186/s41747-020-00191-0

20. Engineering B, Building ET. Confocal Endomicroscopy : Instrumentation and Medical Applications. 2012;40(2):378-397. doi:10.1007/s10439-011-0426-y

21. Zambelli A, Villanacci V, Buscarini E, et al. Confocal laser endomicroscopy in celiac

disease : description of findings in two cases. Published online 2007:1018-1020. doi:10.1055/s

22. Chauhan SS, Abu Dayyeh MPH BK, Bhat YM, et al. Confocal laser endomicroscopy. *Gastrointest Endosc*. 2014;80:928-938. doi:10.1016/j.gie.2014.06.021

23. Zhao HL, Zhang CP, Zhu H, Jiang YF, Fu XB. Autofluorescence of collagen fibres in scar. *Ski Res Technol*. 2017;23(4):588-592. doi:10.1111/srt.12375

24. Shen Y, Zhu D, Lu W, Liu B, Li Y, Cao S. The characteristics of intrinsic fluorescence of type I collagen influenced by collagenase I. *Appl Sci*. 2018;8(10). doi:10.3390/app8101947

25. Vol. 76, No. 4, 1977 BIOCHEMICAL AND BIOPHYSICAL RESEARCH COMMUNICATIONS ISOLATION. 1977;76(4):1124-1129.

26. Lutz V, Sattler M, Gallinat S, Wenck H, Poertner R, Fischer F. Impact of collagen crosslinking on the second harmonic generation signal and the fluorescence lifetime of collagen autofluorescence. *Ski Res Technol*. 2012;18(2):168-179. doi:10.1111/j.1600-0846.2011.00549.x

27. Sell DR, Monnier VM. Isolation, purification and partial characterization of novel fluorophores from aging human insoluble collagen-rich tissue. *Connect Tissue Res*. 1989;19(1):77-92. doi:10.3109/03008208909016816

28. Hansch A, Sauner D, Hilger I, et al. Autofluorescence spectroscopy in whole organs with a mobile detector system. *Acad Radiol*. 2004;11(11):1229-1236. doi:10.1016/j.acra.2004.07.027

29. Croce AC, Bottiroli G. Autofluorescence spectroscopy and imaging: A tool for biomedical research and diagnosis. *Eur J Histochem*. 2014;58(4):320-337. doi:10.4081/ejh.2014.2461

30. Hansch A, Sauner D, Hilger I, et al. Noninvasive diagnosis of arthritis by autofluorescence. *Invest Radiol*. 2003;38(9):578-583. doi:10.1097/01.RLI.0000077128.80730.03

31. Luetkemeyer CM, Marchi BC, Ashton-Miller JA, Arruda EM. Femoral entheseal shape and attachment angle as potential risk factors for anterior cruciate ligament injury. *J Mech Behav Biomed Mater*. 2018;88:313-321. doi:10.1016/j.jmbbm.2018.08.045

32. Rezakhaniha R, Agianniotis A, Schrauwen JTC, et al. Experimental investigation of collagen waviness and orientation in the arterial adventitia using confocal laser scanning microscopy. *Biomech Model Mechanobiol*. 2012;11(3-4):461-473. doi:10.1007/s10237-011-0325-z

33. Campagnola P. Second harmonic generation imaging microscopy: Applications to diseases diagnostics. *Anal Chem*. 2011;83(9):3224-3231. doi:10.1021/ac1032325

34. Prockop DJ, Fertala A. Inhibition of the self-assembly of collagen I into fibrils with synthetic peptides: Demonstration that assembly is driven by specific binding sites on the monomers. *J Biol Chem*. 1998;273(25):15598-15604. doi:10.1074/jbc.273.25.15598

35. Liu Y, Liu L, Chen M, Zhang Q. Double thermal transitions of type I collagen in

acidic solution. *J Biomol Struct Dyn*. 2013;31(8):862-873. doi:10.1080/07391102.2012.715042

36. Egelandsdal B, Kvaal K, Isaksson T. Autofluorescence spectra as related to tensile properties for perimysium from bovine masseter. *J Food Sci*. 1996;61(2):342-347. doi:10.1111/j.1365-2621.1996.tb14190.x

37. Benjamin M, Toumi H, Ralphs JR, Bydder G, Best TM, Milz S. Where tendons and ligaments meet bone: Attachment sites ('entheses') in relation to exercise and/or mechanical load. *J Anat*. 2006;208(4):471-490. doi:10.1111/j.1469-7580.2006.00540.x

38. Beaulieu ML, Carey GE, Schlecht SH, Wojtys EM, Ashton-Miller JA. On the heterogeneity of the femoral enthesis of the human ACL: microscopic anatomy and clinical implications. *J Exp Orthop*. 2016;3(1). doi:10.1186/s40634-016-0050-8

39. Magnussen RA, Taylor DC, Toth AP, Garrett WE. ACL graft failure location differs between allografts and autografts. *Sport Med Arthrosc Rehabil Ther Technol*. Published online 2012. doi:10.1186/1758-2555-4-22

40. Yang L. Theoretical and Numerical Analysis of Anterior Cruciate Ligament Injury and its Prevention. *Glob J Res Eng*. 2020;20(1):43-54. doi:10.34257/gjrejvol20is1pg43

41. Bojicic KM, Beaulieu ML, Imaizumi Krieger DY, Ashton-Miller JA, Wojtys EM. Association between lateral posterior tibial slope, body mass index, and ACL injury risk. *Orthop J Sport Med*. 2017;5(2):1-7. doi:10.1177/2325967116688664

42. Ateschrang A, Schreiner AJ, Ahmad SS, et al. Improved results of ACL primary repair in one-part tears with intact synovial coverage. *Knee Surgery, Sport Traumatol Arthrosc*. 2019;27(1):37-43. doi:10.1007/s00167-018-5199-5

43. Hyochol Ahn, et al 2017. 乳鼠心肌提取 HHS Public Access. *Physiol Behav*. 2017;176(10):139-148. doi:10.1038/nrc3566.Fluorescence-guided

CHAPTER 4

ACL Microfatigue and Collagen Unravelling – A Detailed Spectroscopic Analysis

4.1 Introduction

4.1.1 The molecular spectroscopic biomarker of denatured collagen in human ACL

Collagen – based tissues such as tendons and ligaments demonstrate remarkable ability to adapt to mechanical loads; however, overall ACL damage can still occur when the rate of damage exceeds the rate of repair. [1,2] The anterior cruciate ligament (ACL) is a connective tissue connecting the tibia and the femur, a dynamic part of the body distributing loads applied to them to execute movement.[3] The interface of the ligament and bone attachment – the enthesis – is a site of stress concentration and commonly subjected to overuse.[3] Clinically, most ruptures of the native ACL and graft ACL occur near the femoral enthesis. A study on multi-length scale characterization of the femoral enthesis of ACL as a result of fatigue, revealed that ACLs exhibited damage at the level of collagen molecules, fibrils and fibers. The molecular level damage was observed via atomic force microscopy – infrared spectroscopy (AFM-IR) as an amide I band shift from 1664 cm^{-1} to 1740 cm^{-1}.[4] The spectroscopic assignment was seen as a chemical change, representative of disruption to the collagen backbone structure from mechanical loading generating change in the stoichiometric amount of water associated with the triple helix leading to destabilization of the triple helix. The denaturation of collagen was further validated with the fluorescent probe, carboxytetramethylrhodamine (TAMRA) dye conjugated to a collagen hybridizing peptide (CHP), which specifically binds to single stranded

collagen associated with denatured helices. The intensity of the CHP-TAMRA in the mechanically tested ACLs were twice that of the mean percentage intensity of the controls (p = .02). This implies that 1740 cm^{-1} band can serve as a molecular spectroscopic biomarker to infer the quality of ACLs. To further investigate the conformation change in collagen suggested by the 1740 cm^{-1} band, another example of assignment of 1740 cm^{-1} as denatured collagen and the corresponding validation method is discussed. Then IR frequencies (Amide I and III band) known to be sensitive to the collagen conformation during denaturation are elucidated from literature. Additionally, other factors that contribute to collagen stability such as hydrophobic interactions, tyrosine and proteoglycans are discussed (Table 4.1). Finally, the 1740 cm^{-1} band, IR frequencies in the Amide I and Amide III band and tyrosine are examined to assess the correlation between these new spectroscopic biomarkers.

Table 4.1 *IR Wavenumber assignment*

Region	Wavenumbers (cm^{-1})	Assignment	References
Amide I	1740, 1738, 1724	Carbonyl vibration for denatured collagen to gelatin, gel, carbonyl, fatty acids, esters	Stani et al. (2019), Chen et al. (2019), Latour et al. (2016)
	1690	Antiparallel and parallel beta-sheet for globular proteins and collagen. Hydrogen bonds that involve the Cα-H of the amino acid in the Y position and the carbonyl group in the X position of type I collagen, histidinohydroxylysinonorleucine (HHL) and pyridolines (PYR) crosslinks.	Stani et al. (2019), Muyonga et al. (2004)
	1680, 1664, 1660	Ordered carbonyl backbone of triple helix, ascribed to residue X, typically, X = Proline	George and Veis (1991), Payne and Veis (1988)
	1630	Antiparallel and parallel beta-sheet for globular proteins and collagen, Pro-carbonyl H-bond mediated with larger number of water, denatured collagen.	Stani et al. (2019), George and Veis (1991), Payne and Veis (1988), Bryan et al. (2007)
Amide III	1292, 1284	H-bond involving C alpha-H of amino acid in the Y position and the carbonyl group in the X position of type 1 collagen	Stani et al. (2019)
	1272, 1268, 1257	Random conformation of denatured globular protein.	Stani et al. (2019), Jakobsen et al. (1983)
	1242	Cx = Ox ••• H – N inter-strand hydrogen bond in the triple-helix	Stani et al. (2019), Jakobsen et al. (1983)
Finger print	1176	C-O stretch of C-O-H and C-O-C from tyrosine and proteoglycans	Balan et al. (2019)

4.1.2 Spectroscopic assignment of denatured collagen in altered parchments

Parchment, used in museums, libraries and archives, is also derived from fibrillar collagen type 1 and its degradation also leads to denaturation of collagen to gelatin.[5] Characterization of gelatinized parchment with AFM-IR reveals a similar carbonyl vibration around 1724 cm^{-1} assigned as gel-carbonyl.[6] The spectroscopic signature was correlated with non-linear optical microscopy - second harmonic generation (SHG) and two-photon excited

fluorescence (2PEF), which are attributed to collagen cross-links and collagen's non-centrosymmetric organization at the molecular scale, respectively. The reduction in SHG signal intensity and increase in 2PEF signal were observed in the degraded parchment and reference samples of pure fibrillar collagen and gelatin, both of which possessed a gel-carbonyl peak at 1724 cm^{-1} and 1738 cm^{-1} respectively. The formation of the gel-carbonyl has hypothesized to be a result of formation of acidic species from acidification of collagen affecting the hydrogen bonding of the carbonyl.

4.1.3 Amide I band associated with denatured collagen

The conformational changes in the amide carbonyl groups along the polypeptide backbone during denaturation have been well-delineated by FTIR studies where the deconvolution of the Amide I band shows an intensification of the 1633 cm^{-1} peak and a diminishment of the dominant 1660 cm^{-1} peak.[7,8] Upon denaturation, the relative intensities of the 1660 and 1633cm^{-1} bands were shown to shift from greater than 1 to less than 1.[8] The large 30 cm^{-1} shift during denaturation is ascribed to increase in water mediated H – bonding of carbonyl of the proline residue, which is commonly the middle of the triplet amino acids in type 1 collagen Gly – X – Y. [8] The carbonyl of the X residue is shown to be extremely sensitive to conformation change related to an internal H – bond structure or interaction with the solvent water inferred by the Ramachandran diagram, which shows the inward orientation of the X residue's carbonyl whereas the Gly, Y carbonyls are exposed to the aqueous environment and are not likely to be conformationally dependent.[8] In addition, the relatively highly basic carbonyl of proline residue compared to that of glycine and hydroxyproline is also known to form stronger H – bond with free water. The assignment of the 1630 cm^{-1} to has been used to describe collagen denaturation from a variety of materials and methods: thermal denaturation of rat skin collagen and calf skin gelatin[8,9], acid solubilized skins of young and adult Nile perch[10], thermal denaturation of commercial type 1 collagen[11] and mechanically induced

fatigue on glutaraldehyde treated bovine pericardium[12]. Computational studies support that the hydration of helices generates an intensified 1630 cm^{-1} peak due to bifurcated H-bonding between helix and water molecules. [13,14]

4.1.4 Amide III bands associated with denatured collagen

The conformational changes in the Amide III region have also been described in the thermally driven fibrillogenesis and denaturation process of collagen. The Amide III band (1310 – 1175 cm^{-1}) is mainly associated with C-N stretching and N-H bending vibrations (30% each), C-C stretching (20%) and CH bending (10%).[11] The inter-strand hydrogen bond in the ordered triple helix $C_x = O_x$ ••• H – N is known to represent the Amide III vibrations. Jakobsen et al. showed that the 1257 cm^{-1} band in a collagen monomer solution reduced in intensity as the first phase of the fibrillogenesis, lag phase, began. In the lag phase, the intensity ratio was reversed, with the other amide III band 1242 cm^{-1} higher in intensity, and increasing even more during the final growth phase of the fibrils.[15] Another study reported similar variation in Amide I and Amide III regions during thermal denaturation of commercial type 1 collagen in acidic solution, which showed double thermal transitions - a minor transition where breakage of hydrogen bonding and partial unfolding of the triple helix occur, and a major transition recognized as the triple helix to single alpha helix then unordered single coil structures.[11,16,17] The spectral component of 1284 cm^{-1} have shown to be related to the 1690 cm^{-1} band (hydrogen bonding between alpha C-H and carbonyl); the 1268 cm^{-1} (random conformation of denatured globular protein) with the 1630 cm^{-1} band (carbonyl with solvent H-bonding due to denatured alpha chains); and 1225 cm^{-1} (beta sheet structures) with the 1620 cm^{-1} band (unordered insoluble aggregates); and 1202 cm^{-1} band with the 1610 cm^{-1} band (amino acids lateral chains).[11]

4.1.5 Collagen stabilizers: Hydrophobicity and tyrosine during fibrillogenesis

In addition to the importance of hydrogen bonding in the stability of collagen molecules and its organization into higher - order structures, other aspects such as hydrophobic effects and other constituents in the extracellular matrix (ECM) that contribute to collagen's structural integrity are discussed. X-ray diffraction data (longer H-bond length) and a blue shift of Amide I band during alteration of hydrogen bonding interaction of the carbonyl from within the helix to the aqueous environment infers that weak hydrogen bonding within the collagen backbone is not energetically favourable to drive fibrillogenesis.[7] An investigation into the drivers of collagen's spontaneously self-assembly with triple helical collagen mimetic peptides (CMP) showed that hydrophobic aromatic resides from the telopeptide regions of collagen play an important role in collagen self-assembly, especially the tyrosine (Tyr) and phenylalanine (Phe) residues within the C-terminal chain.[18,19] Recently, three specific binding sites of the tyrosine sulfate domain of fibromodulin (FMOD) on the collagen molecule has been characterized with EM, at the N terminus, and at 100 and 220 nm from the N terminus. The FMOD, a small leucine-rich proteoglycan (SLRP), has been shown to enhance fibril formation and this was shown to be dependent on the sulphated tyrosine residues which remained bound on the formed fiber.[20] The broad distribution of FMOD in connective tissue, especially in cartilage, has attracted attention as a candidate for biomolecular drug for osteoarthritis to promote chondrogenic development and regeneration.[21] Decorin and biglycan are SLRP which are important constituents of the ECM in ACL, and are also known to aid in regulation of collagen fibrillogenesis.[22] The aromatic side-chain rings of tyrosine can exhibit interesting physicochemical properties such as autofluorescence and UV absorption which can be used to monitor the intactness of collagen fibrils[23,24] It was shown that the dissociation of aggregated type 1 collagen by collagenase led to an increase in intrinsic fluorescence intensity of type 1 collagen due to the increased in the number of exposed tyrosine residues which were initially

wrapped in collagen during aggregation.[25] In addition, digestion of native collagen with pepsin, which cleaves peptides in the telopeptide region of collagen, exhibited a reduction in the near UV absorption spectrum at 276 nm attributed to tyrosine residues, due to the reduction in the number of tyrosine residues remaining on the collagen.

Table 4.2 *Selection of ratios and disordered, ordered component assignment*

Region	Ratios	Assignment
Amide I	1740 /1680	Disordered/Ordered
	1630/1680	Disordered/Ordered
Amide III	1292/1242	Disordered/Ordered
	1272/1242	Disordered/Ordered
Finger print	1176/1242	Disordered/Ordered

While the spectroscopic peak 1740 cm^{-1} has been validated to describe denatured collagenous tissue, its relative intensity with the ordered triple helix Amide I band has not been explicitly described for a native ACL or fatigued ACL. Furthermore, the conformation information has not been elucidated. In this study, existing spectroscopic benchmarks for denatured collagen was used to analyze AFM-IR measurements of human anterior cruciate ligament (ACL) to elucidate local protein conformation changes in association with the molecular spectroscopic biomarker of collagen denaturation 1740 cm^{-1}. The compilation of data from literature on spectroscopic signatures of collagen denaturation led to a selection of five IR ratios (1740 cm^{-1}/1680 cm^{-1}, 1630 cm^{-1}/1680 cm^{-1}, 1292 cm^{-1}/1242 cm^{-1}, 1272 cm^{-1}/1242 cm^{-1}, 1176 cm^{-1}/1242 cm^{-1}) (Table 4.2) to examine the trends and relationships between the variables as a result of mechanical loading. Our hypothesis is that all the ratios will show positive correlation with higher levels of collagen denaturation by mechanical testing.

4.2 Methods

4.2.1 Preparation of cadaveric knees, mechanical testing and explants for spectroscopic analysis

For this study, six paired knees were acquired from the University of Michigan Anatomic Donations Program and Gift of Life Michigan (Table 4.3). We followed the same procedures for preparing and mounting the adult human knees for mechanical testing as published previously. From the paired knees, one knee randomly selected for testing. See After mechanical testing was completed the methods for extracting each ACL from its knee complete with its bony origin and insertion, preserving and embedding the explant, and Kawamoto cryosectioning were performed as described previously. See chapter 2 methods section for more details.

Table 4.3 *Demographic of 6 paired knees (12 ACL's total) one of which has been mechanically tested and summary of data collection method. Hyperspectral dataset possess 1 micron spatial resolution whereas point spectrum are spread out ~ as large as 40 µm.*

Specimen	Sex	Age	Tested limb	Data collection method	Data points
C1	M	25	R	Point spectrum	63
C2	M	28	R	Point spectrum	217
C3	M	32	R	Point spectrum	80
C4	M	39	L	Point spectrum	87
C5	M	47	R	Point spectrum	79
C6	F	42	R	Hyperspectral	887

4.2.2 AFM-IR data collection

The AFM-IR data were collected with a NanoIR3 system (Bruker) in contact mode utilizing nIR2 probes (gold-coated silicon cantilever; nominal radius, 25nm; force constant, 0.07 – 0.4N/m; resonance frequency, 13 ± 4 kHz). The nIR2 test standard polystyrene – polymethylmethacrylate (PS-PMMA) sample (Bruker) was used for optimization of each of the four quantum cascade laser (QCL) chips which spans a continuous interval from 780 –

1890 cm^{-1}. The IR focus spot was set to 2429 pt. Background was collected over the entire QCL spectral range at 300cm^{-1}/s scan rate, 10 co-averages with a spectral resolution of 2 cm^{-1}.

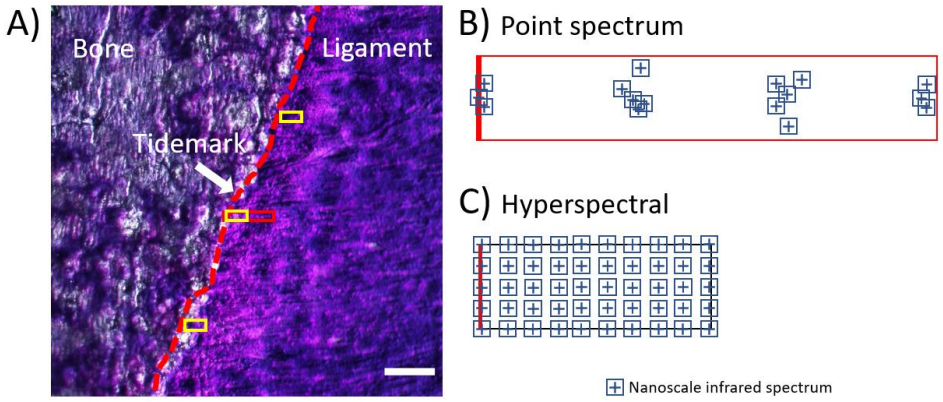

Figure 4.1 *Data collection location and method illustration. A) Toluidine blue stained ACL with imaging area in point spectrum method (red rectangle) and hyperspectral method (yellow rectangles) adjacent to the tidemark into the ligament region. Scalebar 100 µm. B) Point spectrum data collection method shows localized spectrum collection at a specified interval within 100 µm from tidemark. C) Hyperspectral data collection method shows a fixed 1 µm step size of IR spectrum collection in the imaging area of 50 µm from the tidemark.*

Data was collected in two methods within 100 µm from the tidemark into the ligament region: i) point IR spectrum and ii) 2D hyperspectral arrays from six paired adult ACL's (Figure 4.1, Table 4.3). For the point IR spectrum method, an average of 163 point IR spectra (with 8 co – averages) spanning 790 – 1850 cm^{-1} were taken for each of the samples C1 – C5. The spectrums were acquired at an interval of 20 – 40 µm from the tidemark, and at every interval location multiple spectrum were acquired in a localized manner (Figure 4.1B). For the hyperspectral method, 30 rectangular arrays of 5 x 25 µm with 1 µm step size was collected from one sample, C6 (Figure 4.1C). A maximum of two rectangular arrays were imaged adjacent to one another, spanning a 5 x 50 µm area from the tidemark into the ligament area. Then a maximum of two additional locations along the length of the tidemark was selected to carry out the same imaging procedure. Laser parameters were kept consistent between both methods: 3.37% laser power, 2.0% duty cycle and 1680 cm^{-1} attributed to carbonyl vibration of ordered triple helix as the wavenumber for tuning the resonant frequency of the tip to around 180 kHz. All spectra were subjected two post – processing functions on the Analysis Studio

software: i) deglitch and ii) 3rd order polynomial with five point Savitzky – Golay smoothing function for removing chip transition artefacts and noise respectively.

4.2.3 AFM-IR data analysis

All of the spectral data were analyzed with R Studios software. The processed spectra from Analysis software were further screened for negative signal intensity in the entire spectral range which led to 34% of data (276 out of 815) exclusion from the point IR spectrum dataset, and 80% of data (4039 out of 4926) exclusion from the hyperspectral dataset from further data analysis. Despite the high elimination of data points, this conservative approach was taken to ensure meaningful interpretation of data. In the remaining spectra (1426), Amide I bands 1740, 1680, 1630 cm^{-1}, Amide III bands 1292, 1272, 1242cm^{-1} and finger print region band 1176 cm^{-1} were selected for ratio analysis. 1680 cm^{-1} was selected to represent the carbonyl vibration of ordered triple helix due to the maximum intensity displayed in the dataset. The characteristic peaks were assigned based on literature on collagen (Table 4.1; wavenumber assignments). Five ratios (1740 cm^{-1}/1680 cm^{-1}, 1630 cm^{-1}/1680 cm^{-1}, 1292 cm^{-1}/1242 cm^{-1}, 1272 cm^{-1}/1242 cm^{-1}, 1176 cm^{-1}/1242 cm^{-1}) were designated as variables to assess the protein conformation changes in the Amide I, Amide III and finger print regions in normal and denatured collagen (Table 4.2; ratio assignments). All of the ratios are formatted as the ordered, native collagen band component in the denominator and the disordered, denatured collagen band component in the numerator, to represent an increase in ratio values parallel to an increased disorder or denatured collagen structure described by the ratio 1740 cm^{-1}/1680 cm^{-1}. To assess the trends and relationships between the assignment of protein denaturation 1740 cm^{-1}/1680 cm^{-1} with the rest of the IR frequencies in Amide I, Amide III and finger print regions, the mean value of 1740 cm^{-1}/1680 cm^{-1} associated with incremental increase in the rest of the ratios were plotted to determine positive or negative trends. Next, the range of 1740 cm^{-1}/1680 cm^{-1} ratio was binned to three intervals (0 – 0.3, 0.3 – 1.0, > 1.0) to represent normal, high, and extreme level

of collagen denaturation. Then the change in the remainder of the ratios (1630 cm^{-1}/1680 cm^{-1}, 1292 cm^{-1}/1242 cm^{-1}, 1272 cm^{-1}/1242 cm^{-1}, 1176 cm^{-1}/1242 cm^{-1}) according to the increasing levels of collagen denaturation were presented in box plots with p-values from Welch two sample t-test. Furthermore, principal component analysis (PCA) was performed using R Studios (correlation matrix method) to demonstrate the relationship between the variables.

4.3 Results

4.3.1 Behavior of collagen denaturation with respect to Amide I, Amide III and tyrosine ratios

Figure 4.2 shows the changes in the mean value of 1740 cm^{-1}/1680 cm^{-1} ratio (representative of collagen denaturation) with respect to increase in ratios from Amide I, Amide III bands and tyrosine from the point spectrum dataset (C1 – C5). The comparison of trends between the control and tested ACL clearly demonstrate the point of divergence where the tested samples possess higher perturbation to the collagen backbone. The point of divergence are summarized in Table 4.4. For the point spectrum data, all of the points of diversion are seen approximately around 1, in which the intensity of the numerator wavenumber (disordered component) becomes larger relative to the denominator wavenumber. While it can be seen that 1740 cm^{-1}/1680 cm^{-1} ratio increases positively with ratios in Amide I, III and tyrosine, it does not increase synchronously with all of them. The intersecting mean values of 1740 cm^{-1}/1680 cm^{-1} ratio vary among the different ratios (Table 4.5). The corresponding mean values of the 1740 cm^{-1}/1680 cm^{-1} ratio for the controls (0.53 – 0.68) in the point spectrum data set were used to define the upper limit of a normal level of damage described by the 1740 cm^{-1}/1680 cm^{-1} ratio. An approximate value was used. Ratio value of 0 – 0.5 was used to describe normal levels of damage, and 0.5 – 1.0 as high, and greater than 1.0 as extreme. The classification in

Figure 4.3 shows that all the ratios in the normal level of damage possess a mean of less than 1 as anticipated in relation to the data in Figure 4.2.

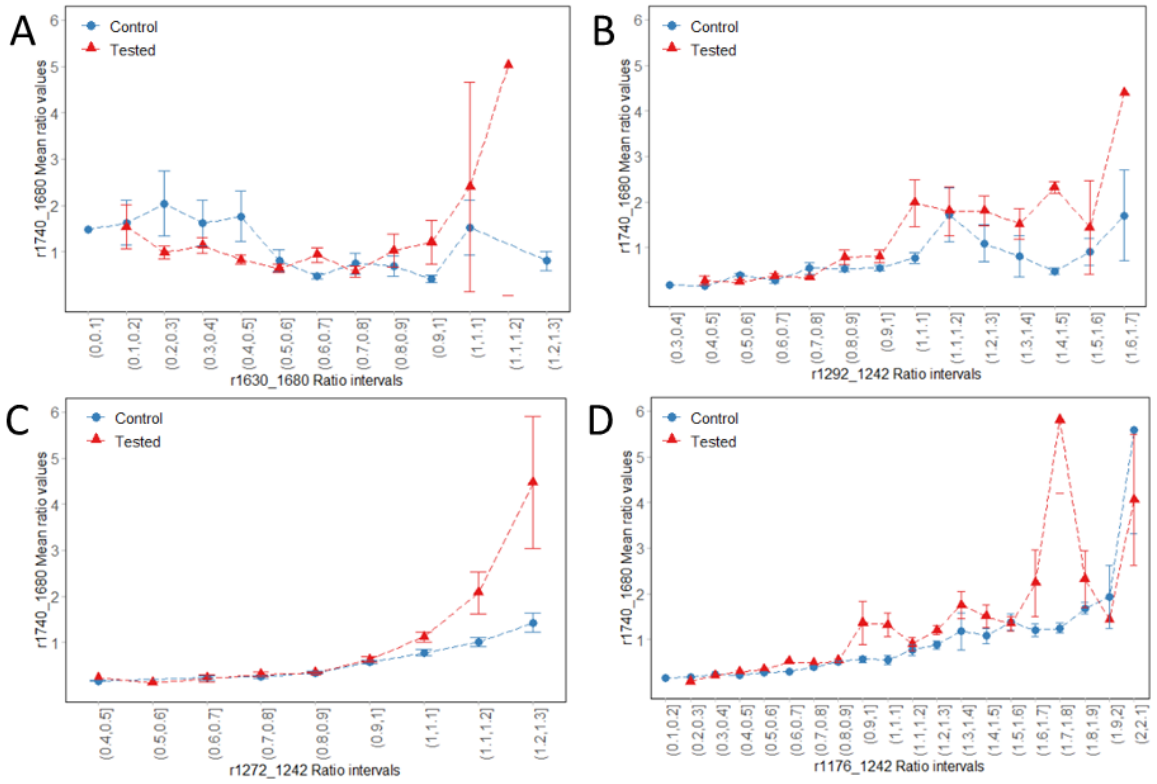

Figure 4.2 *Changes in collagen denaturation reflected by ratio 1740 cm^{-1}/1680 cm^{-1} with respect to incremental (step size: 0.1) change of A) Amide I ratio 1630 cm^{-1}/1680 cm^{-1}B) Amide III ratio 1292 cm^{-1}/1242 cm^{-1} C) Amide III ratio 1272 cm^{-1}/1242 cm^{-1} and D) fingerprint region 1176 cm^{-1}/1242 cm^{-1} from the point spectrum dataset. (circle, triangle: mean ± standard error bars; note variation in x-axis range for each plot)*

Table 4.4 *Summary of Amide I, Amide III and tyrosine ratio bins where point of divergence of control and tested sample occur seen in figure 4.2 (point spectrum dataset) and 4.4 (hyperspectral dataset).*

	1630/1680	1292/1242	1272/1242	1176/1242
Point spectrum	0.8 – 0.9	0.8 – 0.9	0.9 – 1.0	0.9 – 1.0
Hyperspectral	0.4 – 0.5	0.8 – 0.9	0.8 – 0.9	0.6 – 0.7

Table 4.5 *Summary of mean values of 1740 cm^{-1}/1680 cm^{-1} at the point of divergence between control and tested ACL from figure 4.2 (point spectrum dataset) and 4.4 (hyperspectral dataset).*

	1630/1680		1292/1242		1272/1242		1176/1242	
	Control	Tested	Control	Tested	Control	Tested	Control	Tested
Point spectrum	0.68	1.02	0.53	0.78	0.56	0.63	0.56	1.36
Hyperspectral	0.20	0.35	0.21	0.41	0.40	0.50	0.17	0.37

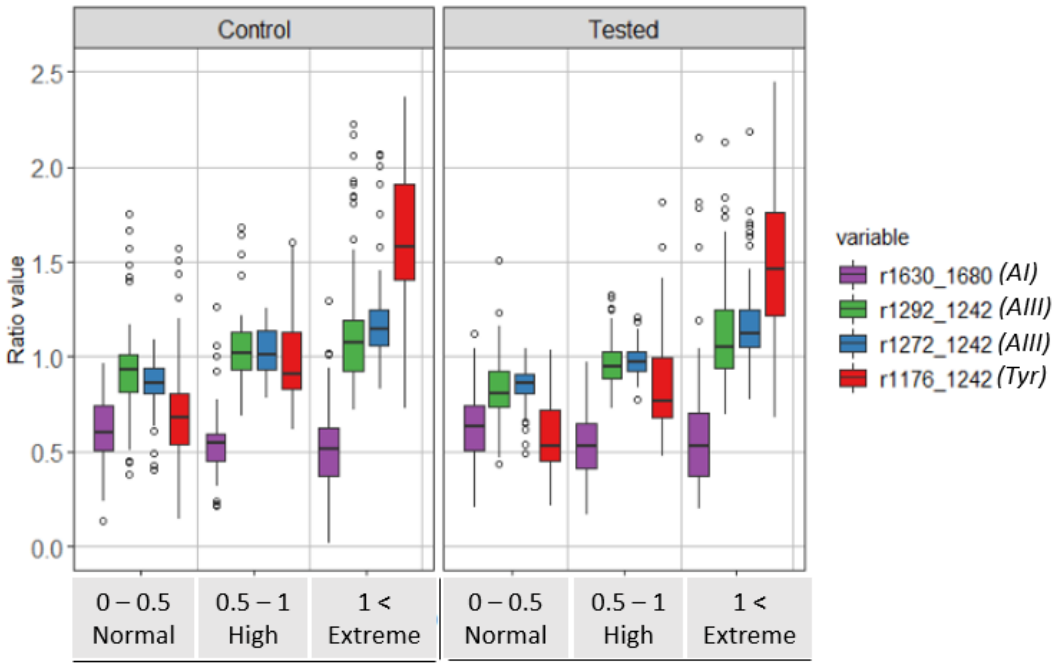

Figure 4.3 *Changes in Amide I ratio 1630/1680, Amide III ratio 1272/1242, Amide III ratio 1292/1242 and tyrosine residue 1176/1242 classified by degree of collagen denaturation (normal: 0 – 0.5, high: 0.5 – 1, extreme: 1.0 <) depicted by specified intervals of ratio 1740 cm^{-1}/1680 cm^{-1} in control versus tested ACL's from point spectrum dataset C1-5. Amide III and tyrosine region ratios increase with damage progression. Amide I remains unaffected during damage progression. (boxplot shows median line, mean value reported in table 4.6)*

Table 4.6 *Summary of mean values of ratios with respect to degree of collagen denaturation (normal: 0 – 0.5, high: 0.5 – 1, extreme: 1.0 <) from figure 4.3. p_1 denotes p-value between control and tested sample. P_2 denotes p-value with reference to values in the normal collagen denaturation level (bin 0 -0.5).*

	1630/1680			1292/1242			1272/1242			1176/1242		
1740/1680	**Control**	**Tested**	**p_1**	**Control**	**Tested**	**p_1**	**Control**	**Tested**	**p_1**	**Control**	**Tested**	**p_1**
0 – 0.5	0.62	0.63	0.75	0.92	0.82	< 0.001	0.86	0.85	0.35	0.71	0.57	<0.001
0.5 – 1.0	0.55	0.53	0.48	1.04	0.97	0.01	1.03	0.98	0.009	1.00	0.86	0.003
1.0 <	0.56	0.62	0.41	1.78	1.11	0.02	1.65	1.19	0.01	2.68	1.62	0.007
p_2	0.11†	.015†		<0.001	<0.001		<0.001	<0.001		<0.001	<0.001	

† Mean value in extreme level of damage (>1.0) is not statistically significant with reference to normal level of damage (0 – 0.5)

The summary of mean values the ratios with increasing levels of damage shows strong statistical significance (p_2 <0.001) for the Amide III and tyrosine ratios but not with Amide I ratio (Table 4.6). Counterintuitively, the control samples display a higher ratio value than that of controls with mixed statistical significance (p_1 values: 0.001 – 0.75)

Figure 4.4 shows the changes in the mean value of 1740 cm^{-1}/1680 cm^{-1} ratio (representative of collagen denaturation) with respect to increase in ratios from Amide I, Amide III bands and tyrosine from the hyperspectral dataset (C6). Similar to the trends seen in Figure 4.2, the 1740 cm^{-1}/1680 cm^{-1} ratio increases positively with increasing ratios in Amide I, III and tyrosine. The point of divergence are summarized in the second row of Table 4.4. A comparison between the datasets (point spectrum versus hyperspectral) show lower ratios at the point of divergence for the Amide I and tyrosine ratios. The corresponding mean values of the 1740 cm^{-1}/1680 cm^{-1} ratio in Table 4.5 were also lower than values in the point spectrum.

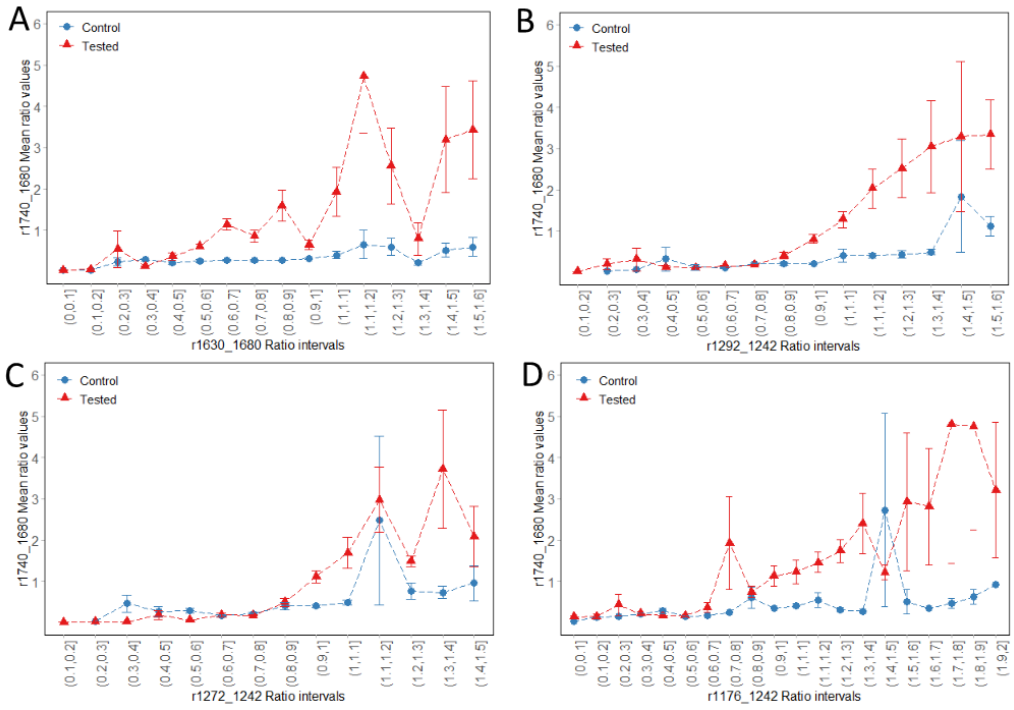

Figure 4.4 *Changes in collagen denaturation reflected by ratio 1740 cm^{-1}/1680 cm^{-1} with respect to A) Amide I ratio 1630 cm^{-1}/1680 cm^{-1} B) Amide III ratio 1292 cm^{-1}/1242 cm^{-1} C) Amide III ratio 1272 cm^{-1}/1242 cm^{-1} and D) fingerprint region 1176 cm^{-1}/1242 cm^{-1} from the hyperspectral dataset. (circle, triangle: mean ± standard error bars; note variation in x-axis range for each plot)*

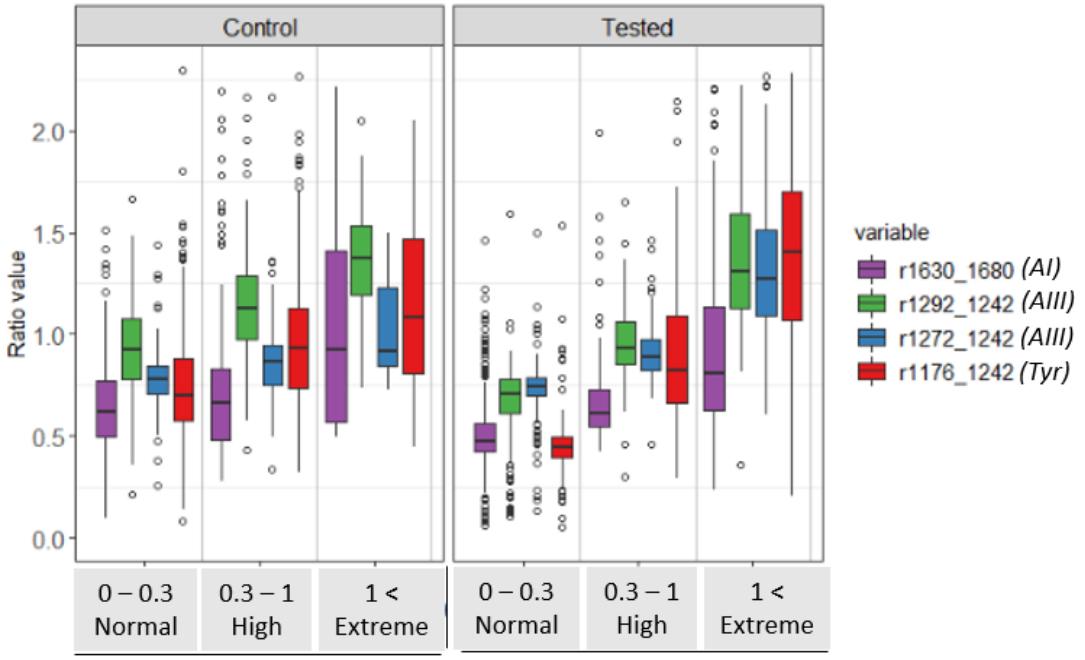

Figure 4.5 *Changes in the ratios classified by degree of collagen denaturation (normal: 0 – 0.3, high: 0.3 – 1, extreme: 1.0 <) depicted by specified intervals of ratio 1740 cm^{-1}/1680 cm^{-1} in control versus tested ACL's from hyperspectral dataset C6. Amide I, amide III and tyrosine region ratios increase with damage progression. (boxplot shows median line, mean value reported in table 4.7)*

Table 4.7 *Summary of mean values of ratios with respect to degree of collagen denaturation (normal: 0 – 0.3, high: 0.3 – 1, extreme: 1.0 <) from figure 4.5. p_1 denotes p- value between control and tested sample. p_2 denotes p-value with reference to values in the normal collagen denaturation level (bin 0 – 0.3)*

	1630/1680			1292/1242			1272/1242			1176/1242		
1740/1680	**Control**	**Tested**	**p_1**	**Control**	**Tested**	**p_1**	**Control**	**Tested**	**p_1**	**Control**	**Tested**	**p_1**
0 – 0.3	0.64	0.53	<0.001	0.93	0.67	< 0.001	0.77	0.73	<0.001	0.75	0.47	<0.001
0.3 – 1.0	0.88	0.71	<0.001	1.18	0.98	<0.001	0.89	0.92	0.34	1.09	0.93	0.03
1.0 <	5.22	1.92	0.08	1.36	1.86	<0.001	1.03	1.76	<0.001	1.40	3.08	<0.001
p_2	<0.001	<0.001		<0.001	<0.001		<0.001	<0.001		<0.001	<0.001	

The mean values of the controls were then used to define the upper limit of the normal level of damage: 0.3 due to the smaller mean values (0.17 – 0.4) seen in the control samples. Thus the ratio value of 0 – 0.3 was used to describe normal levels of damage, and 0.3 – 1.0 as high, and greater than 1.0 as extreme. The changes in the Amide I, III and tyrosine ratios with respect to normal, high and extreme levels of damage are displayed in Figure 4.5. The summary of ratios in Table 4.7 display an increase in all of the ratios with higher levels of denaturation (p_2 <0.001). The comparison of the control and tested exhibit higher ratio values in the controls, except for in extreme levels (>1.0) of denaturation.

To better display the relationship between the various Amide I and Amide III band ratios and how they differ in a control and mechanically tested ACL, PCA was performed for both datasets. First the hyperspectral data was analysed, then the point spectrum data.

4.3.2 Principal component analysis (PCA)

To determine the number of principal components (PCs) to examine, a scree plot was generated to illustrate the percent of variance explained by each component. The results display a total of five PCs in each of the control and tested ACL due to the number of original input variables, or ratios (Figure 4.6). The percent variance threshold for PC selection is 20%, which is the theoretical contribution of a PC if all components contributed equally to the total variance. Therefore, PC 1 and 2 are selected for both control and tested ACL, which amounts to 78.2% and 92% explained variance when combined, for each control and tested ACL respectively. A variable correlation plot with quality of representation (cos2) in the two PCs is depicted in Figure 4.7. Separate plots of the control and tested ACL can show how the relationship between the variables are similar or different to one another when there is an increase in collagen denaturation due to mechanical loading. In this case, the control and tested plot differ from one another, highlighting how important patterns may be diluted or missed when groups are combined. The arrows represent the variable vectors, where the angle between

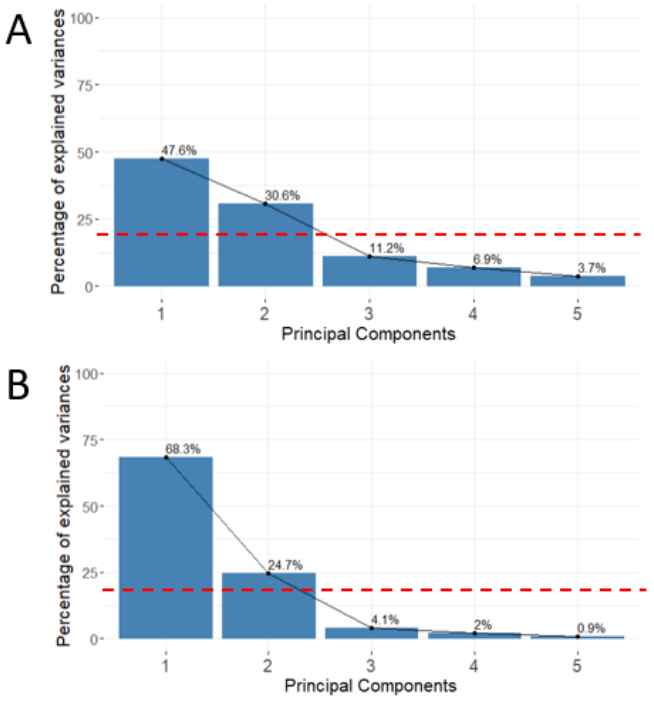

Figure 4.6 *The scree plot of hyperspectral data A) control and B) tested ACL from a paired knee. For both A and B, principal component 1 and 2 pass the percent variance threshold (> 20% in red dotted line) to be selected for PCA. PC 1 and 2 of control explain 78.2% of variance in data, and 92% of data in the tested.*

any two vectors represents the correlation between the two variables, and the length of the vectors indicate the quality of representation (cos2) of the variable on the plot. The control ACL (Figure 4.7A) shows a segregation of variables in two groups in nearly orthogonal to one

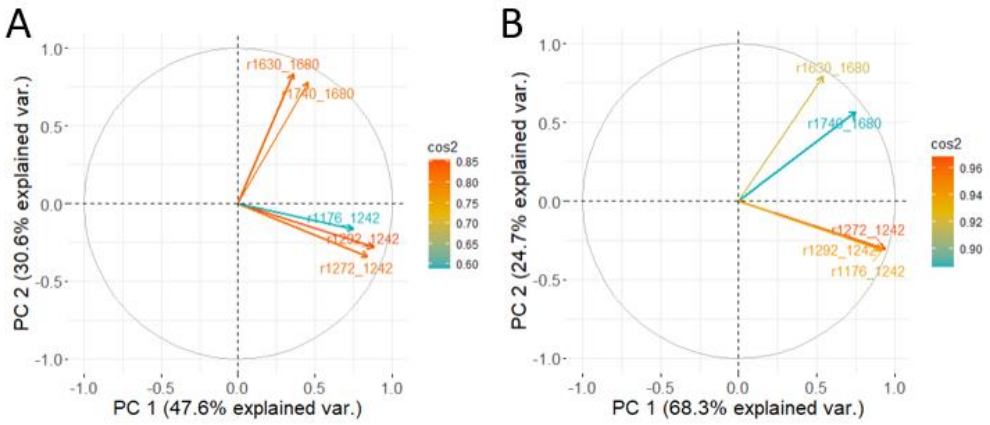

Figure 4.7 *Variable correlation plots of A) control and B) tested ACL from hyperspectral dataset. A)Control ACL shows segregation of variables in two groups which show strong correlation within groups. B)Tested ACL shows increased correlation strength between r1740_1680 and tyrosine residues and the Amide III vectors. The r1630_1680 vector position shifts slightly in the tested ACL.*

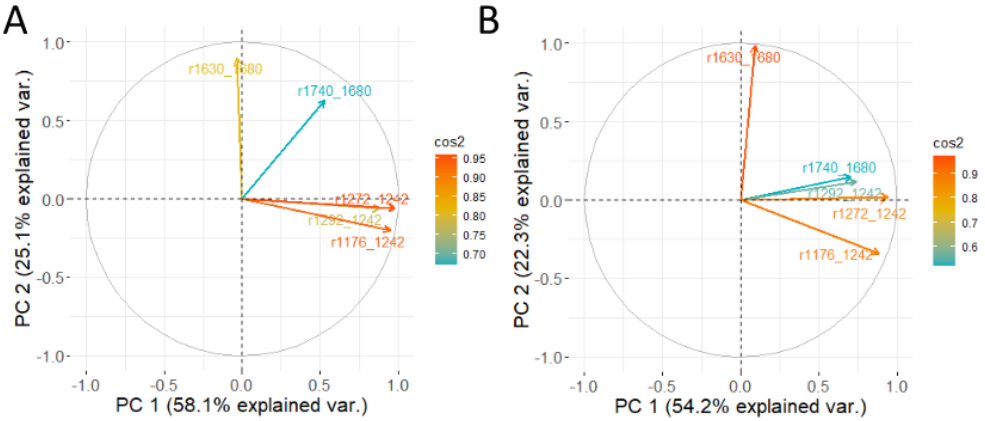

Figure 4.8 *Variable correlation plots of A) control and B) tested ACL from point spectrum dataset. A)Control ACL show similar orthogonal separation of two groups, except the r1740_1680 vector lying in the middle of the groups, indicating a moderate strength of correlation with the other groups. B)Tested ACL shows increased correlation strength between r1740_1680 and tyrosine residues and the Amide III vectors. The r1630_1680 vector position shifts slightly in the tested ACL.*

another, indicating a lack of correlation between the two groups. The first group of variables with a dominant representation along PC 1 include the Amide III (1292 cm^{-1}/1242 cm^{-1}, 1272 cm^{-1}/1242 cm^{-1}) and tyrosine ratio (1176 cm^{-1}/1242 cm^{-1}), which show slight differences however, are overall strongly correlated with one another. The second group of variables with a dominant representation along PC 2 include the Amide I region ratios (1740 cm^{-1}/1680 cm^{-1}, 1630 cm^{-1}/1680 cm^{-1}), which also show high correlation to one another. For a given variable, the sum of the cos2 (quality of representation) on all of the PCs is equal to one. Therefore,

variable vectors that are long enough to reach the circumference of the correlation circle indicate excellent representation by PC 1 and 2. The quality of representation is the very high for 1292 cm^{-1}/1242 cm^{-1}, 1272 cm^{-1}/1242 cm^{-1} in the first group and 1740 cm^{-1}/1680 cm^{-1}, 1630 cm^{-1}/1680 cm^{-1} in the second group. 1176 cm^{-1}/1242 cm^{-1} possessed the shortest vector displaying the least representation. Overall, the tested ACL (Figure 4.7B) shows development of stronger representation in the PC1 from all the variables compared to the control, seen by a reduction in the angle among the variable vectors and increase in lengths. The Amide III (1292 cm^{-1}/1242 cm^{-1}, 1272 cm^{-1}/1242 cm^{-1}) and finger print region ratio (1176 cm^{-1}/1242 cm^{-1}) vectors become collinear, indicating a strong positive correlation and equally strong representation of PC1. Thus, their minimal representation of PC2 are diminished even further for ratios 1292 cm^{-1}/1242 cm^{-1} and 1176 cm^{-1}/1242 cm^{-1}. The angle between the two groups are minimized especially due to the shift of r1740_1680 vector toward the collinear Amide III and finger print region variables, indicating a stronger positive correlation between 1740 cm^{-1}/1680 cm^{-1} and the group 1 variables than seen in the control sample. Subsequently, the correlation between 1740 cm^{-1}/1680 cm^{-1} and 1630 cm^{-1}/1680 cm^{-1} are weakened, but still remain stronger than compared with the other variables. The angle between the collinear Amide III and finger print region vectors still display a perpendicular angle with 1630 cm^{-1}/1680 cm^{-1}, indicating an uncorrelated relationship. The quality of representation in PC1 increased for all variables, in line with the larger percentage of variance explained in PC1 in Figure 4.6B.

The determination of PCs for the point spectrum dataset were performed with the same method. The first two PCs were selected for both control and tested ACL, which amounts to 83.2% and 76.5% explained variance when combined, for each control and tested ACL respectively. The variable correlation plot of the control and tested display a similar orthogonal separation between 1630 cm^{-1}/1680 cm^{-1} and Amide III and tyrosine ratios similar to hyperspectral data, however, the 1740 cm^{-1}/1680 cm^{-1} variable show approximately similar

strength of correlation with the 1630 cm^{-1}/1680 cm^{-1} and Amide III and tyrosine ratios in the control sample (Figure 4.8A). The strength of correlation of 1740 cm^{-1}/1680 cm^{-1} and Amide III bands increase in the mechanically tested sample (Figure 4.8B), drawing the disordered vector further away from ratio 1630 cm^{-1}/1680 cm^{-1}, which remain weakly correlated with the remainder of the variables. Despite the increase in correlation between 1740 cm^{-1}/1680 cm^{-1} and Amide III ratios, the quality of representation with PC1 and PC2 is reduced along with 1292 cm^{-1}/1242 cm^{-1} as seen by the reduction in vector length, whereas ratio 1272 cm^{-1}/1242 cm^{-1} still remain strongly represented by PC1. The difference in the quality of representation suggests different trends of the ratios.

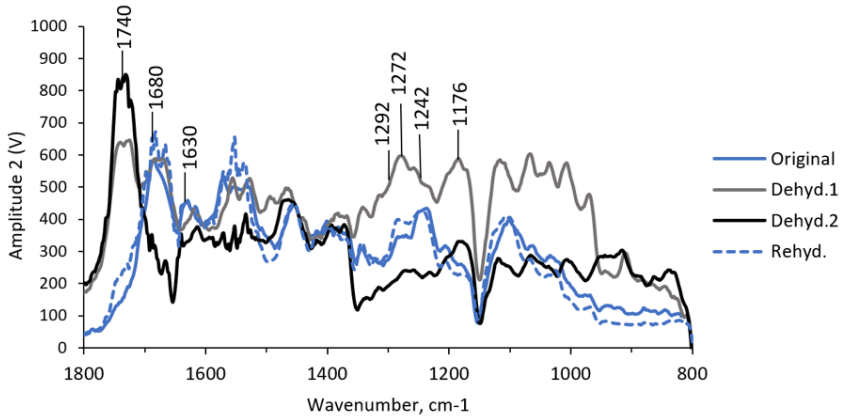

	1740/1680	1630/1680	1292/1242	1272/1242	1176/1242
Original	0.25	0.81	0.72	0.81	0.59
Dehyd. 1	1.10	0.67	1.07	1.14	1.09
Dehyd. 2	2.88	1.18	0.93	1.09	1.48
Rehydrated	0.36	0.74	0.84	0.92	0.53

Figure 4.9 *Intentional dehydration and rehydration of ACL with N_2 gas and the respective ratio measurements after each treatment. All ratio values increase with dehydration sequence 1 (except for r1630_1680), then increase again after dehydration sequence 2 (except for the Amide III ratios r1292_1242 and r1272_1242). The values are reversed close to their original values after rehydration*

An additional test was performed to observe the changes in the ratios in relation to the generation of the 1740 cm^{-1} band by intentional dehydration with N_2 gas (Figure 4.9), which destabilizes the triple helix due to deformation of a tetrahedral network of hydrogen bonds in the kinetically labile first hydration shell.[26] Dehydration sequence 1 represents three minutes of N_2 exposure and dehydration sequence 2 represents 2 hours of N_2 exposure. Rehydration sequence was performed by washing of tissue with 1 mL deionized water for five times. The

original measurements prior to any treatment reflect pre-existing damage displayed by the 1740 cm^{-1}/1680 cm^{-1} ratio value of 0.25. The remaining four ratios display higher intensities, however they are still less than 1, indicating a more dominant relative intensity of the wavenumber in the denominator, ascribed to an ordered triple helix conformation. The Amide I band ratio 1630 cm^{-1}/1680 cm^{-1} possess 0.81 identical with the amide III band 1272 cm^{-1}/1242 cm^{-1} ratio value. The 1292 cm^{-1}/1242 cm^{-1} ratio exhibits a slightly reduced value of 0.72 and the tyrosine ratio 1176 cm^{-1}/1242 cm^{-1} exhibits 0.59. After the initial dehydration sequence, the 1740 cm^{-1} intensity grows with the ratios in the Amide III region, and tyrosine increasing to above 1. On the other hand, the Amide I band 1630 cm^{-1}/1680 cm^{-1} showed a reduction from 0.81 to 0.67. After the second dehydration sequence, the 1740 cm^{-1}/1680 cm^{-1} ratio increased by over two-fold to 2.88, and the 1630 cm^{-1}/1680 cm^{-1} ratio escalated to 1.18. The tyrosine residue ratio escalated to 1.48 and the Amide III intensity showed the least amount of change, but remained around 1. After rehydration, most of the ratios are reversed nearly back to its original values except for the 1630 cm^{-1}/1680 cm^{-1} and tyrosine ratio which were slightly less than the original ratio value.

4.4 Discussion

In this work, we have showed explicit changes in the relative ratios of the IR frequencies related to denatured conformation of collagen with respect to a relatively novel spectroscopic biomarker of fatigue damage in ACL, 1740 cm^{-1}. Subsequently, the ratios were used to identify the point of divergence seen between the control and tested samples, and an approximate "normal range" of damage was determined. Further classification into high and extreme levels of damage exhibited that Amide I, Amide III and tyrosine ratios increased with increasing levels of damage (1740 cm^{-1}/1680 cm^{-1} ratios) ($p_2 < 0.001$ in Tables 4.6 and 4.7). However mean values of Amide I, Amide III and tyrosine ratios between control and tested showed

higher values in the control with some statistical significance (see p_1 values in Tables 4.6 and 4.7). Therefore, we confirmed the hypothesis that Amide III and tyrosine residue ratios increase with fatigue damage in ACL, 1740 cm^{-1} while Amide I shows variation. Denaturation by dehydration exhibit changes in the five ratios similar to that of mechanical denaturation in that the magnitude of increase in the ratios with dehydration sequence was non-uniform. These findings suggest that the denaturation of the triple helix occurs by multiple local conformation changes affecting the amide bonds leading to helical instability.

4.4.1 Ratios of Amide I, Amide III and tyrosine at the point of divergence

Figure 4.2 displays the point of divergence between control and tested near ratio values of 1 for all four ratios (Table 4.4). This means the conformation associated with each ratio all indicate denatured collagen – increased hydrogen bonding with solvent and or weakened inter-strand H-bonding, and exposure of tyrosine residues from disassembled collagen. It would seem that the 1740 cm^{-1}/1680 cm^{-1} ratios would only appear when the Amide I, Amide III and tyrosine ratios also indicate completely denatured conformation (ratio > 1) of collagen, but this is not the case seen in Figure 4.4. The point of divergence for the Amide I and tyrosine ratio (Table 4.4 row 2) are seen below 1, and the reported mean values of 1740 cm^{-1}/1680 cm^{-1} indicate that the relative intensity of the 1740 cm^{-1} band is at least 17 – 35% that of the 1680 cm^{-1} band. The simultaneous growth of denatured carbonyl ascribed bands – 1630 cm^{-1} and 1740 cm^{-1} suggests that the denaturation process may occur in many steps and different pathways thus multiple, localized denaturation may occur along the molecule. Denaturation by dehydration sequence 1 induced a growth of the 1740 cm^{-1} peak intensity while 1630 cm^{-1} becomes slightly reduced, indicating an increase in disruption for some amide I moieties but not for other amide I groups (Figure 4.9). Then in dehydration sequence 2, both amide I vibrations 1740 cm^{-1} and 1630 cm^{-1} become enhanced. A structural investigation of the thermal response of type 1 collagen in acidic solution has been shown to undergo a double thermal

transition where the initial thermal transition at 37°C corresponded to a partial unfolding of the triple helices which were reversibly renatured with cooling, and the latter thermal transition at 55°C corresponded to the complete denaturation of the major part of the triple helices which were irreversibly denatured.[16] The reversal of all five ratios to close to their original values upon rehydration of tissue (Figure 4.9) indicate that the additional water molecules re-stabilized the collagen triple helix by mediating hydrogen bonds where there were partial unfolding and or, renature native hydrogen bonds driven by hydrophobic interactions. Hydroxyproline (Hyp) residue may play a role in the reversible helix formation as its polar, rigid side chain is known to stabilize the helix through water-mediated hydrogen bonds, although this effect is position sensitive - they are shown to be the most effective only when it is located in the Y position of the common Gly – X- Y triplet sequence.[26] Additionally, computational data suggests water-mediated stabilizations also hold for charged residues.[26] This may include glycosaminoglycans (GAG) which is a highly negatively charged extracellular matrix constituent in the ACL, providing lubrication between collagen fibrils allowing a greater degree of deformation to resist damage.[27] The reversibility of the five ratios in the dehydration data also suggests that the collagen structure associated with IR bands 1740 cm^{-1} and 1630 cm^{-1} can describe reversible partially-unfolded helices. However, the maximum ratio value or degree of partially unfolded helices to allow renaturation is unknown. Dynamic light scattering measurements of collagen fibrillar aggregates during thermal denaturation have been reported to display two separate hydrodynamic radius distributions indicating two sizes of collagen aggregates.[16] These two aggregates reflected differences in temperature sensitivity, in which the inter-triple helix hydrogen bonds of the smaller size aggregates were easier to break than the larger ones thus the ones to undergo partial unfolding during the minor thermal transition at 37°C. TEM images of the minor thermal treatment showed the preservation of d-spacing which were absent in the major thermal transition. Renaturation of helix growth is also known to occur in two stages: an

immediate fast rate of helix growth followed by a much longer, slow helix-growth rate due to the high proportion of peptide bonds which must undergo *cis* to *trans* isomerization reactions, which have a high activation energy (~72 kJ mol^{-1}) in order to form the triple helix.[28,29] This can explain the ratios that were reversed nearly back to its original values, not exactly the same. Due to the AFM-IR being such a local technique, it is possible that it detects regions of local order and disorder such as described by the ratio values. McMillan et al. employed microbeam laser-excited Raman spectroscopy to characterize collagen in cartilage samples that has undergone high temperature (>100°C), and then freeze-drying generated a peak at 1788 cm^{-1} ascribed to stretching vibration of the carboxylic group v(-COOH) as a consequence of partial hydrolysis occurring at the peptide linkage.[30] As seen in this case of extreme temperatures required to generate the 1788 cm^{-1} band, the formation of the 1740 cm^{-1} band or gel – carbonyl in collagen may also indicate an extreme level of denaturation, where another region on the molecule contributing to the stability of the molecular structure is compromised. One of the motivations in research on collagen-to-gel formation and contraction is related to wound healing. One central element of wound healing is contraction of the wound, which involves interaction between dermal fibroblasts and dermal interstitial collagens. It has been found that collagen telopeptide sites play an important role in collagen gel lattice contraction. When acid solubilized collagen is brought to physiological salt and pH at temperature of 37°C, a gel-like mass of reconstituted fibrils are formed. [31] In the presence of dermal fibroblasts, collagen gel begins to tract from all sides resulting an round or oval shape that is a fraction of the original size of the gel.[31] Research on hydrogelators – small organic molecules capable of gelling aqueous solvents – has also examined collagen, as it meets the amphiphilic requirements of hydrogelators. Hydrogelators must possess hydrophobic and hydrophilic pockets on the outer surface. Collagen meets this requirement with its hydrophobic proline residue, due to its cyclic imino group, and the hydroxyproline residue, with a hydroxyl group that is hydrophilic.[32]

Furthermore, Prockop and Fertala demonstrated via molecular modelling the importance of hydrophobic and electrostatic interactions in the C-telopeptide to drive fibril formation. In their simulation, the mutation of two tyrosine residues and one phenylalanine residue abolished all effects on fibril formation, whereas mutating two aspartate residues had no effect.[33] The ACL is known to be avascular, except for mainly in the synovium sheathe,[34] which attributes to its poor reparative capacity[35] and a lack of a blood clot that typically forms across a wound site.[36] Is gelatinization in the ACL due to damage similar to a "blood clotting" mechanism for wounds without blood supply?

4.4.2 Changes in Amide I, Amide III and tyrosine ratios by damage levels

The results of the changes in Amide I, Amide III and tyrosine IR ratios associated with normal, high and extreme levels of collagen denaturation are summarized in Table 4.6 and 4.7. The changes in the trend between 1740 cm^{-1}/1680 cm^{-1} ratio and 1630 cm^{-1}/1680 cm^{-1} were hypothesized to be positively correlated due to 1630 cm^{-1} assignment to carbonyl vibration with water mediated H-bonding due to denatured alpha chains [8,11]. However, the mean values of 1630 cm^{-1}/1680 cm^{-1} ratio value remain relatively stagnant around 0.55 – 0.63 in all three levels of collagen denaturation (normal, high and extreme) seen in Table 4.6, with no statistically significant change represented by the low high p_1 and p_2 values. The p_1 denotes the p-value between control and tested sample while the p_2 denotes p-value of increase in damage with reference to the baseline or normal level of damage. This ratio's unchanging behavior is reflected in the corresponding PCA analysis (Figure 4.8) where the r1630_1680 vector only shows slight changes in its position and length in the control and tested sample, but largely remain orthogonal to the rest, indicating a lack of correlation. However, in the control sample, the two vectors r1630_1680 and r1740_1680 display moderate correlation (Figure 4.8A) possibly inferring that the 1630 cm^{-1}/1680 cm^{-1} ratio value around 0.55 – 0.62 (Table 4.6) is more related to the disorder represented by 1740/1680 seen in the control sample than that of

the higher levels of disorder in the mechanically tested sample. In Table 4.7, the level of 1630/1680 ratio are significantly (p_1 <0.001) larger in the control in the normal and high levels of collagen denaturation but not in the case of extreme levels of collagen denaturation (>1.0). However, independent of mechanical testing, the increase in 1630/1680 ratio, or increased interaction of the carbonyl with water, does significantly correlate (p_2 < 0.001) with increased collagen denaturation. The PCA variable correlation plot (Figure 4.7) displays the highest correlation between the Amide I region vectors r1630_1680 and r1740_1680 and the Amide III and tyrosine vectors with one another. In the fatigue loaded sample all the vectors draw closer, indicating increased correlation among them. However, the angle between the vectors r1630_1680 and r1740_1680 widens in the mechanically tested sample, indicating a loss of correlation between the carbonyl ascribed to increase in hydrogen bonding with solvent water molecules rather than from within the helix. The difference between the point spectrum and hyperspectral can be attributed to biological variation in samples C1 – C5 leading to pooled information.

The conformational changes in the Amide III region describes changes in the inter-strand hydrogen bond in the triple helix Cx = Ox --- H – N. Relative intensities of 1292 cm^{-1} /1242 cm^{-1} and 1272 cm^{-1} /1242 cm^{-1} greater than 1 are ascribed to increased water mediated H- bonds due to collagen denaturation. It was hypothesized that the tested sample will possess higher ratio values than the control due to accumulation of fatigue, however, the opposite is observed in Table 4.6. Table 7 exhibit similar patterns, except in the extreme level of collagen damage (> 1.0) exhibits statistically larger (p_1 < 0.001) amide III ratios for the tested samples. However, increase in the ratios with progressively higher degrees of collagen denaturation show strong statistical significance (p_2 < 0.001) in both table 4.6 and 4.7. These are further corroborated by the PCA variable plots where the angle between the r1740-1630 and amide III vectors are reduced in the mechanically tested sample (Figure 4.7, 4.8). Raman characterization of calf

skin gelatin shows an increase in the Amide III mode vibrations 1274 cm^{-1} as the existing 1248 cm^{-1} band widens to form a shoulder. [37] It is hypothesized that these Amide III bands do not come from proline or hydroxyproline residues as they have no amide hydrogen due to its sterically cumbersome cyclic imino groups, leading no Amide III mode, which involves the NH in-plane bending motion.[37] Therefore, the generation of the 1274 cm^{-1} band is hypothesized to stem from non-proline residue or a polar region of a the denatured collagen chain. [37]

Higher relative intensity of 1176 cm^{-1} / 1242 cm^{-1} is attributed to increase in the number of exposed tyrosine residues due to collagen denaturation. However, comparisons between normal and tested ACL show larger ratio in the control sample ($p_1 < 0.001$) in Table 4.6 and 4.7, except for in the extreme level of collagen damage (>1.0) in Table 4.7. Recent study identified three binding sites of tyrosine sulfate domain of fibromodulin on the type 1 collagen molecule – at the N terminus, and at 100 and 200 nm from the N terminus.[20] Electron microscopy illustrated the binding of fibromodulin on collagen at the borders between the overlap and gap regions, otherwise known as the D - spacing of collagen. Mechanical stimuli can stretch the elastic region which can alter local D - spacing values.[1] It is possible that the increase in exposure of tyrosine residues is also related to the alteration of D - spacing values. In addition, its importance in fibril assembly is confirmed due to its role in providing hydrophobic interactions at the C - telopeptides, which play an important role in collagen gel lattice contraction. Therefore, its association with denaturation seems highly possible. In the PCA analysis, the r1176-1630 vector behaves similarly with the Amide III vectors r1292-1242 and r1272_1272 with respect to r1630_1680 and r1740_1680 (Figure 4.7 and 4.8). It remains the least correlated with r1630_1680 in both control and tested samples, but increase in correlation in the mechanically tested sample. However, a slight loss of correlation among the tyrosine and Amide III bands are seen in the tested sample (Figure 4.8) as the angle between the vectors widens and the contribution from PC2 increases.

4.5 Conclusion

In conclusion, five IR ratio values (1740 cm^{-1}/1680 cm^{-1}, 1630 cm^{-1}/1680 cm^{-1}, 1292 cm^{-1}/1242 cm^{-1}, 1272 cm^{-1}/1242 cm^{-1}, 1176 cm^{-1}/1242 cm^{-1}) were analyzed from six paired control and mechanically tested ACLs to elucidate the conformation changes in collagen after fatigue damage development. A comparison of the change in 1740 cm^{-1}/1680 cm^{-1} ratio values between the control versus the tested ACL exhibited a point of divergence where the tested ACL displayed higher denatured collagen levels than in control ACL (Figure 4.2 and 4.4). The 1740 cm^{-1}/1680 cm^{-1} ratio values were used to generate three levels of collagen damage: normal, high and extreme. These classifications were used to examine how the ratios 1630 cm^{-1}/1680 cm^{-1}, 1292 cm^{-1}/1242 cm^{-1}, 1272 cm^{-1}/1242 cm^{-1}, 1176 cm^{-1}/1242 cm^{-1} behaved with increasing damage levels (Figure 4.3 and 4.5). For all samples the Amide III region and tyrosine ratios increased with progression of damage with high statistical significance (p_2 <0.001) (Table 4.6 and 4.7). However, the Amide I ratio 1630 cm^{-1}/1680 cm^{-1} did not always increase with progression of damage. A dehydration study to induce collagen denaturation exhibited similar changes to the ratios from mechanical denaturation - that the ratios did increase but the magnitude of increase in the ratios also were not uniform. These findings suggest that the denaturation of the triple helix is a complex process where multiple local conformations affecting the amide bonds eventually leads to helical instability.

4.6 Acknowledgements

I would like to acknowledge the help and support from Simon van Baal.

4.7 References

1. Chen J, Ahn T, Colón-Bernal ID, Kim J, Banaszak Holl MM. The Relationship of Collagen Structural and Compositional Heterogeneity to Tissue Mechanical Properties: A Chemical Perspective. *ACS Nano*. 2017;11(11):10665-10671. doi:10.1021/acsnano.7b06826

2. Zitnay JL, Jung GS, Lin AH, et al. Accumulation of collagen molecular unfolding is the mechanism of cyclic fatigue damage and failure in collagenous tissues. *Sci Adv*. 2020;6(35). doi:10.1126/sciadv.aba2795

3. Benjamin M, Toumi H, Ralphs JR, Bydder G, Best TM, Milz S. Where tendons and ligaments meet bone: Attachment sites ('entheses') in relation to exercise and/or mechanical load. *J Anat*. 2006;208(4):471-490. doi:10.1111/j.1469-7580.2006.00540.x

4. Chen J, Kim J, Shao W, et al. An Anterior Cruciate Ligament Failure Mechanism. *Am J Sports Med*. 2019;47(9):2067-2076. doi:10.1177/0363546519854450

5. Gonzalez LG, Wess TJ. The effects of hydration on the collagen and gelatine phases within parchment artefacts. *Herit Sci*. 2013;1(1):14. doi:10.1186/2050-7445-1-14

6. Latour G, Robinet L, Dazzi A, Portier F, Deniset-Besseau A, Schanne-Klein MC. Correlative nonlinear optical microscopy and infrared nanoscopy reveals collagen degradation in altered parchments. *Sci Rep*. 2016;6(April):1-10. doi:10.1038/srep26344

7. Payne KJ, Veis A. Fourier transform ir spectroscopy of collagen and gelatin solutions: Deconvolution of the amide I band for conformational studies. *Biopolymers*. 1988;27(11):1749-1760. doi:10.1002/bip.360271105

8. George A, Veis A. *FTIRS in H20 Demonstrates That Collagen Monomers Undergo a Conformational Transition Prior to Thermal Self-Assembly in Vitro1"*. Vol 30.; 1991. Accessed March 1, 2021. https://pubs.acs.org/sharingguidelines

9. Iayne KJ, Veis A. *Fourier Transform IR Spectroscopy of Collagen and Gelatin Solutions: Deconvolution of the Amide I Band for Conformational Studies*.

10. Muyonga JH, Cole CGB, Duodu KG. Fourier transform infrared (FTIR) spectroscopic study of acid soluble collagen and gelatin from skins and bones of young and adult Nile perch (Lates niloticus). *Food Chem*. 2004;86(3):325-332. doi:10.1016/j.foodchem.2003.09.038

11. Stani C, Vaccari L, Mitri E, Birarda G. FTIR investigation of the secondary structure of type I collagen: New insight into the amide III band. *Spectrochim Acta - Part A Mol Biomol Spectrosc*. 2020;229:118006. doi:10.1016/j.saa.2019.118006

12. Sellaro TL, Hildebrand D, Lu Q, Vyavahare N, Scott M, Sacks MS. Effects of collagen fiber orientation on the response of biologically derived soft tissue biomaterials to cyclic loading. *J Biomed Mater Res - Part A*. 2007;80(1):194-205. doi:10.1002/jbm.a.30871

13. Lrenz-Fonfria VA, Bamann C, Resler T, Schlesinger R, Bamberg E, Heberle J. Temporal evolution of helix hydration in a light-gated ion channel correlates with ion conductance. *Proc Natl Acad Sci U S A*. 2015;112(43):E5796-E5804. doi:10.1073/pnas.1511462112

14. Bryan MA, Brauner JW, Anderle G, Flach CR, Brodsky B, Mendelsohn R. FTIR studies of collagen model peptides: Complementary experimental and simulation approaches to conformation and unfolding. *J Am Chem Soc*. 2007;129(25):7877-7884. doi:10.1021/ja071154i

15. Jakobsen RJ, Brown LL, Hutson TB, Fink DJ, Veis A. Intermolecular interactions in collagen self-assembly as revealed by Fourier transform infrared spectroscopy. *Science (80-).* 1983;220(4603):1288-1290. doi:10.1126/science.6857249

16. Liu Y, Liu L, Chen M, Zhang Q. Double thermal transitions of type I collagen in acidic solution. *J Biomol Struct Dyn*. 2013;31(8):862-873. doi:10.1080/07391102.2012.715042

17. Mu C, Li D, Lin W, Ding Y, Zhang G. Temperature induced denaturation of collagen in acidic solution. *Biopolymers*. 2007;86(4):282-287. doi:10.1002/bip.20742

18. Cejas MA, Kinney WA, Chen C, et al. Thrombogenic collagen-mimetic peptides: Self-assembly of triple helix-based fibrils driven by hydrophobic interactions. *Proc Natl Acad Sci U S A*. 2008;105(25):8513-8518. doi:10.1073/pnas.0800291105

19. Prockop DJ, Fertala A. Inhibition of the self-assembly of collagen I into fibrils with synthetic peptides: Demonstration that assembly is driven by specific binding sites on the monomers. *J Biol Chem*. 1998;273(25):15598-15604. doi:10.1074/jbc.273.25.15598

20. Tillgren V, Mörgelin M, Önnerfjord P, Kalamajski S, Aspberg A. The tyrosine sulfate domain of fibromodulin binds collagen and Enhances Fibril formation. *J Biol Chem*. 2016;291(45):23744-23755. doi:10.1074/jbc.M116.730325

21. Li C, Ha P, Jiang W, Haveles CS, Zheng Z, Zou M. Fibromodulin – A New Target of Osteoarthritis Management? *Front Pharmacol*. 2019;10:1475. doi:10.3389/fphar.2019.01475

22. Akhtar MA, Ingman TG, Robinson CM, et al. Small leucine rich proteoglycans (SLRP's) expression in skin, tendons and capsules of athletic population after shoulder dislocation and ACL injuries. *Br J Sports Med*. 2011;45(2):e1-e1. doi:10.1136/bjsm.2010.081554.34

23. Hernández B, Pflü F, Adenier A, Kruglik SG, Ghomi M. Vibrational Analysis of Amino Acids and Short Peptides in Hydrated Media. VIII. Amino Acids with Aromatic Side Chains: L-Phenylalanine, L-Tyrosine, and L-Tryptophan. doi:10.1021/jp106786j

24. Na GC. UV Spectroscopic Characterization of Type I Collagen. *Top Catal*. 1988;8(4):315-330. doi:10.1016/S0174-173X(88)80003-7

25. Shen Y, Zhu D, Lu W, Liu B, Li Y, Cao S. The characteristics of intrinsic fluorescence of type I collagen influenced by collagenase I. *Appl Sci*. 2018;8(10). doi:10.3390/app8101947

26. De Simone A, Vitagliano L, Berisio R. Role of hydration in collagen triple helix stabilization. *Biochem Biophys Res Commun*. 2008;372(1):121-125. doi:10.1016/j.bbrc.2008.04.190

27. Kharaz YA, Canty-Laird EG, Tew SR, Comerford EJ. Variations in internal structure, composition and protein distribution between intra- and extra-articular knee ligaments

and tendons. *J Anat*. 2018;232(6):943-955. doi:10.1111/joa.12802

28. Gornall JL, Terentjev EM. Helix-coil transition of gelatin: helical morphology and stability. doi:10.1039/b713075a

29. Bachmann A, Kiefhaber T, Boudko S, Rgen Engel J, Bä HP, Baldwin RL. *Collagen Triple-Helix Formation in All-Trans Chains Proceeds by a Nucleationgrowth Mechanism with a Purely Entropic Barrier*. Vol 27.; 2005. www.pnas.orgcgidoi10.1073pnas.0505141102

30. Martinez MG, Bullock AJ, MacNeil S, Rehman IU. Characterisation of structural changes in collagen with Raman spectroscopy. *Appl Spectrosc Rev*. 2019;54(6):509-542. doi:10.1080/05704928.2018.1506799

31. Woodley DT, Yamauchi M, Wynn KC, Mechanic G, Briggaman RA. Collagen telopeptides (cross-linking sites) play a role in collagen gel lattice contraction. *J Invest Dermatol*. 1991;97(3):580-585. doi:10.1111/1523-1747.ep12481920

32. Handgraaf JW, Zerbetto F. Molecular dynamics study of onset of water gelation around the collagen triple helix. *Proteins Struct Funct Genet*. 2006;64(3):711-718. doi:10.1002/prot.21019

33. Prockop DJ, Fertala A. Inhibition of the self-assembly of collagen I into fibrils with synthetic peptides: Demonstration that assembly is driven by specific binding sites on the monomers. *J Biol Chem*. 1998;273(25):15598-15604. doi:10.1074/jbc.273.25.15598

34. Petersen W, Hansen U. Blood and lymph supply of the anterior cruciate ligament: Cadaver study by immunohistochemical and histochemical methods. *J Orthop Sci*. 1997;2(5):313-318. doi:10.1007/BF02488915

35. Yoshida M, Fujii K. Differences in cellular properties and responses to growth factors between human ACL and MCL cells. *J Orthop Sci*. 1999;4(4):293-298. doi:10.1007/s007760050106

36. Murray MM, Flutie BM, Kalish LA, et al. The Bridge-Enhanced Anterior Cruciate Ligament Repair (BEAR) Procedure: An Early Feasibility Cohort Study. *Orthop J Sport Med*. 2016;4(11):232596711667217. doi:10.1177/2325967116672176

37. Frushour BG, Koenig JL. Raman scattering of collagen, gelatin, and elastin. *Biopolymers*. 1975;14(2):379-391. doi:10.1002/bip.1975.360140211

CHAPTER 5

Conclusion

5.1 Conclusion and future directions

The complex heterogeneity of the human anterior cruciate ligament femoral enthesis has been elucidated via the cadaver loading experiments in this thesis. The cadaver loading system allowed studies that would be unethical to conduct in patients and characterization of direct effects of fatigue to the primary structural protein of ACL without convoluting effects from other extracellular matrix (ECM) components. Utilizing high spatial resolution techniques, we showed molecular to microscale level fatigue damage signatures in Chapter 2 that are not detectable with current clinical diagnostic techniques. In Chapter 3 we used a confocal laser endomicroscope to directly measure the progression of fatigue damage without the need for a contrast agent and we find that the intrinsic autofluorescence increased with progression of fatigue damage. Lastly in Chapter 4, we performed a detailed nanoscale infrared spectroscopic analysis of the changes in collagen's secondary structure as a result of mechanical fatigue that suggested that the denaturation of the triple helix occurs by multiple local conformation changes affecting the Amide bonds, leading to helical instability.

In addition to type 1 collagen, other ECM macromolecules contribute to the tissues specific function and mechanical properties. The ACL possess a uniquely diverse morphological and extracellular protein distribution attributing to the tissues mechanical

function. Through histology and immunostaining, Kharaz et al. showed that healthy canine ACLs possessed less compact collagen fiber architecture, rounded cell morphology and high sulphated GAG and elastin content, reflecting an adaptive response to various mechanical loads as a protection mechanism from tissue damage.[1] The interplay of GAGs and collagen have shown to be critical components in the outcome of tendon biomechanics. Choi et al. demonstrated that the accumulation of sulphated GAG upon focal injury in tendon, led to disorganized collagen networks, which ultimately led to a widespread inferior biomechanics by reduced the elastic modulus and ultimate tensile strength of the tissue.[2] The increase in proteoglycan is hypothesized to interfere with collagen network remodelling and repair.[3] Additional studies purported the link between tissue composition and mechanics, where the proteomic differences between male and female patellar tendon (PT) and ACL influenced the ECM regulation pathways, apoptosis, advanced glycation end-products (AGEs) metabolism and response to mechanical loading to differ between males and females, highlighting the sex-based differential ACL injury risk.[4]

The effect of fatigue on other ECM proteins in the ACL have not been fully explored. Assessing the effect of fatigue in animal models exhibiting inflammation, repair and remodelling processes can provide valuable insight on the biochemical response from the ECM proteins which interact with collagen to determine the tissue's structure and mechanics. Blaker et al. employed a sub-critical knee injury mouse model to investigate the role of sub-critical knee injury on ACL rupture risk and posttraumatic osteoarthritis (PTOA). The study revealed a histological evidence of mild, focal cartilage lesion at the patello-femoral joint (PFJ) region shown by a loss of proteoglycan staining at 8 weeks after injury, in addition to reduced ACL failure load, and rapid onset of allodynia just after 1 week.[5] Further investigation into specific structural and chemical changes is required to determine the drivers of ACL and cartilage pathologies in this mouse model.

The compositional heterogeneity and hierarchical structure of collagen-based tissues play important roles in both tissue structure and function. Therefore, future projects characterizing the changes in local chemical composition of tissue in relation to the mechanics can improve our understanding of the effect of fatigue on ACL. Using AFM-IR, which can simultaneously acquire topography, chemical composition and relative stiffness data at high spatial resolution, areas of local stiffness changes and the locations of stiffness changes in relation to the composition of tissue can be mapped to better understand how local mechanical failure is related to bulk mechanical failure of ACL.

Investigating the changes in proteoglycan levels in response to sub-critical knee injuries are of interest to identify potential early treatment targets for injury and PTOA susceptibility. Employing Optical Photothermal Infrared Spectroscopy (O-PTIR) to map the IR intensities corresponding to proteoglycans from Blaker et al's *in vivo* sub-critically injured mouse may identify and characterize changes earlier than is detectable by conventional techniques (i.e. histology and mechanical testing of tissue). The O-PTIR (mIRage) can determine the locations of altered proteoglycan content in the ACL and map the distribution with sub-micron spatial resolution. Additionally, these findings can provide insight into the fatigue damage response in the context of living systems involving inflammation, repair and remodelling processes.

Finally, the confocal laser endomicroscopy work (Ch.3) can be expanded to study a larger sample set to acquire a more comprehensive view of the change in autofluorescence as a function of fatigue damage accumulation. Additionally, it would be valuable to confirm if the findings in Chapter 3 are reproducible in a larger sample set: i) Does larger autofluorescence signal intensity change indicate plastic deformation of ligament? At what point in the fatigue cycle would this occur? ii) Do the proximal region fibers display a larger change in autofluorescence compared to the midsubstance and distal regions with fatigue loading and can this serve as a pre-injury marker? iii) Can physiological parameters (BMI and posterior lateral

tibial slope) associated with higher risk of ACL injury also affect the autofluorescence signal? The combination of CLE and the intrinsic fluorescence of collagen offer opportunities to expand its application toward diagnosis of ACL fatigue damage prior to damage.

5.2 References

1. Kharaz YA, Canty-Laird EG, Tew SR, Comerford EJ. Variations in internal structure, composition and protein distribution between intra- and extra-articular knee ligaments and tendons. *J Anat*. 2018;232(6):943-955. doi:10.1111/joa.12802
2. Choi RK, Smith MM, Martin JH, et al. Chondroitin sulphate glycosaminoglycans contribute to widespread inferior biomechanics in tendon after focal injury. doi:10.1016/j.jbiomech.2016.06.006
3. Plaas AHK, Wong-Palms S, Koob T, Hernandez D, Marchuk L, Frank CB. Proteoglycan metabolism during repair of the ruptured medial collateral ligament in skeletally mature rabbits. *Arch Biochem Biophys*. 2000;374(1):35-41. doi:10.1006/abbi.1999.1630
4. Little D, Thompson JW, Dubois LG, Ruch DS, Moseley MA, Guilak F. Proteomic Differences between Male and Female Anterior Cruciate Ligament and Patellar Tendon. Published online 2014. doi:10.1371/journal.pone.0096526
5. Blaker CL, Zaki S, BVSc yz, Little CB, Clarke EC. Long-term Effect of a Single Subcritical Knee Injury Increasing the Risk of Anterior Cruciate Ligament Rupture and Osteoarthritis. doi:10.1177/0363546520977505

Appendix

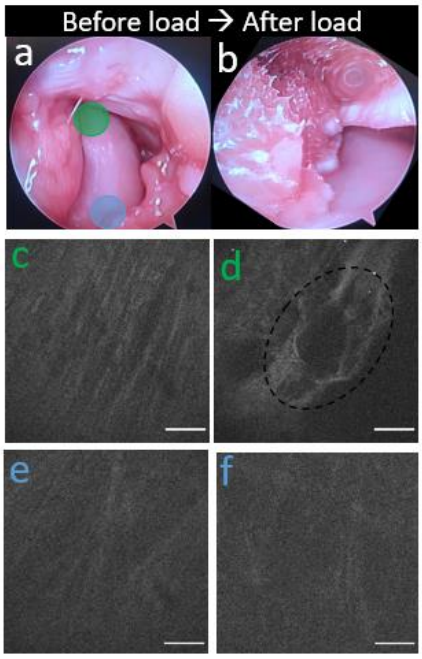

***Figure A.1**. Sample S1. Arthroscopy and CLE image of ACL a) before and b) after 5 pre-loading cycles shows tibial avulsion post loading. CLE probe placement for AF image capture at distal and proximal regions of ACL are marked by green and blue circles respectively. CLE images of distal ACL fibers c) before and d) after tibial avulsion CLE images of proximal ACL fibers e) before and f) after avulsion does not display prominent fiber disruption and possess lower AF increase than the distal region. Scalebar 100µm.*

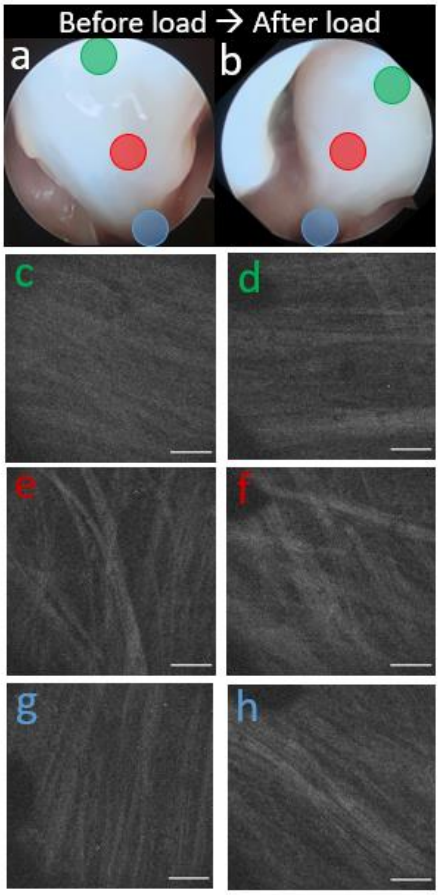

Figure A.2. *Sample S2. Arthroscopy and CLE image of ACL a) before and b) after 5 pre-load + 4 loading cycles shows no apparent damage despite > 3mm anterior tibial translation. CLE probe placement for AF image capture at distal, midsubstance and proximal regions of ACL are marked by green, red and blue circles respectively. CLE images of distal ACL fibers c) before and d) after testing. CLE images of midsubstance ACL fibers e) before and f) after testing display larger gaps between woven fibers. CLE images of proximal ACL fibers g) before and h) after testing. Scalebar 100µm.*

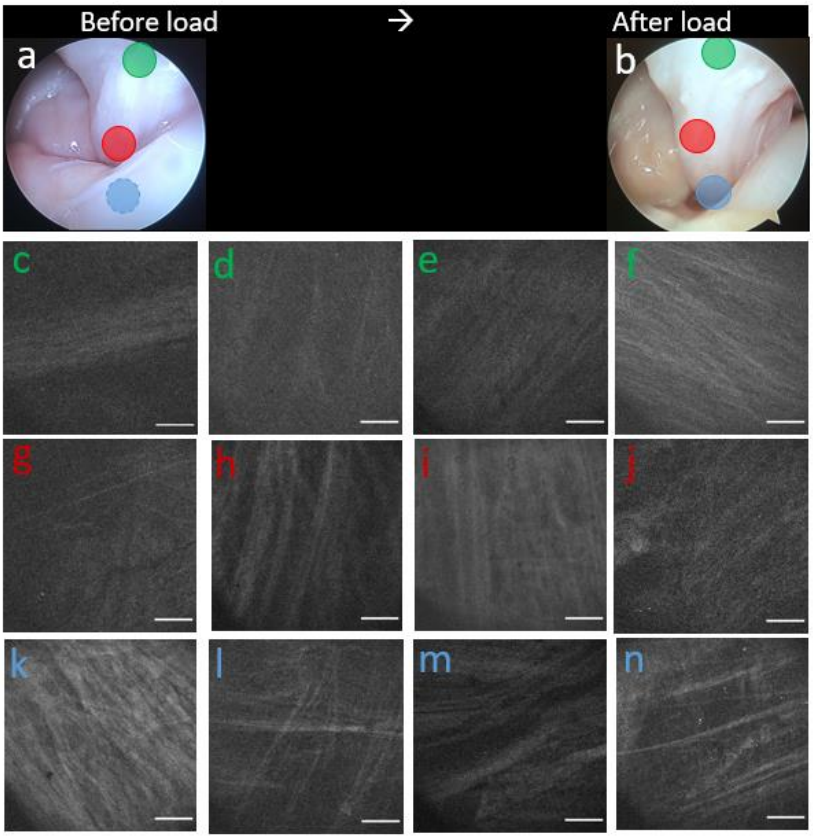

Figure A.3. *Sample S4. Arthroscopy and CLE image of ACL a) before and b) after 105 total loading cycles. CLE probe placement for AF image capture at distal, midsubstance and proximal regions of ACL are marked by green, red and blue circles respectively. CLE images of distal ACL fibers c) before d) after 5 pre-loading cycles e) additional 33 cycles up to f) 45 cycles. CLE images of midsubstance ACL fibers g) before h) after 5 pre-loading cycles i) additional 33 cycles up to j) 45 cycles. CLE images of proximal ACL fibers k) before l) after 5 pre-loading cycles m) additional 33 cycles up to n) 45 cycles. Scalebar 100µm.*